PERTURBATIONS OF CELLULAR MEMBRANES WITH SYNTHETIC POLYMERS AND ULTRAFAST LASERS

by

Christopher Vaughn-Daigneau Kelly

A dissertation submitted in partial fulfillment
of the requirements for the degree of
Doctor of Philosophy
(Applied Physics)
in The University of Michigan
2009

Doctoral Committee:

Professor Mark M. Banaszak Holl, Co-Chair
Professor Bradford G. Orr, Co-Chair
Professor James R. Baker, Jr.
Associate Professor Zhan Chen

DEDICATION

To my parents for the running start they gave me

ACKNOWLEDGEMENTS

Gratitude - The feeling of being deeply appreciative of kindness; friendly feeling toward a benefactor; kindness awakened by a favor received; thankfulness.

I am eternally grateful for the vast contributions to this thesis and my education from my colleagues, friends, and family over the last 5 years. I have learned more about science and life than I had imagined possible. Each of you has taught me in ways that I cannot describe sufficiently here. I offer my most sincere thank you.

I have learned the most from my many advisers. As in all aspects of life, each professor had his own twist on the questions worth answering and the most effective approaches. The gift of having numerous professors advise me has been profound; this aspect of my education has been the most rewarding. Thank you Brad Orr, Mark Banaszak Holl, James Baker, Yumi Ijiri, Ioan Andricioaei, David Reis, Zhan Chen, Daniel Styer, Ron Larson, Rona Qi, Sharon Glotzer, John Scofield, Thommey Thomas, Theodore Norris, Anna Bielinska, Elliott Hill, Jolanta Kukowska-Latallo, Istvan Majoros, Dick Jackson, James Penner–Hahn, Andrzej Myc, and Ayyalusamy Ramamoorthy, Ankur Desai, Christine Orme, Charlie Brooks, Steven Wright, Len Sander, and Brian Talbot.

In particular, my thesis chairs, Mark Banaszak Holl and Brad Orr, have given me a better understanding of their perspectives and have been better teachers than I had ever expected. Their kindness, patience, and wisdom benefited my education and growth immensely. They have made me well-prepared and excited to dedicate my life to the advancement of knowledge.

My fellow students have enhanced my education, contributed to these scientific advancements, and made these years enjoyable. Our discussions, whether scientific or otherwise, have ensured the foundations of my education were strong, broadened my interests, and extended my intellectual abilities. Thank you, dear friends, Pascale Leroueil, Almut Mecke, Damian Kahn, Seungpyo Hong, Jessica Hessler, Bonnie Ludwig, Randon Walker, Eric Tkaczyk, Jeffery Wereszczynski, Song Ge, Kevin Landmark, Bernell Williams, Jiumei Chen, Ajdin Kavara, Douglas Mullen, Ahleah Rohr, Daniel McNerny, Maria Mills, Blake Erickson, Jesse Ward, Pieter Smith, Rahul Rattan, Prashant Padmanabhan, Meghan Liroff, Devon Triplett, Rebecca Lahti, Joseph Wallace, Lisa Prevette, Maggie Kober, Päivö Kinnunen, Andrew Boughton, Kandapa Cousineau, Stephanie Berry, Kristin Duthie, Paul Makidon, Meredith Brenner, Alexander Hrin, Joshua Stein, Chan Huntington, Justin Kline, Andrew Zheng, Stephen Siciliano, Timothy Sullivan, Hwankyu Lee, Brandon McNaughton, Jasper Kok, Divine Kumah, Kat Smirl, Beau Truex, Abigail Mechtenberg, Nicole Onyeneho, Phill Grajek, Bo Sun, Leon Webster, Katie Bach, Jeffery Herbstman, Pamula Wong, Edgar Lee, Hao Ding, Liz McDowell, Sam Pazicni, Bill Pfleger, Peter Kananen, David LaTarte, Allison LaTarte, and Shanna Shaked.

On both technical and intellectual challenges, the kind support of many University staff members have made this research possible. In particular, thank you Charles Sutton, Michael Parise, Thomas Dunham, Alina Kotlyar, Nancy Hobbs, David Braun, Sasha Meshinchi, Cynthia McNabb, Claire Verweij, Gloria Lippens, Katherine Wood, and for your contributions to this work.

Outside of science, my life is made complete thanks primarily to my beautiful wife, Kathryn. Katie has provided me with the love and support necessary for me to feel like I can achieve anything. Katie's love for me is ever-present and awe-inspiring. I am forever grateful for my Love and her acceptance of me. I owe endless gratitude to Katie for her patience, encouragement, and kindness.

TABLE OF CONTENTS

LIST OF TABLES

LIST OF FIGURES

ABBREVIATIONS

AFM	Atomic Force Microscopy
CG	Coarse-grained
D	Diffusion Constant
DLS	Dynamic Light Scattering
DMEPC	1,2-Dilauroyl-s*n*-Glycero-3-Ethylphosphocholine
DMPC	1,2-Dimyristoyl-s*n*-Glycero-3-Phosphocholine
DMPG	1,2-Dimyristoyl-s*n*-Glycero-3-[Phospho-*rac*-(1-glycerol)]
DMPS	1,2-Dimyristoyl-s*n*-Glycero-3-[Phospho-L-Serine]
δt	Time between sequentially acquired images, (Frame rate)$^{-1}$
Δt	Diffusion time
EPR	Electron paramagnetic resonance
FA	Folic acid
FITC	Fluorescein isothiocyanate
G	Generation of dendrimer
GFP	Green fluorescent protein
GPMV	Giant plasma membrane vesicles
ITC	Isothermal titration calorimetry
k_B	Boltzmann's constant
Laser	Light amplification by stimulated emission of radiation

LDH	Lactate dehydrogenase
m	Any positive integer
MD	Molecular dynamics
MSD	Mean squared displacement
MTX	Methotrexate
n	Dimensionality of the tracking
NMR	Nuclear magnetic resonance
PALM	Photo-activated localization microscopy
PAMAM	Poly(amidoamine)
PI	Propidium iodide
PC	Phosphatidylcholine
PS	Phosphitidyleserine
R110-AAA_2	Rhodamine 110 bis-(L-aspartic acid amide)
STORM	Stochastic optical reconstruction microscopy
t	Time
T	Temperature
TEM	Transmission Electron Microscopy
x	Particle location
Z-VAD-fmk	Z-Val-Ala-Asp(OCH_3)-Fluoromethylketone

ABSTRACT

This dissertation examines the response of the plasma membrane to perturbations by synthetic nanoparticles and ultra-fast laser pulses. Both model membranes and living cells were examined to characterize membrane disruption and the biological response to perturbation. These studies provide a deeper understanding of cell biology and guide the design of effective nanoparticle- or laser-based therapies.

In regards to membrane disruption by pulsed-laser irradiation, irradiation induced giant plasma membrane vesicles (GPMVs) on the surface of the living cell. GPMV formation involved the incorporation of material from the extracellular media into both the cytoplasm and the GPMV as the cell responded to the intense pressure and temperature gradients induced by irradiation and cavitation. Further, cells exposed phosphotidylserine to the exterior surface of the plasma membrane and initiated caspase activity. Single particle tracking of 20 nm fluorescent beads within the GPMVs demonstrated a complex, gelatinous structure within the GPMV.

In regards to nanoparticle-based perturbations, techniques such as isothermal titration calorimetry and molecular dynamics were used to investigate the relationship between nanoparticle properties and membrane disruption. Molecular dynamics simulations examined the binding of third-generation poly(amidoamine) dendrimers to phosphatidylcholine bilayers as a function on nanoparticle termination and membrane

phase. A potential of mean force was calculated. It demonstrated that the charged dendrimers bound to gel-phase zwitterionic phospholipids with approximately 50% more free energy release than uncharged dendrimers. Further, the difference in dendrimer binding to gel and fluid lipids was largely due to the hydrophobic interactions between the lipid tails and the non-polar dendrimer moieties. Isothermal titration calorimetry examined the heat release upon interaction between dendrimers and phospholipids. Identification of key changes in the heat release versus dendrimer-lipid molar ratio suggested the formation of generation-dependent dendrimer-lipid complexes. This work suggested that dendrimers of seventh-generation or greater formed vesicle-encased dendrimer complexes while smaller dendrimers primarily formed complexes of the dendrimer flattened on a planar bilayer.

CHAPTER 1

INTRODUCTION

1.1. MOTIVATION

The plasma membrane is a vital component of animal cells with a complex structure-function relationship. Among its many functions, the plasma membrane is the first line of defense for an individual cell against foreign materials and physical disruptions. Thus, the cellular fate upon exposure to synthetic nanoparticles or membrane-rupturing events critically depends on the response of the plasma membrane.

From an evolutionary perspective, animals are constantly exposed to small particles that would harm them if the plasma membrane did not to prohibit their entry. The evolved protection mechanisms work well for micron-sized objects, such as dust and bacteria, as well nanoscale objects from natural sources, being either biological in origin (e.g. proteins or viruses) or in relatively low concentrations (e.g. from volcanoes and forest fires). However, modern industrial processes are creating nanoscale materials at high concentrations with surface moieties not present in nature (Fig. 1.1). These synthetic nanoparticles are used in applications that frequently result in direct human contact, such as lotions, cosmetics, and therapeutics. Because synthetic nanoparticles have been shown to cause harm to animal cells, and, in particular, the plasma membrane,[1-3] it is imperative that the biological effects of synthetic nanoparticles be

understood and minimized. The numerous applications of nanoparticles in commercial products may provide enhanced functionality of the product in some aspects, but the effects of the nanoparticles on the user and environment are motivation for better understanding and design for nanoparticles in biological systems.

Figure 1.1. Many commercial products are now incorporating nanotechnologies, including cosmetics. As a result, exposure to nanoparticles is increasing and appropriate design of nanoparticles to minimize side effects is warranted.[4]

Not only is it necessary to understand what nanoparticle will induce membrane permeability or pore formation, it is also necessary to understand how the cell responds to such a disruption. The physiological response to defects on the plasma membrane are an area of ongoing research.[5, 6] By better understanding the cellular response to assorted nanoscale perturbations, synthetic nanoscale materials may be better designed for the desired biological response.

From a therapeutic perspective, physicians often want particular medicinal particles to enter the cell despite the natural membrane processes preventing it. Biomedical researchers are developing nanodevices capable of overcoming the natural

barriers and even exploiting the cellular process to transport a therapeutic into a cell.[7, 8] Like a Trojan horse, a targeted cancer therapeutic tricks the plasma membrane of a cancer cell to internalize the chemotherapeutic that results in the death of the diseased cell. Modern drug delivery applications, such as this, rely on the controlled interaction of the plasma membrane with synthetic nanodevices (Fig. 1.2).

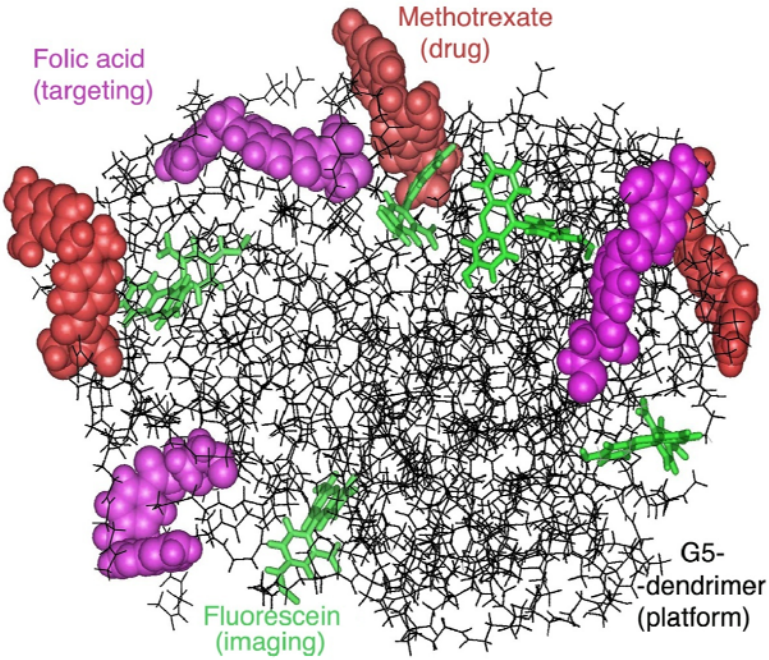

Figure 1.2. This biomedical nanodevice acts like a Trojan horse to a cancer cell. The nanodevice is bound and internalized by the plasma membrane of cancer cell via the folic acid. Once internalized, it reports the location of the cancer cell via the fluorescein and kills the cancer cell via the methotrexate.[9]

This thesis examines the response of membranes to nanoscale perturbations. In particular, ultrafast laser pulses and synthetic nanoparticles are used to stress both living and model membranes for a better understanding of how the membrane responds to such perturbations and how to design nanodevices that are more effective.

1.2. STRUCTURE AND FUNCTION OF THE PLASMA MEMBRANE

By surrounding animal cells (Fig. 1.3), the plasma membrane is a vital component of life and performs three key functions to the survival of a cell: (1) physically encloses the organelles, salts, proteins, etc., (2) supports a variety proteins and sugars that depend on the hydrophobic/hydrophilic balance of the membrane, and (3) regulates which surrounding materials should enter the cell – keeping out materials that would be harmful while taking in materials that are beneficial. The plasma membrane is a complex, dynamic, and necessary component of life and has been the focus of extensive research.[10]

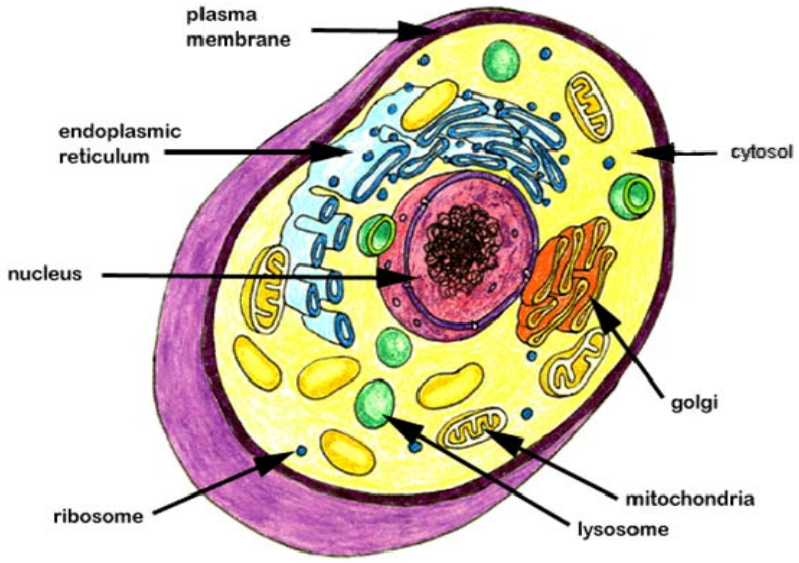

Figure 1.3. The plasma membrane surrounds the cell. All the organelles and the cytosol are confined by the plasma membrane.[11]

As shown in Fig. 1.4, the plasma membrane is composed of a variety of lipids, proteins, and carbohydrates in a complex, dynamic mixture. Although significant cell type variations exist, the membrane is composed of approximately 50% by weight proteins and 50% by weight lipids, with assorted carbohydrates and other proteins in close proximity to the membrane. The lipids maintain the membrane structure by sequestering their hydrophobic components within the middle of the membrane and

exposing hydrophilic components to the aqueous cytoplasm and extracellular environments.

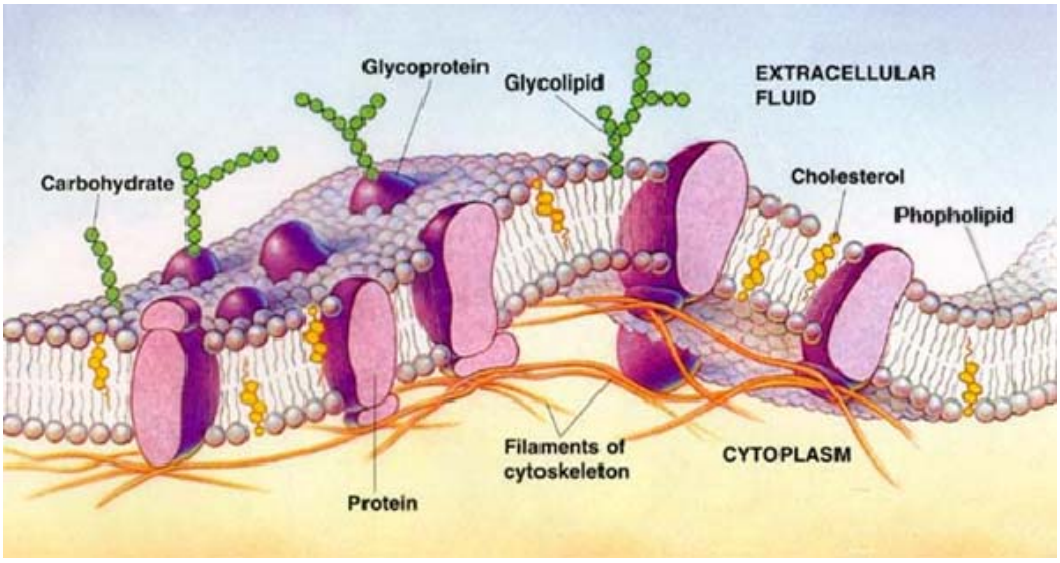

Figure 1.4. The plasma membrane is composed of a variety molecules as it surrounds living cells, the most numerous of which are phospholipids.[12]

Lipids are fat-soluble molecules and, thus, contain hydrophobic moieties that segregate from water. The plasma membrane includes a variety of lipids, such as cholesterol, glycerolipids, and sphingolipids that are essential to membrane function. The subgroup of glycerolipids that contain a phosphate moiety, called glycerophospholipids or phospholipids, are the dominate type of lipids in the cellular membranes. Phospholipids are amphipathic, containing both a hydrophobic, tail region and a hydrophilic, head group region (Fig. 1.5). The phospholipid tails vary in length and degree of saturation and the phospholipid head groups vary in charge and size. These molecular differences result in differing physical properties of the phospholipid bilayers, such as thickness, curvature, and phase transition temperature.

The differing environments and complex cell processes require substantial differences between the inner and outer membrane leaflets. For example, cell-to-cell

communication or signaling utilizes cellular control of the molecules presented on the extracellular side versus the intracellular side of the plasma membrane. In particular, the lipids with a phosphatidylserine (PS) head group (Fig. 1.5) are confined to the cytoplasmic side of the membrane where they facilitate cytoskeleton-membrane interactions. However, PS is exposed to the extracellular side when the cell is dying and ought to be decomposed for the wellbeing of the host organism. By utilizing this phenomenon, PS expression is a commonly used in the laboratory to detect if a cell is dying.

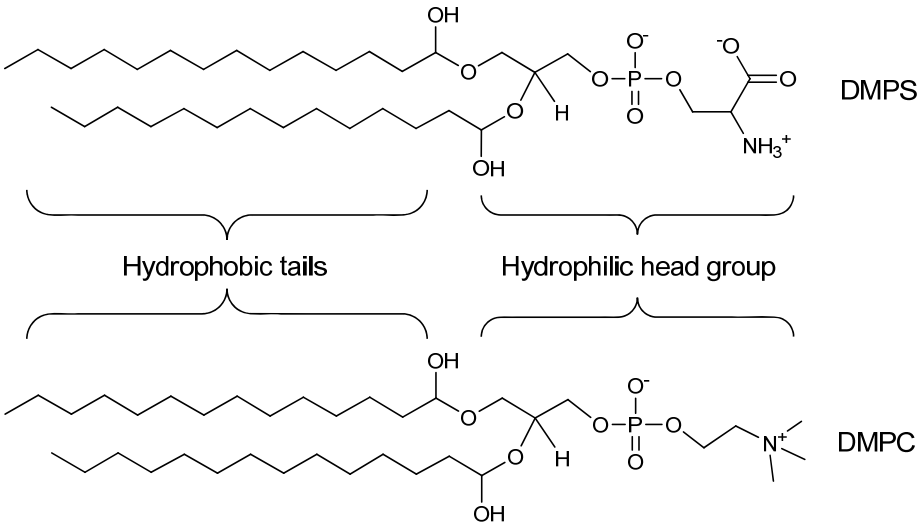

Figure 1.5. Atomic structure of the phospholipid 1,2-Dimyristoyl-*sn*-Glycero-3-[Phospho-L-Serine] (DMPS) and 1,2-Dimyristoyl-*sn*-Glycero-3-Phosphocholine (DMPC). DMPS is utilized for cell signaling and DMPC is the most common phospholipid on most plasma membranes.

The most common lipid molecules in the plasma membrane have a head group of phosphatidylcholine (PC, Fig. 1.5). PC head groups are zwitterionic, with negatively charged phosphate and positively charged choline moieties. Because PC head groups are the most numerous on the plasma membranes, model membranes are commonly constructed solely of PC lipids without in any proteins, carbohydrates, and lipids types.

As described below, these models provide simple experimental system for examination of the fundamental membrane properties and responses.

1.3. MODELS OF THE PLASMA MEMBRANE

Model membranes are commonly created from pure phospholipid samples. Most commonly, model membranes are composed of only phosphatidylcholine head groups and tails of either 14 or 16 carbons each. (Figs. 1.5 and 1.6). Model membranes composed of only phospholipids allow for relatively simple determination of the how the lipids contribute to the membrane behavior and which membrane functions require additional proteins, sugars, etc. For example, the membrane tension, curvature, phase transition, and passive diffusion are largely controlled by the phospholipids.

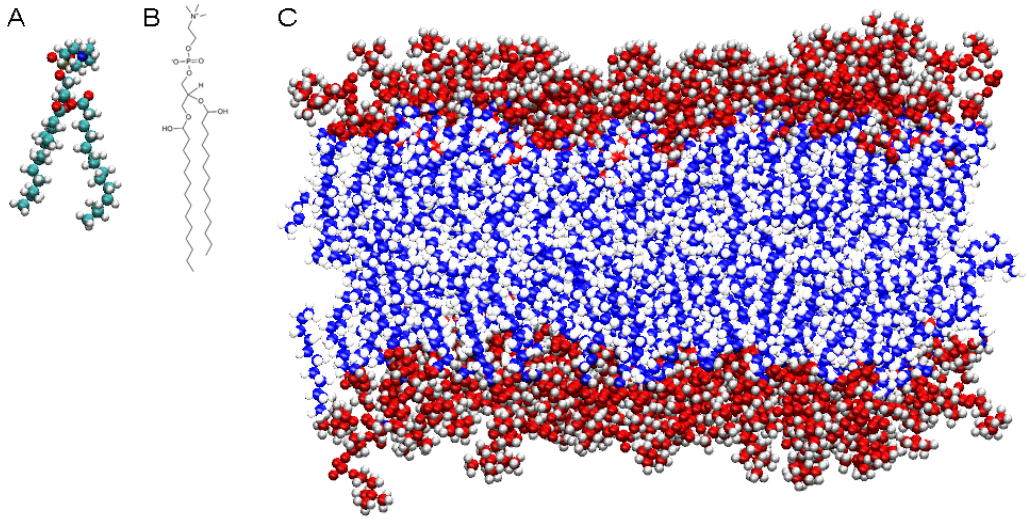

Figure 1.6. (A, B) A DMPC molecule and (C) bilayer composed of 146 DMPC molecules. A simulation of this bilayer would require periodic boundary conditions such that the inner, hydrophobic components are separated from the water surrounding the bilayer. See Fig. 1.5 for a larger view of (B).

The membrane curvature and surface tension are fundamental membrane properties that greatly affect membrane function. The details of these interactions have

been the focus of considerable research over the past 40+ years. Properties of membrane that only contain one lipid type have been accurately modeled since the 1970's and relatively simple models exist for the basic membrane functions.[13] The properties of complex phospholipid bilayers and the affects of varying lipid types on the bilayer are only recently being understood. Many of the more complex membrane functions, such as lipid rafts, depend on the complex interaction of many lipid types and are a current area of research.[14-16]

The dominant features of individual lipid molecules that determine the resulting membrane include (1) the area of the hydrophilic head group, (2) the volume of the hydrophobic tails, (3) the contour length of the hydrophobic tails, and (4) their phase transition temperatures. In particular, the ratio of the lipid dimensions (e.g. cone vs. cylinder shape) determines the radius of curvature preferred for the membrane (Fig. 1.7). These variables have been combined by Israelachili et al. in a seminal paper modeling the distribution of vesicle sizes to be expected in a solution of lipid molecules.[13]

In brief, Israelachili et al. assumed neighboring lipid molecules had an attractive potential, parameterized by a surface tension, and a repulsive potential. The repulsive potential depends on many factors, but was used, with the surface tension, solely to determine the area per head group on the membrane surface. With an approximation for the free energy as a function of the head group area, Israelachili et al. consider the packing constraints of the lipids tails. Primarily, they consider the volume and contour lengths the tails. This model explains how lipids with one tail are capable of forming micelles and lipids with two tails are not. By further considering the balance of chemical potential from all vesicle sizes in solution, Israelachili et al. calculated a distribution of

vesicle sizes in solution. This method has been used recently to analyze the distribution of vesicles in solution in the presence of cationic nanoparticles.[17] A description of this phenomenon is also given in numerous recent reviews.[15, 16]

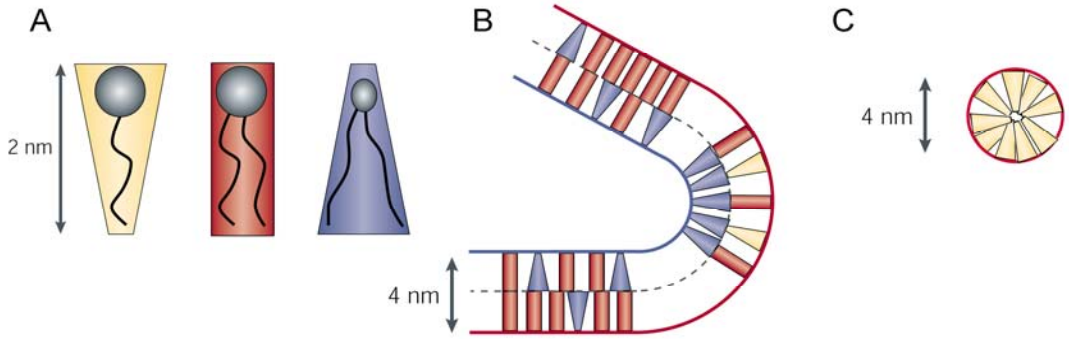

Figure 1.7. (A) Individual lipid molecules vary in the size of the head group in comparison to the volume of the tails. (B) Lipid molecules may form into a bilayer and induce curvature without increasing the membrane bending energy. (C) A different mixture of lipid molecules may form into a micelle. This image is adapted from Sprong et al.[15]

Model membranes are commonly utilized to examine how living membranes are capable of adjusting their surface area through the induction of phase transitions without the addition or removal of individual lipid molecules. Membrane phase transitions, and particularly lipid rafts, have important ramifications for cell signaling, endocytosis, and homeostasis.[18] For example, in transition from fluid-ordered to a fluid-disordered phase, the area per lipid molecule can change for 20-30% while the volume changes by only 2-4%.[19] Similarly, the phase transition temperature of a membrane can be altered widely through variation in the lipid molecules. In general, the addition of lipid molecules with longer tails, lipid tails greater degrees of unsaturation, or small hydrophobic molecules such as cholesterol decrease the phase transition temperature. These properties of lipids allows for spacial variation in fundamental membrane properties through differing local lipid compositions.

1.4. DISRUPTION OF THE PLASMA MEMBRANE

A variety of processes may occur in which the plasma membrane is unable to perform the functions required for cellular homeostasis. For example, under sufficient osmotic pressure, the plasma membrane is incapable of maintaining appropriate salt and water concentrations. In hypotonic solutions, the large cytoplasmic osmotic pressure results in a swelling of the cell and eventual rupture of the plasma membrane. Hypertonic solutions result in cell shrinking and removal of water from the cell. This is particularly evident in red blood cells, which lack the traditional cytoskeleton (Fig. 1.8).

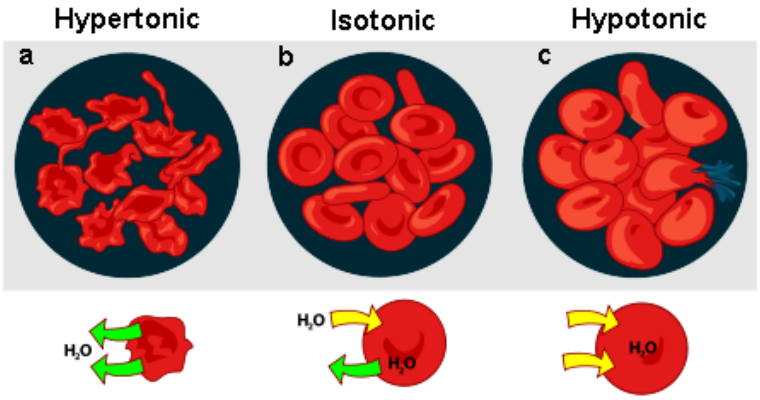

Figure 1.8. Variation in the osmotic pressure of the surrounding media affects cells. The plasma membrane can only maintain homeostasis within a limited range of environmental conditions. In a hypertonic solution (a), the relative osmotic pressures cause water to leave the cell. In a hypotonic solution (c), the plasma membrane can rupture due to the net influx of water.[20]

Many other stimuli exist which prevent the plasma membrane from maintaining homeostasis. For example, the presence of detergents can dissolve the membrane, viruses can penetrate the membrane, and extreme temperatures can disrupt the proteins functioning within the membrane. These stimuli differ in their mechanisms, yet failure of the plasma membrane in any of these ways frequently results in cellular death.

Commonly, disruptions of the plasma membrane include reducing the membrane's ability to prevent the leakage of cytosolic proteins into the extracellular environment. Nanoparticles are particular potent at inducing membrane leakage. Synthetic nanoparticles can be made from a variety of materials, such as hard polymers (e.g. polystyrene), metals (e.g. gold or iron), or deformable polymers (e.g. polyethlyeneglycol or polyethyleneimine) with the nanoparticle surface area and charged identified as the primary predictors of membrane disruption.[1]

A common way to test membrane permeability is by measuring the leakage of lactate dehydrogenase (LDH) from cells upon exposure to assorted antagonists (e.g. nanoparticles). LDH is naturally confined within the cytoplasm, but upon exposure to large, cationic dendrimers, LDH is released from the cell into the surrounding media. Previous studies have identified poly(amidoamine) (PAMAM) dendrimers as a nanoparticle capable of inducing LDH release (Fig. 1.9).[2, 21] In particular, the larger and greater charged dendrimers are more effective at disrupting the plasma membrane.

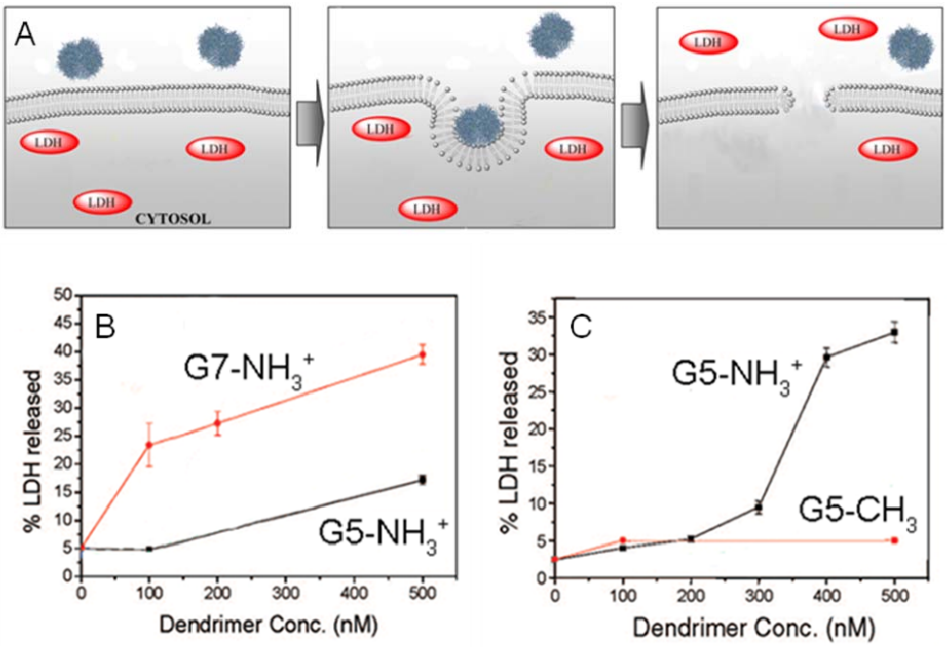

Figure 1.9. Measuring LDH release from cells is a convenient way of measuring the degradation that has occurred to the plasma membrane. (A) Poly(amidoamine) dendrimers interact with the plasma membrane and result in membrane degradation and LDH release. (B) Large seventh-generation dendrimers (G7) cause more leakage than small fifth-generation dendrimers (G5). (C) Cationic, amine terminated dendrimers cause more leakage than uncharged, acetylated dendrimers.

Attempts have been made to examine the disruption of the plasma membrane in greater detail with atomic force microscopy (AFM). AFM provides nanometer resolution to the topography of supported lipid bilayers. Upon exposure to seventh-generation, charged PAMAM dendrimers, pores are observed forming within the membrane (Fig. 1.10). In contrast, uncharged fifth-generation PAMAM dendrimers with acetyl termini do not form membrane pores as readily (Fig. 1.11). The smaller, uncharged dendrimers are more likely to accumulate on the membrane surface rather than remove lipids from the bilayer, as done by the larger, charged dendrimers. These atomic scale images are consistent with the LDH leakage assays.

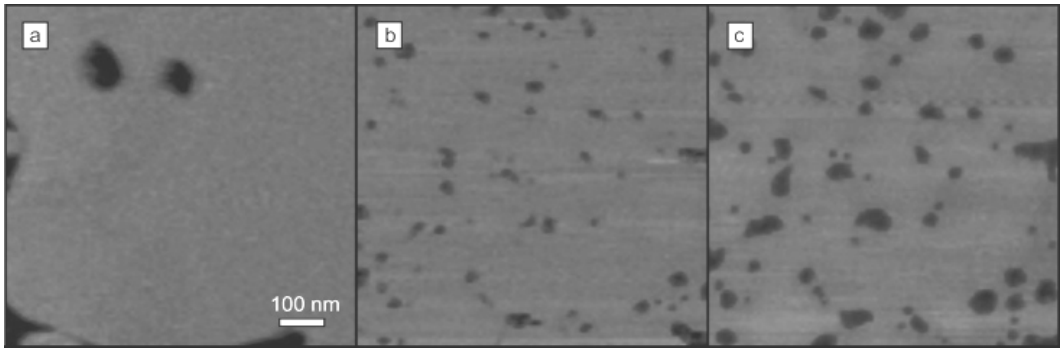

Figure 1.10. Atomic force micrograph of a supported lipid bilayer (grey) exposed to seventh-generation PAMAM dendrimers and the formation of numerous membrane pores (black). (A) Before, (B) 20 min after and (C) 60 min after dendrimer addition. Dendrimers are 1.4-42 μM and the bilayer is 4.5 nm above the mica below.[22]

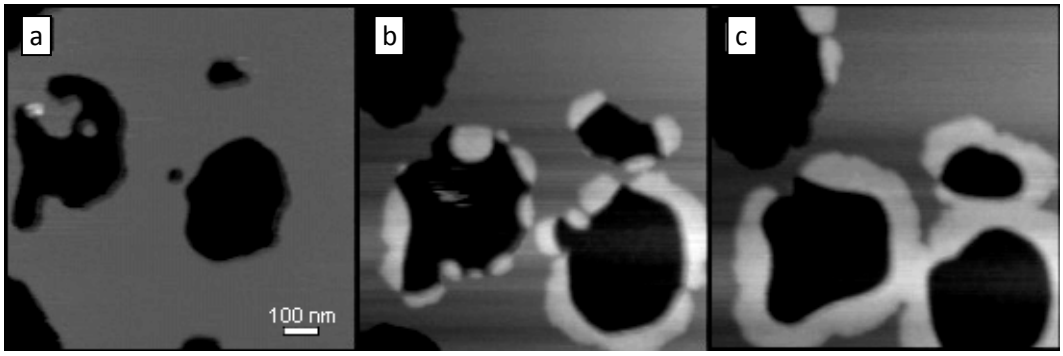

Figure 1.11. Atomic force micrograph of supported lipid bilayer (medium grey) exposed to fifth-generation PAMAM dendrimers with acetylated termini. Membrane pores (black) grow slightly, but primarily, dendrimers are observed accumulating on the surface of the membrane (light grey). A) Before, (B) 15 min after and (C) 32 min after dendrimer addition. Dendrimers are 1.4-42 μM and the bilayer is 4.5 nm above the mica below. Dendrimer aggregates are 1.5 nm above bilayer.[22]

1.5. CONCLUSIONS

This thesis aims to further nanoscale understandings of the plasma membrane and its response to nanoparticle and laser perturbations. Chapter 2 focuses on the effects of ultrafast laser pulses and the local cavitation within the plasma membrane. The membrane responds to such stress through the formation of giant plasma membrane vesicles and the biophysics of these vesicles are examined. Chapter 3 utilizes isothermal titration calorimetry (ITC), transmission electron microscopy (TEM), and dynamics light scattering (DLS) to examine the energetics and stoichiometry of mixing of PAMAM dendrimers and phospholipid vesicles. These studies identify the dendrimer-lipid complexes that may result in membrane pore formation. Chapters 4 and 5 examine the atomic interactions of PAMAM dendrimers and DMPC bilayers through molecular dynamics simulations. The computational modeling of dendrimers and lipids allows for examination of which atomic moieties of each molecule are dominating the interaction.

Chapter 6 provides an analysis of these main conclusions, including their strengths and shortcomings, and a discussion of further possible experiments.

1.6. REFERENCES

1. Leroueil, P. R.; Berry, S. A.; Duthie, K.; Han, G.; Rotello, V. M.; McNerny, D. Q.; Baker, J. R.; Orr, B. G.; Holl, M. M. B., Wide varieties of cationic nanoparticles induce defects in supported lipid bilayers. *Nano Letters* **2008,** 8, (2), 420-424.
2. Leroueil, P. R.; Hong, S. Y.; Mecke, A.; Baker, J. R.; Orr, B. G.; Holl, M. M. B., Nanoparticle interaction with biological membranes: Does nanotechnology present a janus face? *Accounts of Chemical Research* **2007,** 40, (5), 335-342.
3. Oberdorster, G.; Oberdorster, E.; Oberdorster, J., Nanotoxicology: An emerging discipline evolving from studies of ultrafine particles. *Environmental Health Perspectives* **2005,** 113, (7), 823-839.
4. Maynard, A. D.; Aitken, R. J.; Butz, T.; Colvin, V.; Donaldson, K.; Oberdorster, G.; Philbert, M. A.; Ryan, J.; Seaton, A.; Stone, V.; Tinkle, S. S.; Tran, L.; Walker, N. J.; Warheit, D. B., Safe handling of nanotechnology. *Nature* **2006,** 444, (7117), 267-269.
5. Idone, V.; Tam, C.; Andrews, N. W., Two-way traffic on the road to plasma membrane repair. *Trends in Cell Biology* **2008,** 18, (11), 552-559.
6. McNeil, P. L., Repairing a torn cell surface: make way, lysosomes to the rescue. *Journal of Cell Science* **2002,** 115, (5), 873-879.
7. Langer, R., Drug delivery and targeting. *Nature* **1998,** 392, (6679), 5-10.
8. Quintana, A.; Raczka, E.; Piehler, L.; Lee, I.; Myc, A.; Majoros, I.; Patri, A. K.; Thomas, T.; Mule, J.; Baker, J. R., Design and function of a dendrimer-based therapeutic nanodevice targeted to tumor cells through the folate receptor. *Pharmaceutical research* **2002,** 19, (9), 1310-1316.
9. Kukowska-Latello, J. As part of NCI Platform Partnership, researchers will focus on using nanoparticles to diagnose, treat cancer, http://www.med.umich.edu/opm/newspage/2005/nanocancer.htm. (Dec. 19, 2008),
10. Sadava, D. E.; Heller, H. C.; Orians, G. H.; Purves, W. K.; Hillis, D. M., *Life, the Science of Biology*. 8th edition ed.; W.H. Freeman & Company: 2008.
11. Carpi, A. The Natural Science Pages, http://web.jjay.cuny.edu/~acarpi/NSC/. (Dec. 19, 2009),
12. Krempels, D. http://fig.cox.miami.edu/Faculty/Dana/membrane.jpg. (Dec 19, 2009),
13. Israelachvili, J. N.; Mitchell, D. J.; Ninham, B. W., Theory of Self-Assembly of Lipid Bilayers and Vesicles. *Biochimica Et Biophysica Acta* **1977,** 470, (2), 185-201.
14. Baumgart, T.; Hess, S. T.; Webb, W. W., Imaging coexisting fluid domains in biomembrane models coupling curvature and line tension. *Nature* **2003,** 425, (6960), 821-824.
15. Sprong, H.; Sluijs, P. v. d.; Meer, G. v., How proteins move lipids and how lipids move proteins. *Nature Reviews Molecular Cell Biology* **2001,** 2, (7), 504-513.
16. McMahon, H. T.; Gallop, J. L., Membrane curvature and mechanisms of dynamic cell membrane remodelling. *Nature* **2005,** 438, (7068), 590-596.
17. Mecke, A.; Majoros, I. J.; Patri, A. K.; Baker, J. R.; Holl, M. M. B.; Orr, B. G., Lipid bilayer disruption by polycationic polymers: The roles of size and chemical functional group. *Langmuir* **2005,** 21, (23), 10348-10354.
18. Pike, L. J., Lipid rafts: bringing order to chaos. *Journal of Lipid Research* **2003,** 44, (4), 655-667.

19. Jahnig, F., What is the surface tension of a lipid bilayer membrane? *Biophysical Journal* **1996,** 71, (3), 1348-1349.
20. Villarreal, M. R. http://en.wikipedia.org/wiki/File:Osmotic_pressure_on_blood_cells_diagram.svg. (Dec. 19, 2009),
21. Hong, S. P.; Leroueil, P. R.; Janus, E. K.; Peters, J. L.; Kober, M. M.; Islam, M. T.; Orr, B. G.; Baker, J. R.; Holl, M. M. B., Interaction of polycationic polymers with supported lipid bilayers and cells: Nanoscale hole formation and enhanced membrane permeability. *Bioconjugate Chemistry* **2006,** 17, (3), 728-734.
22. Mecke, A.; Lee, D. K.; Ramamoorthy, A.; Orr, B. G.; Holl, M. M. B., Synthetic and natural polycationic polymer nanoparticles interact selectively with fluid-phase domains of DMPC lipid bilayers. *Langmuir* **2005,** 21, (19), 8588-8590.

CHAPTER 2

PULSED-LASER CREATION AND CHARACTERIZATION OF GIANT PLASMA MEMBRANE VESICLES FROM CELLS

2.1. INTRODUCTION

Giant plasma membrane vesicles (GPMVs) are fluid-filled membrane bound protrusions from the extracellular surface of living cells and are naturally created during cell death, division, locomotion, and as a response to physical or chemical stress. GPMV formation is generally controlled by the cell through regulation of the cortical-actin and plasma membrane structure, via assorted proteins, such as caspases, myosin-I and II, cytochalasin B, HSP27, myosin light chain kinase, p38, p21, and Rho GTPases.[1-8] However, GPMV formation may also occur as an out-of-control cellular response resulting from a disrupted cytoskeleton or pressure imbalances, such as burn, blunt trauma, hypoxia, inflammation, poison, and infection.[1, 3, 9-15] These stress-induced GPMVs are the focus of this study.

Both stress and self-induced GPMVs result from an intracellular pressure not contained by the cortical actin, resulting in a separation of the plasma membrane from the cytoskeleton. [2, 9, 10, 12, 16-18] Dynamic, reversible GPMVs, such as those during mitosis, locomotion, or apoptosis, are triggered by an asymmetric build up of pressure and structural integrity by the cortical actin.[4, 18, 19] These reversible GPMVs were then either utilized by the cell as a vesicle or retracted back into the main cellular body by regained

cytoskeleton structure.[7, 20] By way of contrast, dynamic, irreversible GPMVs do not demonstrate such well controlled function as they are often associated with necrosis and occasionally called blisters.[3, 15, 21] Irreversible GPMVs tend to be initiated by a chemical or physical stress which results in the permeation of the cortical actin and separation of the plasma membrane.[9, 10] Such vesicles are not retracted back into the cell and generally indicate pending cellular death via necrosis. Irreversible GPMV formation can result in an uncontrolled release of cellular contents, capable of harming neighboring cells. Currently, very little is known of the underlying biophysics of irreversible GPMV behavior and gaining more understanding may lead to better treatment of acute tissue damage.

Pulsed-laser irradiation was used to trigger irreversible GPMV formation in a particular cell while leaving neighboring cells unaffected. The ability to trigger GPMV formation in this fashion is useful because it allows controlled studies on a single cell in close proximity to unaffected control cells. Thus, this method of inducing GPMV formation is quite distinct from bulk chemical or physical treatments that induce vesicle formation and affect all cells within the sample. In this aspect, laser irradiation is more akin to microinjection or micro-disruption of a single cell. Additional advantages of laser irradiation over bulk methods include fine control of the laser pulse duration, rate, intensity, and focal spot location, and thus the ability to vary widely the incident stress upon the cell.

The high peak electromagnetic field intensities of pulsed-laser systems affect cells through the induction of multi-photon processes such as sub-diffraction limited ablation and enhanced light absorption at the focal spot, as reviewed by Vogel et al.[22] Pulsed-

lasers have been utilized for sub-cellular dissection of mitochondria,[23, 24] chromosomes,[25, 26] and cytoskeleton filaments,[27, 28] with nanometer precision as well as to study transfection,[29] membrane permeability,[30] vesicle formation,[30, 31] and embryo development.[32] Irradiation is a particularly interesting tool for examination of vesicle formation because it is capable of initiating GPMV formation on a single cell either in vivo or in vitro with careful control of the imposed stress while avoiding both adverse effects on neighboring cells and unknown chemical side-effects.[29, 32] Multiphoton absorption, particularly 790 nm with low single-photon water absorption, has high potential for bioengineering and medical applications due to the ability to tightly focus in all three dimensions within a patient while avoiding collateral damage in the out of focus regions.[22]

Single particle tracking (SPT) has become a frequently used in micro-rheology measurements to determine the material properties in biological systems.[33] SPT has been used to characterize the properties of myosin,[34] microtubules,[35] actin,[36] and the crowding within the cytoplasm.[37, 38] Here we utilize SPT to determine the viscosity and structure of cellular vesicles.

This paper describes the morphology, dynamics, contents, viscoelastic, and biophysical properties of cellular vesicles resulting from pulsed-laser irradiation. We report on the capability of laser pulses to initiate extracellular GPMV formation and further examine the physical properties, F-actin distribution, caspase activity, membrane permeability, and phosphatidylserine (PS) externalization of the resulting blebs. Vesicles incorporate material from the cytosol (e.g. cytosolic GFP, F-actin, 65 nm polystyrene beads, and caspase proteases) as well as from the surrounding media (e.g. propidium

iodide, Annexin-V, and anionic dextran). Simultaneously, irradiation induces membrane permeability that results in the release of cytoplasmic contents (e.g. cytosolic GFP) into the surrounding media. Vesicles are characterized in terms of viscosity and internal structure through SPT of fluorescent bead diffusion.

2.2. RESULTS

2.2.1. Irradiation and Vesicle Formation

Femtosecond laser pulses have been utilized to stimulate extracellular GPMV formation on individual living cells. The irradiation was absorbed in a volume less than the diffraction limit within an individual cell. The initial effect of laser irradiation on cells was the creation of short-lived gas filled micro-bubbles (0.5 - 5 μm diameter) within the cytoplasm of the cells (15 – 30 μm diameter). The micro-bubble formation occurred within 0.1 sec upon laser pulse exposure and lasted less than 3 sec, similar to the micro-bubbles observed previously.[39, 40] Micro-bubble size was controlled with incident intensity and pulse duration. The smallest micro-bubbles (< 1 μm diameter) usually did not initiate vesicle formation within 10 min. Large micro-bubbles (> 2 μm diameter) resulted in larger, more numerous GPMV formations and were sufficient for that vesicle's formation within the following 60 sec. Micro-bubble and vesicle formation were observed on all nine different adherent cell lines examined (Fig. 2.1). The only cell line that did not grow GPMVs as a result of irradiation was mouse red blood cells, which has a substantially different spectrin-based cytoskeletal structure.[41]

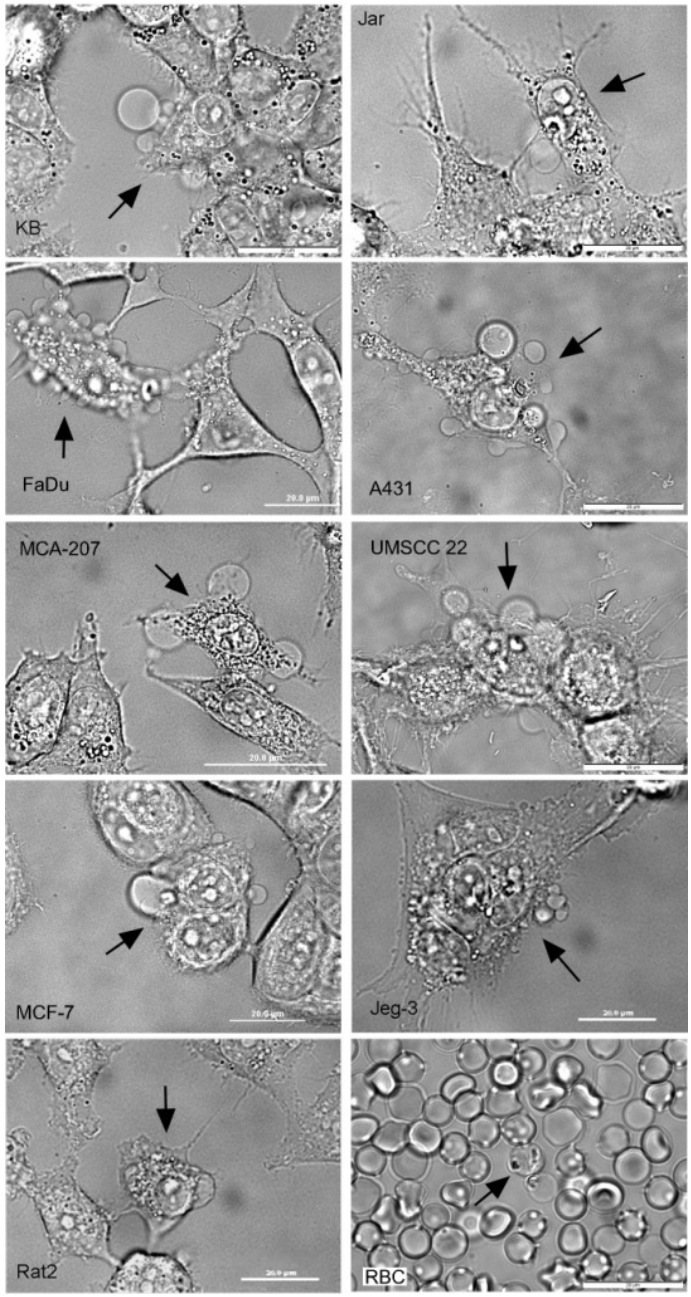

Figure 2.1. Pulsed laser irradiation (790 nm, 62 fs, 4 nJ/pulse, 90 MHz) induces micro-bubble formation and GPMV formation in both continuous and primary lines human cell lines and a rat fibroblast line. Each brightfield micrograph shows one irradiated cell (as indicated by the arrow) and vesicles formation on the plasma membrane. Micrographs also include control cells within view for direct observation of the effects of irradiation. The varieties of GPMVs seen here are also seen between cells within a single cell line. The cellular response to irradiation is not specific to any particular cell type, but rather seems to be a general response to pulsed laser irradiation by cells. An interesting exception is found for mouse red blood cells (RBCs) which, although clearly damaged, do not vesicle as a result of irradiation, as shown in the bottom right image.

Large variation in GPMV size and number per irradiated cell were found between irradiation events. GPMV growth rates were highest when the vesicle first started growing and decreased continuously over time. GPMVs did not reach their maximum size within 500 min (Fig. 2.2 and 2.3). This observation of decreasing growth rate with time is interesting in light of a previous study in which a constant growth rate of GPMV was observed during cell re-adhesion post trypsinization.[16] Variations in the stimulus of GPMV formation have a profound effect upon the vesicle growth rate, growth duration, and possible retraction.

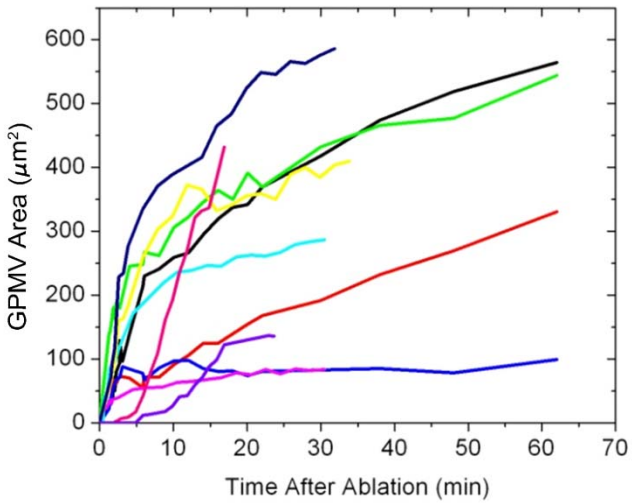

Figure 2.2. GPMV growth begins soon after irradiation, usually within the first 30 sec. Generally, vesicles' growth rates decrease soon after they are initiated; however, they do not reach a final size within 60 min (for an example over 500 min see Fig. 2.3). The vesicle volume can be estimated by assuming a spherical vesicle, in which case these results do not change significantly. This data has a 10% uncertainty due to errors in visual vesicle edge determination and variation in microscope focal plane height relative to the largest vesicle cross sectional area.

The morphology of the laser-induced GPMVs was compared to the vesicles created through other common cell stressors: broad-spectrum UV light, hypotonic solutions, and physical rupture. GPMVs from either the UV light or the physical rupture appeared morphologically identical to the laser-induced vesicles; the vesicles were

optically homogeneous, surrounded by a PS containing membrane, and generally spherical. Cells exposed to a hypotonic solution display stress and some vesicle formation, however the vesicle morphologies were considerably different. Cells in a hypotonic environment expand uniformly and tended not to make localized, spherical vesicles on the plasma membrane, although this varied with the age and general health of the cells.

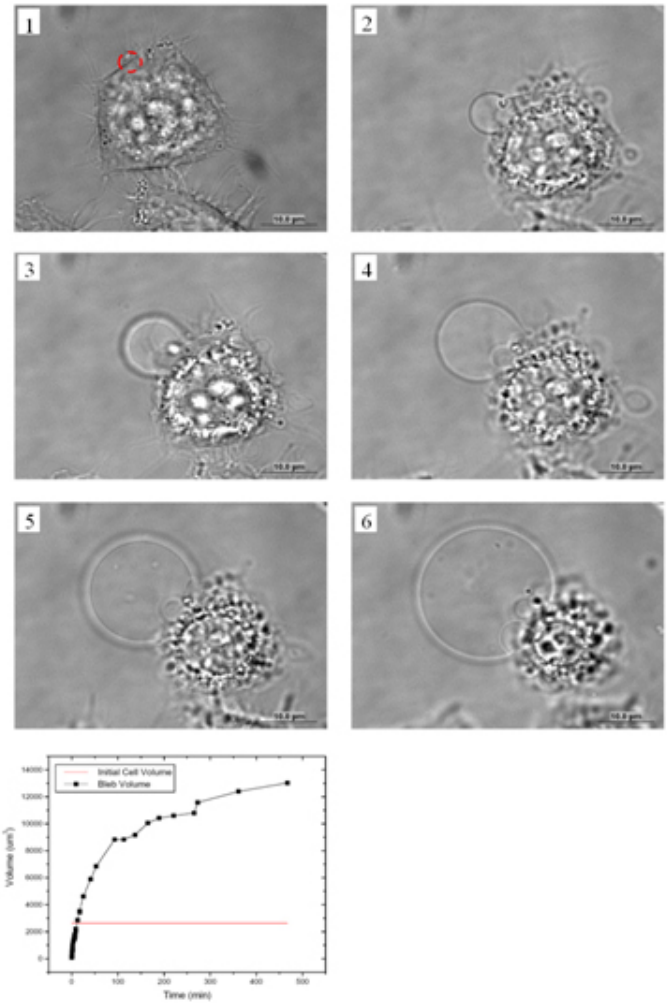

Figure 2.3. GPMV growth and volume change over 500 min. The volume increases very quickly initially then slows; however, the GPMV continues to grow over 500 min to a volume approximately 4.5 times the initial volume of the cell.

Micro-bubble and subsequent vesicle formation as a result of laser irradiation was never observed while the Ti:sapphire laser oscillator was in a continuous-wave mode of operation with similar average power. The mode-locked operation, with high peak intensity and multi-photon processes, was required for the increased laser absorption at the focal spot and micro-bubble formation. A poorly aligned laser setup or a previously stressed cell culture would reduce the likelihood of micro-bubble formation, whereas increased incident power could counter this.

2.2.2. Membrane permeability and GPMV contents

The contents of the fluid-filled vesicle were analyzed through the flow of fluorescent molecules (e.g. propidium iodide (PI), 10 kDa dextran and 40 kDa dextran) from the cytoplasm and the surrounding media into the GPMV. The adherent cells were initially surrounded by fluorescent, anionic dextran of either 10 or 40 kDa. Dextan is not thought to strongly interact with any particular cellular component and is slowly taken into the cytoplasm of healthy cells by pinocytosis.[42] Upon irradiation and vesicle formation, both the 10 and 40 kDa dextran were separately observed, relative fluorescence intensities, at greater concentrations within the cytoplasm and resulting vesicles of irradiated cells than the unaffected surrounding cells (Fig. 2.4a-d). The concentration of dextran within the irradiated cells was always less than that of the surrounding solution regardless of incubation time, until the surrounding solution was replaced removing extracellular dextran. This result indicates irradiation induces membrane permeability sufficient for flow of 40 kDa molecules through the plasma membrane and that dextran did not concentrate within the cell.

PI was used to probe the cell plasma membrane integrity and the time scale of the degradation. PI is a brightly fluorescing small molecule commonly used to assess membrane integrity since it cannot enter cells with intact plasma membranes and binds strongly to nucleic acids. PI entered irradiated cells immediately (< 30 sec) after irradiation and continued to enter cells for up to 2 hr after irradiation (Fig. 2.4e-f). 2 hr after irradiation, the cells visually appeared to be highly stressed and it is presumed that these irradiated cells never recovered their membrane integrity, as is common for necrotic cells. Since the fluorescence signal from PI varies greatly depending on its proximity to nucleic acids, relative concentrations of PI within the cytoplasm and the extracellular media could not be easily determined. Both the dextran and PI results indicate cellular irradiation induces plasma membrane permeability and flow of material from the surrounding media into the cytoplasm and resulting vesicles.

Flow of material from the cytoplasm to the GPMV was observed directly through irradiation of cytosolic-GFP expressing cells (Fig. 2.4g-h). The GFP was initially distributed throughout the cytosol and was observed to enter the vesicle immediately upon vesicle growth post irradiation. This result shows that material flows from the cytoplasm to the vesicle upon irradiation.

Over time, the intensity of the GFP fluorescence signal from the irradiated cell was observed to decrease relative to the neighboring control cells (Fig. 2.4h). GFP was never directly observed in the extracellular media, as if released from the irradiated cell. However, the dilution of the GFP within the extracellular media would likely make the fluorescent signal undetectable. This result is consistent with material flowing from the

cytoplasm to the extracellular media upon irradiation, but this could not be directly detected.

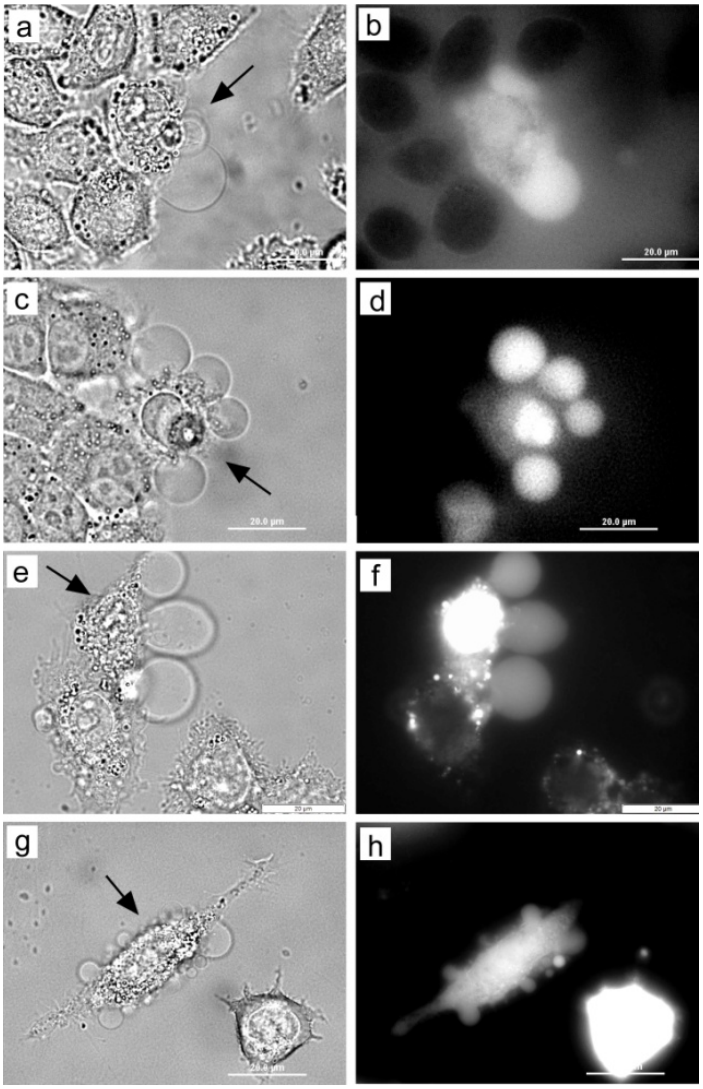

Figure 2.4. Material flows from the surrounding media into the irradiated cell, from surrounding media into GPMVs, and from the cytoplasm into the GPMVs of irradiated cells. The irradiated cell in each brightfield micrograph is indicated with the arrow and is surrounded by control cells. The KB cells at 37 °C were surrounded by (a, b) 40 kDa anionic dextran-Alexa Fluor 488, (c, d) 10 kDa anionic dextran-Alexa Fluor 488, or (e, f) propidium iodide. MCF-207-cytosolic GFP cells (g, h) were irradiated and emitted fluorescence from both the cytoplasm as well as the GPMVs. The difference in fluorescence intensity from the irradiated and control GFP expressing cells indicates that cytoplasmic material is also released from the irradiated cell.

The F-actin filaments in the cytoplasm and the vesicle were examined with phalloidin-Alexa Fluor 488. Phalloidin binds strongly to F-actin and was observed throughout the cytoplasm and the vesicle after irradiation (Fig. 2.5).[43] Although blurry in appearance, the phalloidin fluorescence within the vesicle was not due to an out-of-focus signal, as determined through the narrow focal range of the 100x oil-immersion objective utilized. The center of the vesicle clearly demonstrated a stronger fluorescence signal than either the bottom or top of the vesicle, indicating the source of the fluorescence was originating from the center of the vesicle. Long filaments of F-actin were observed throughout the cytoplasm, however no filaments were observed in the GPMVs. The vesicle and the cytoplasm fluoresce brighter than the surrounding media, whether or not the excess surrounding phalloidin was removed. This indicates that the phalloidin, presumably bound to F-actin, accumulates inside the cell, unlike dextran.

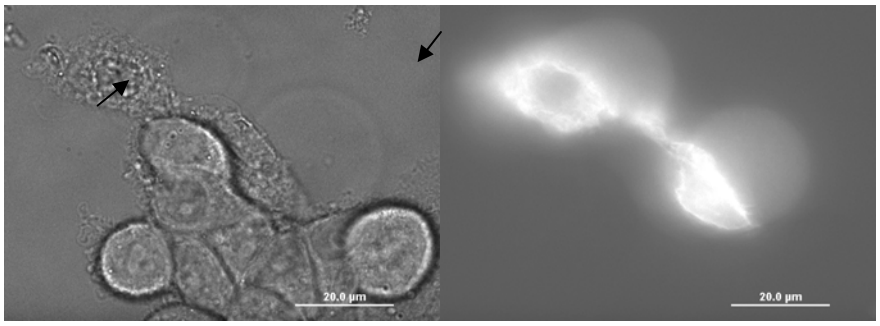

Figure 2.5. The GPMVs of irradiated cells incorporate F-actin without any filamentary structure at 37 °C. Brightfield and fluorescence micrographs of two irradiated KB cells and approximately nine control cells in a PBS solution containing phalloidin-Alexa Fluor 488 are shown. GPMV formation and strong fluorescence was observed for both irradiated cells, as indicated with arrows. The phalloidin was presumed to be bound to F-actin and collecting in the cell and GPMVs due to their increased brightness than the surrounding media before the excess phalloidin is rinsed off. The concentration of phalloidin in the cytoplasm is clearly higher than that in the GPMV, however carefully chosen brightness and contrast settings show both filamentary structure through the cytoplasm and uniform fluorescence throughout the GPMV significantly higher than the background.

2.2.3. Caspase effects

The biochemical effects of laser irradiation were tested through fluorescent studies of Rhodamine 110-bis(L-aspartic acid amide)$_2$ (R110-AAA$_2$). This fluorochrome is only fluorescent after cleavage by caspase. The presence of caspases indicates the biochemical cascade associated with apoptosis and eventual cell death. Irradiated cells displayed strong R110-AAA$_2$ fluorescence and thus caspase activity (Fig 2.6).

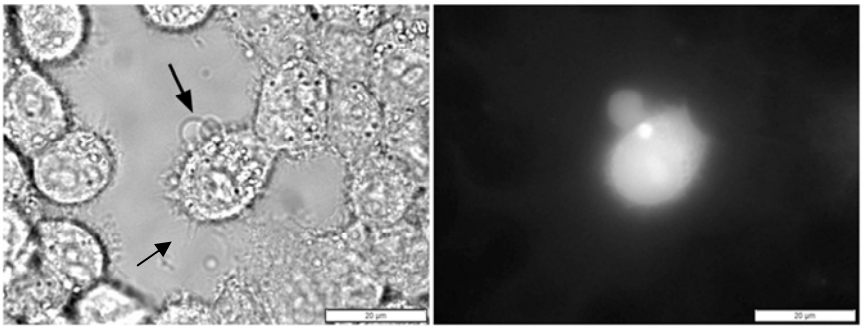

Figure 2.6. Irradiation activates the caspase cascade at 37 °C. Brightfield and Fluorescence micrographs of a single irradiated KB cell in the middle of each panel (as indicated by the arrow) surrounded by many control cells are shown. The surrounding PBS solution contains rhodamine 110 bis-(L-aspartic acid amide) (R110-AAA$_2$). R110-AAA$_2$ is capable of entering all cells but only fluoresces upon cleavage by caspase proteases. Fluorescence is observed in both the cytoplasm and the vesicles of the irradiated cell.

GPMV activity was also analyzed in MCF-7 cells, which lack caspase-3, to test the contribution of caspase-3 in the cellular response to irradiation. Irradiated MCF-7 cells displayed similar vesicle formation and R110-AAA$_2$ fluorescence as all other epithelial and fibroblast cells examined. This result indicates that caspase-3 was not essential for vesicle formation or R110-AAA$_2$ cleavage and that other caspases were activated by irradiation.

Further, Z-Val-Ala-Asp(OCH$_3$)-Fluoromethylketone (Z-VAD-fmk) was used to inhibit the presence of all caspases in MCF-7 cells. Cells that were irradiated after incubation with Z-VAD-fmk displayed the identical GPMV response as all other analyzed epithelial and fibroblast cells. As expected, cells incubated with Z-VAD-fmk

displayed no R110-AAA_2 fluorescence after irradiation. These results show that pulsed-laser initiation of GPMVs does not require the caspase biochemical pathway.

2.2.4 Phosphatidylserine (PS) externalization

The molecular makeup of the exterior vesicle wall and the location of PS lipid molecules were characterized with Annexin V-Alexa Fluor 488. Annexin V is commonly used to track PS and cannot enter cells with intact plasma membranes. Annexin V was used to examine the availability of PS on the plasma membrane and on the vesicle wall. Within 20 min of irradiation, Annexin V bound to the plasma membrane of the main cell body and vesicle wall of the irradiated cell (Fig. 2.7), confirming that the vesicle wall contains phospholipids and suggesting irradiation induces PS externalization to the extracellular plasma membrane leaflet.

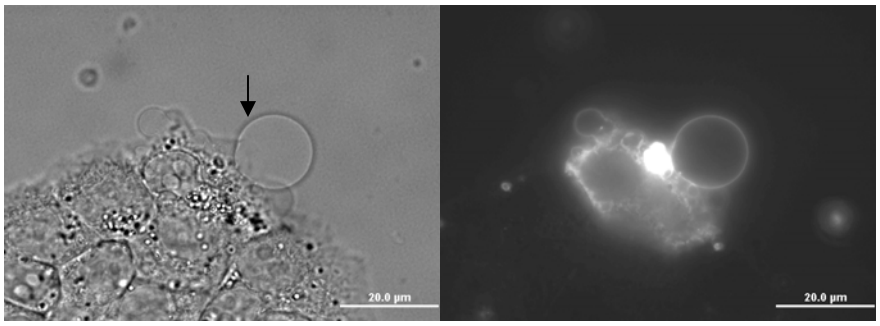

Figure 2.7. Irradiated cells externalize PS lipids on all the exposed cell membranes. Brightfield and fluorescent micrographs of KB cells surrounded by Annexin V-Alexa Fluor 488 and binding buffer at 37 °C are shown. The single irradiated cell (as indicated by the arrow) is atop a group of about eight other cells also within view. The control cells show no PS externalization. The irradiation focal spot shows brightest on the fluorescence image.

Within this study, Annexin V is not necessarily assumed to be on only the outside of the cell because of the plasma membrane permeability induced by irradiation. However, attempts to internalize Annexin V using both electroporation and microinjection showed no intracellular signal from the plasma membrane or organelles

(data not shown). This negative result is consistent with current understanding that intracellular PS bound was to the cytoskeleton and not available for Annexin V binding.[44] Therefore, it is concluded that the Annexin V was bound to PS on the extracellular side of the plasma and vesicle membranes of irradiated cells.

2.2.5 Inner-vesicle single particle tracking (SPT)

The viscosity of within vesicles was quantified through SPT of internalized 65 nm fluorescent beads. During incubation before irradiation, 5 to 15 beads were internalized into each cell. Many beads were also bound to the dish bottom when not covered by the adherent cells and remained bound after rinsing with fresh media. These beads are present throughout the data collection and present a significant, yet acceptable, out of focus background fluorescence. Roughly 5% of the irradiation induced GPMV incorporated at least one bead, of which the vast majority had only one bead per vesicle. The diffusion of these beads was imaged at 15 frames per second and analyzed to extract the diffusion constants and to identify obstacles to free diffusion. These results were interpreted as an effective viscosity of the vesicle contents since the size of the bead likely influences its freedom to diffuse in this crowded environment. The traces of particle movement revealed the structures within the vesicle that limited free diffusion. Characteristic irradiated cells with beads in the GPMV are shown in Fig 2.8, in which the trajectories of the tracked beads are shown.

Identical SPT experiments were attempted on UV light induced vesicles. However, a greatly decreased likelihood of the bead migrating from the cytoplasm to the vesicle made such experiments problematic; < 0.05% of UV induced vesicles incorporated a fluorescent bead.

A bead trajectory displaying free diffusion throughout the vesicle is shown in Fig 2.8a-c. Examination of the bead's free *vs.* restricted diffusion throughout the vesicle revealed important information about the internal vesicle structure. 30% of all beads interacted with the outer vesicle wall and 40% interacted strongly with some other optically transparent structure within the vesicle. A bead trajectory that seems to be interacting strongly with inner-vesicle obstacles is shown in Fig 2.8d-f. The mean square displacement (MSD) *vs*. diffusion time (Δt) for two beads is shown in Fig 2.9 where the freely diffusing bead yields MSD proportional to Δt and the highly restricted bead displays MSD proportional to $(\Delta t)^{\alpha}$ with $\alpha = 0.65$.

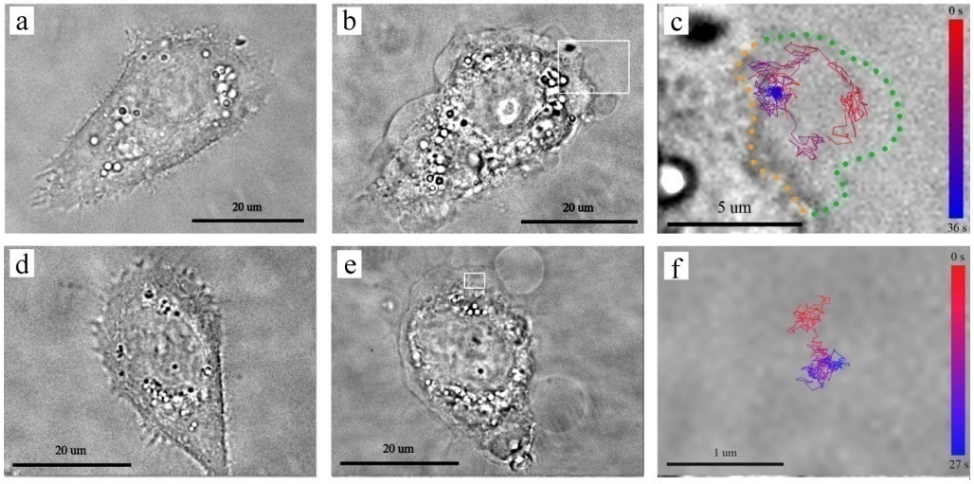

Figure 2.8. The GPMVs of irradiated cells incorporate fluorescent beads, which can be tracked. (a, d) Before irradiation, (b, e) post irradiation, and (c, f) bead trajectory micrographs of KB cells at 37 °C are shown. (c, f) are magnifications of the rectangles in (b, e), respectively. GPMV formation occurs on all non-adherent sections of the plasma membrane, encompasses a large portion of the exterior cell surface, and occasionally shows highly spherical shape. In (c), the bead moves throughout the vesicle without significant interacting with an interior vesicle structure; the effective viscosity within this vesicle is 220 cP. In (f), the bead is constrained to a small portion of the vesicle by some optically transparent inner-vesicle structure. The collision rate between the bead and the inner-vesicle structure in (f) is too high to be determined by our experimental setup. The color bar in (c, f) represents the time coarse of the bead's trajectory. In (c), green dots guide the eye around the vesicle and orange dots indicate the vesicle-plasma membrane interface.

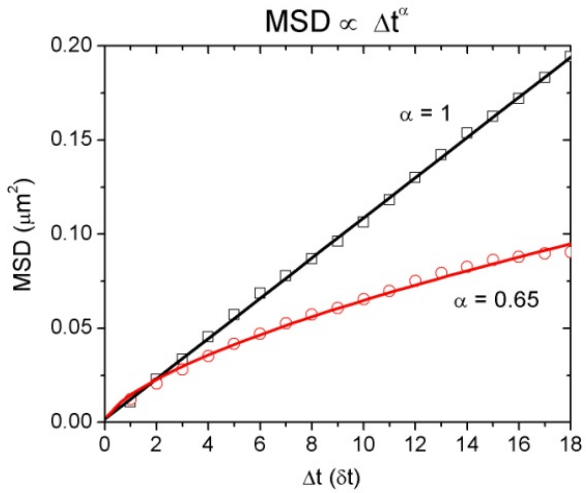

Figure 2.9. Mean square displacement versus diffusion time. Shown is a freely diffusing particle with $\alpha = 1$ and a particle with obstructed diffusion with $\alpha = 0.65$ where $MSD \propto \Delta t^{\alpha}$. The x-axis scale is in units of inverse frame rate, $\delta t = 67$ msec.

The measured effective viscosities did not display a correlation between magnitude of viscosity and size of confinement within the vesicle, therefore these measured viscosity values represent the effective viscosity for a 65 nm bead within the vesicle. 70% of the beads in vesicles were unable to diffuse freely throughout the vesicle. Many of these trajectories are unable to yield useful effective viscosity values due to their rapid obstacle collision rate as compared to the image capture rate. The beads that were not confined in any dimension to a range of less than 300 nm were able to yield the diffusion constant and the effective viscosity of their surrounding media (Fig 2.10). The observed vesicle viscosities vary from 32 to 434 cP, with a mean of 160 ± 110 cP and 8% random error on all measurements.

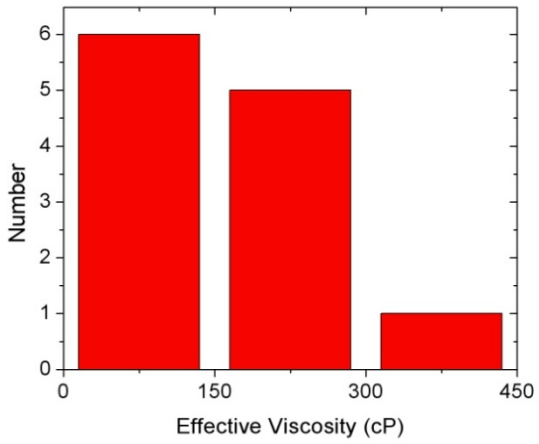

Figure 2.10. Histogram of measured effective viscosities in GPMVs. Observed viscosities range from 32 to 434 cP and lower viscosities are more common. The average effective viscosity of the 65 nm beads is 160 ± 110 cP a wide distribution of observed viscosities. The uncertainty of each viscosity measurement is 8%, as demonstrated in Fig 2.13.

Material properties of the vesicle and cytoplasm were given by analysis of diffusing beads in the vesicle. The beads used in this study were 65 nm in diameter. Both larger (200, 390, 780 nm) and smaller (40 nm) beads were tested, but did not allow for convenient SPT within the vesicles. All beads were internalized into the cytoplasm during the pre-irradiation incubation. However, the larger beads had a greatly decreased likelihood of entering the GPMV, likely due to restrictions in the cytoplasm preventing their flow into the GPMV. The smaller beads did not emit enough fluorescence for adequate SPT in this experimental setup. To accommodate these experimental requirements, the 65 nm beads were used exclusively for the data presented throughout this paper.

2.3. DISCUSSION

Pulsed-laser irradiation was utilized for the generation of vesicles on individual cells *in vitro*. These vesicles were analyzed with fluorescence and brightfield microscopy

for quantification of GPMV properties, the process by which GPMVs were formed, and the overall cellular response to irradiation. The vesicles resulting from laser irradiation seem to be similar to the subset of vesicles occasionally called blisters, since they were created from injury, rather than chemical stimulus, and, like other blisters, these show no inner F-actin structure or vesicle retraction.[1, 5, 30, 45] The variety of cell lines examined indicates this is a common cellular response and can be considered a general cellular response to femtosecond laser irradiation in living animal cells. The vesicles are described in terms the source of the material that fills them, the biochemical and physical mechanisms of their formation, and their structural properties.

GPMVs have been previously used to understand further the composition of the plasma membrane through the detection of local variations in membrane phase, molecular distribution, and membrane curvature. [14, 46, 47] Fig 2.7 demonstrates that the GPMVs created via pulsed laser irradiation demonstrate homogeneous PS distribution at 37 °C. This result is consistent with the homogeneous membrane compositions found in chemically induced GPMVs, where phase and molecular segregation were observed only at colder temperatures (≈ 23 °C).[47]

2.3.1 GPMV morphology and structure

The laser-induced vesicles were preferentially formed on the plasma membrane near the irradiation spot, however vesicles were observed on all surfaces of some irradiated cells. Two types of vesicles were formed: Type 1, those that contacted the cell over a relatively small portion of the plasma membrane and possessed a highly spherical shape, and Type 2, those that made contact with a significant portion (> 15%) of the total

plasma membrane surface with an irregular, non-spherical shape. Some vesicles seem to be intermediate between Types 1 and 2.

This organization of the vesicles into different types is similar to the categorization done by Keller *et al*.[17] However, Keller *et al*. distinguished vesicles types by cortical and cytoplasmic actin layers, whereas this research utilized the vesicle shape and area of interaction with the cytoskeleton. All vesicles in which the effective viscosity was measured have been classified by vesicle type and, as shown in the supplemental material (Fig 2.11), there is no trend between vesicle type and effective viscosity.

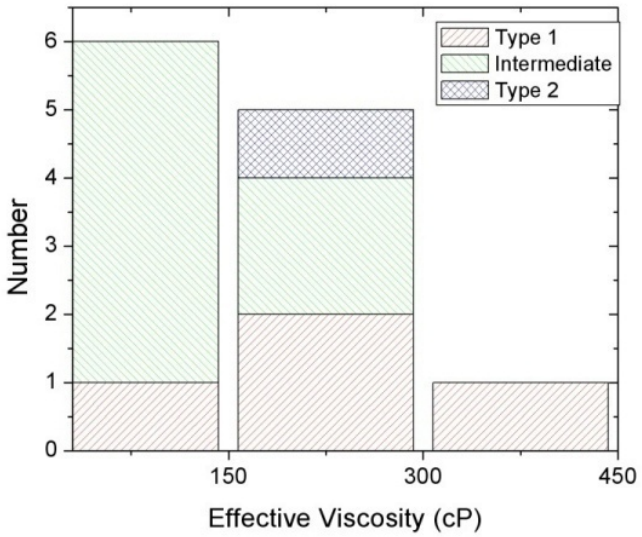

Figure 2.11. Histogram of measured effective viscosities broken down by GPMV type.

The highly spherical nature of the Type 1 vesicles suggests that the vesicles were under considerable surface tension and increased hydrostatic pressure as compared to the surrounding media. The hydrostatic pressure that maintains the vesicle's spherical shape and counteracts the membrane surface tension would also resist the net flow of material into the vesicle. However, individual concentration gradients may facilitate the flow of select species against this hydrostatic pressure gradient. Type 2 vesicles appear to be

under less hydrostatic pressure and/or have increased cytoskeletal framework to maintain non-spherical shapes. Annexin V staining indicates that the membrane surrounding all vesicles includes PS lipid molecules, although phalloidin staining shows no F-actin filaments in either vesicle type.

The diffusion of small particles through the GPMVs reveals fundamental characteristics of the vesicle rheology. The viscosity of the vesicle was determined to be 160 ± 110 cP. Due to the large number of beads confined to compartments less than 300 nm wide, not all beads could be analyzed with a 15 frames per second imaging rate. However, the beads that were confined describe the inner vesicle structure. Approximately 40% of the beads in GPMVs were highly confined and 60% were confined in structures greater than 300 nm in dimension. Since no trend was observed between area of confinement and measured viscosity, it is speculated that the structure composing the confinement edges was significantly different from the material within the confinement influencing the bead's apparently free diffusion. Since the observed viscosity of the vesicle's contents were approximately 50 fold higher than previously determined viscosity of the cytosol,[48, 49] we speculate that the diffusion of the beads was heavily influenced by the crowded environment within the vesicle, likely including an abundance of small molecules previously within the cytoplasm.[37, 50]

These results from the vesicles are useful in comparison to the motion of the beads within the cytoplasm before irradiation. All beads within the cytoplasm appeared to be highly confined to approximately 100 nm. Never was our setup capable of measuring the viscosity of the cytosol due to the high collision rate of the beads with

optically transparent, cytoplasmic structure. In comparison, the GPMVs contained significantly less obstructions to diffusion than the cytoplasm.

Observations of GFP, dextran, PI, and fluorescent beads reveal how material flows between the extracellular media, cytoplasm, and GPMV. As shown by the dextran and PI experiments, material goes from the media to the cytoplasm and to the vesicle (Fig. 3a-f). As shown by the GFP and the fluorescent beads, material goes from the cytoplasm to the vesicle (Fig. 2.4g-h and Fig. 2.8).

A substantial decrease in GFP signal was observed for the irradiated cell as compared to neighboring control cell (Fig. 2.4h). This suggests that there was an outflow of cytoplasmic material, particularly GFP, from the cell post-irradiation. The GFP was not observed in the surrounding media, but the fluorescence signal from such diluted GFP would be expected to be weak and unobservable under our imaging conditions. A possible caveat to the interpretation of the decreased fluorescence resulting from loss of cytoplasmic material is the possibility of differential photobleaching. However, we have no reason to expect photobleaching to be more pronounced in the irradiated *vs.* control cells.

2.3.2 GPMV actin contents

F-actin was in the GPMV, as determined by fluorescent phalloidin found within the GPMV (Fig. 2.5). Phalloidin was observed homogeneously throughout the GPMV without any filamentary structure at higher concentrations than phalloidin exists in the extracellular media. Phalloidin was an effective indicator of F-actin, as it is known to bind to F-actin, reduce the rate of actin filament depolymerization, and prevent conversion of F-actin to G-actin. It is not clear how the F-actin became distributed

throughout the vesicle since non-filamentary actin is expected to be in the G form and unavailable for phalloidin binding. We hypothesis the following progression: (1) the phalloidin enters the cytoplasm through the permeable plasma membrane of the irradiated cell and binds to F-actin filaments, (2) the osmotic and hydrostatic pressure imbalances that fuel the GPMV growth for extended periods of time induce gradual F-actin disassembly, and (3) the short segments of F-actin bound to phalloidin were flushed into the growing vesicle along with other small cytoplasmic particles. This hypothesis accommodates the common understandings of phalloidin activity with the observation of concentrated phalloidin and no filamentary structure within the vesicle.

At first glance, the fluorescent images presented in Fig. 2.5 do not clearly show that the fluorescence signal within the vesicle was directly due to phalloidin vs. a reflection/refraction of fluorescence from the GPMV. The illumination of non-fluorescing structures in close proximity to brightly fluorescing regions has been occasionally observed. However, in Fig. 2.5, the presence of control cells, in close proximity to the irradiated cells within the same micrograph, displays none of this reflection effect. These results demonstrate the power of the pulsed-laser irradiation method utilizing control cells in very close proximity to stressed cells. Considering the highly uniform distribution of PI and dextrans throughout GPMVs, the presence of refractive indices variations necessary for refraction seems unlikely however has not been fully disproven. Further, the presence of actin within vesicles has been suggested previously, although more so during mitosis and locomotion than during cell death,[51] with reduced connections to the vesicle wall.[52] Transmission electron micrographs of

irreversible vesicles caused by oxidative stress have previously demonstrated the presence of low density cytoplasmic material throughout the vesicle.[53]

2.3.3 GPMV formation processes

The contributing factors to the initiation of the GPMV formation process in cells can be roughly divided into two types: physical stimuli (*e.g.* pressure and heat) and biochemical stimuli (*e.g.* caspase activity, actomyosin alterations, etc.). The biochemical stimuli of the apoptotic GPMV formation cascade most likely incorporate caspase-3, Rho, myosin, and actin reorganization. The biochemical mechanisms of vesicle formation were tested through the examination of irradiation in caspase-3 deficient, MCF-7 cells. Although caspase-3 has been shown to be highly influential in the vesicle formation process associated with programmed cell death,[4, 11, 54] no variation in vesicle formation or R110-AAA_2 cleavage was observed in MCF-7 versus other epithelial cells subjected to irradiation. Further, MCF-7 cells were incubated with Z-VAD-fmk to inhibit all caspase activity, and still vesicle formation progressed normally post-irradiation. This result concludes caspase activity was not essential for irradiation induced GPMV formation and emphasizes the importance of physical stimuli while demonstrating caspase activity was not essential for laser-induced GPMV formation.

Physical stimuli were initiated by the micro-bubble formation as result of the multiphoton absorption within the laser focal spot, which generates increased pressure and heat within the cytoplasm. Physical stimuli, such as applied hydrostatic pressure gradients on the plasma membrane, previously have been shown sufficient to induce GPMV formation.[5, 8-10, 12, 13, 17] We have identified two likely components to the physical stimuli of irradiation resulting in vesicle formation: rupture and osmotic pressure

gradients. The rupture component consists of micro-bubble formation causing a large pressure increase within the cytoplasm that breaks the plasma membrane-cytoskeleton interface. As a result, the plasma membrane loses its structural support and GPMVs form as a result of the cell's natural pressure gradients no longer being counteracted by the cytoskeleton. The osmotic pressure component originates from the micro-bubble formation inducing actin depolymerization and significant osmotic pressure increase within the cell. The increased osmotic pressure gradient was relieved by the incorporation of surrounding media into the cytoplasm. However, the influx of fluids into the cytoplasm results in an increase in hydrostatic pressure, which in turn was relieved through vesicle formation. Since the micro-bubble condenses onto itself within seconds after irradiation, the micro-bubble itself could not be the sustained pressure source to promote vesicle growth. Although the relative importance of these two vesicle formation mechanisms cannot be directly observed, comparison to other cellular stressors indicates both vesicle formation mechanisms are important in GPMV formation.

By exposing the cells to other stressors, we have been able to determine that osmotic forces or physical disruption were separately sufficient to induce GPMV formation. By exposing the cells to a hypotonic solution, the cells increase in volume but did not commonly form distinct vesicles. This indicates that osmotic forces alone are not sufficient to induce GPMV formation.

A physical rupture via the poking of the cell with a micron-sized microinjection needle was sufficient to induce vesicle formation. The primary effect of the poking was likely to break the cortical actin support of the plasma membrane via a compression of the cytoplasm and hydrostatic pressure increases. However, this poking event may have

also depolymerized cytoplasmic proteins and caused an osmotic pressure gradient as a secondary effect. In conclusion, both the physical disruption of the cytoskeletal structure and the osmotic pressure gradients likely contribute to the observed laser-induced GPMV formation.

In summary, femtosecond laser irradiation was utilized to perturb living cells and create GPMVs. The vesicles were determined to be membrane bound fluid sacks that incorporate PI, 10 kDa and 40 kDa dextran from the surrounding media as well as F-actin, GFP, and 65 nm fluorescent beads from the cytoplasm. Reduced GFP fluorescence of the irradiated cell relative to the neighboring control cells suggests that cytoplasmic contents were released by the irradiated cell into the surrounding media. Phalloidin bound to F-actin was found in the GPMVs, although evenly dispersed throughout the vesicle and not as long filaments. Laser irradiation initiated caspase activity, which in turn caused R110-AAA_2 cleavage, although caspase activity was not required for the vesicle formation process. 65 nm diameter beads were occasionally incorporated into the vesicles and single particle tracking reveals that the majority of vesicles contain obstacles to free diffusion and the effective viscosity varies from 32 to 434 cP, with lower viscosities occurring more frequently. These results give a better understanding of the effects of pulsed-laser irradiation of cells, the GPMV formation process, and the properties of the resulting GPMVs.

2.4 MATERIALS AND METHODS

2.4.1 Cell lines

Multiple cell lines were examined to determine the generality of these results, including continuous human epithelial lines (KB, FaDu, A431, MCF-7, MCA-207, Jar, Jeg-3), primary epithelial lines (UMSCC-22A), rat fibroblasts (Rat2), and mouse red blood cells. All cells were obtained in collaboration with the Michigan Nanotechnology Institute for Medicine and Biological Sciences (MNIMBS) via the American Type Culture Collection (ATCC) or MNIMBS staff. MCF-7 cells are unique among this set because they are deficient in caspase-3 activity.[54] GFP-transfected KB and MCA-207 cells were obtained from MNIMBS, although most of the KB cells used in this study were not transfected with GFP. KB cells were employed for the majority of these studies, unless otherwise stated, because of our extensive experience with studies of membrane permeability for this cell line.[55, 56] KB cells are a HeLa-contaminant and were grown as a monolayer at 37 °C and 5% CO_2 in RPMI 1640 medium (Mediatech, Inc.) with 10% Fetal Bovine Serum and 1% penicillin/streptomycin on 75 cm^2 tissue culture flasks. At each splitting, 10^5 cells are plated to 35 mm diameter dishes (MatTek Corp.) with a 0.17 mm thick glass bottom for high numerical aperture microscopy. All experiments were performed at 37 ºC and repeated on a minimum of twelve individually irradiated cells over a variety of cell passages.

2.4.2 Fluorochromes

Varieties of fluorescent molecules were employed in understanding the irradiation process and the cellular response. The propidium iodide (PI), 10 kDa anionic dextran-Alexa Fluor 488, 40 kDa anionic dextran-Alexa Fluor 488, Annexin V-Alexa Fluor 488, Rhodamine 110 bis-(L-aspartic acid amide) (R110-AAA_2), and phalloidin-Alexa Fluor 488 were obtained from Invitrogen Corp. and detailed explanation of their *in vitro*

behavior is available from the supplier. Dyes were employed as follows: PI was added to the cell media at various times (2 hr before to 2 hr after irradiation) and various concentrations (1-10 μg/mL) with identical staining pattern in all vesicle forming cells; Dextran was added to the cell solution at a concentration of 25 mg/mL more than 10 min before irradiation and rinsed off with PBS after irradiation; Annexin V in PBS (10 μL : 2 mL) was added to the cells 40 min before irradiation, 40 min after irradiation, or some time in between to test the timing of PS externalization; 60 μM R110-AAA_2 in PBS was added to the cells 45 min before irradiation; 210 nM Phalloidin-Alexa Fluor 488 in PBS was added to the cells 20 min before irradiation, 40 min after irradiation, or some time in between and was occasionally replaced with fresh PBS after irradiation.

2.4.3 PS localization

Annexin V-Alexa Fluor 488 was inserted through both microinjection and electroporation into the cytoplasm to fluorescently tag PS within the cytoplasm of KB cells. Microinjection was performed with a Femtojet (Eppendorff, Inc.) on an inverted microscope with 1:50 mixture of Annexin V in 0.02 μm filtered binding buffer on four different days to over 50 different cells. Electroporation was performed with a Nucleofector (Amaxa, Inc.) following the HeLa cell protocol in a 1:250 Annexin V in binding buffer solution on six different experiments over three different days.

2.4.4. Caspase inhibition

Z-Val-Ala-Asp(OCH_3)-Fluoromethylketone (Z-VAD-fmk, Biomol International L.P.) was employed to further test caspase activity in irradiated cells. This broad-spectrum caspase inhibitor has been shown to highly limit the induction of caspase activity upon cellular stresses.[4, 57, 58] MCF-7 cells were occasionally incubated with 22

μM Z-VAD-fmk in PBS for 2 hr before irradiation. Z-VAD-fmk was rinsed off with fresh PBS before irradiation and occasional R110-AAA_2 addition.

2.4.5 Microscopy setup

For single particle tracking (SPT), epifluorescent micrographs with 680 x 512 pixel resolution were captured at 15 frames/sec for up to 40 sec duration with an Olympus DP30 cooled CCD camera on an Olympus IX81 inverted microscope with computer control through Olympus DP and Microsuite software (Fig 2.12). A 100x oil-immersion, 1.35 NA Olympus UPlanAPO objective was utilized to view the cells through collagen coated glass bottom 35 mm dishes. Fluorescent images were processed with GIF Movie Gear (Gamani Productions), Photoshop CE (Adobe Systems, Inc.), and Matlab (Mathworks, Inc.) to digitally zoom in, adjust contrast and brightness of the entire image, and track the fluorescent beads.

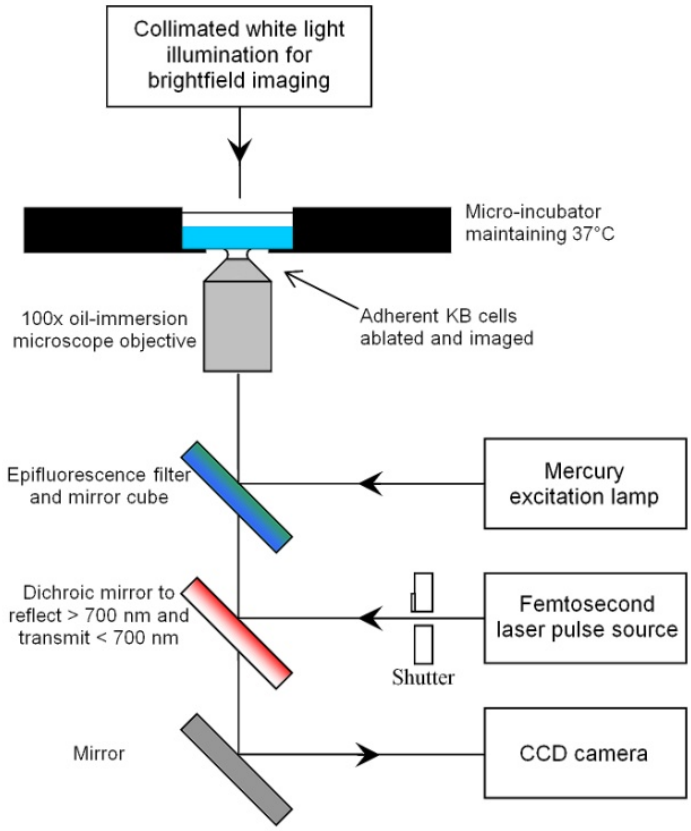

Figure 2.12. Experimental setup incorporating an inverted fluorescent microscope with femtosecond 790 nm laser pulses. The CCD camera captures high resolution grey scale images of the sample, as focused by the 100x oil-immersion objective.

2.4.6 Cell stressors

Mechanistic comparisons between laser irradiation and other cellular stressors are analyzed, including exposure to low intensity ultraviolet (UV) light, physical rupture with a micron sized needle, and exposure to hypotonic solutions. The UV light irradiation is a broad spectrum source commonly used for disinfection of laboratory supplies and exposed to cells for 20 ± 10 min. The physical rupture of the cells is performed by the micromanipulator-control of a microinjection needle to poke the cells. There was no flow into or out of the needle during these poking experiments. The hypotonic solution

was high purity water (NERL Diagnostics). Cells were exposed to the hypotonic solution for 1 hr.

2.4.7 Laser setup

The laser system consisted of a solid state pumped (Verdi [532 nm, Coherent, Inc.]) passively mode-locked Ti:sapphire laser (Femtosource Scientific [Femtolasers, Inc.]). Resulting pulses had a central wavelength of 790 nm with a FWHM of 115 nm, repetition rate of 90 MHz, and compressed pulse duration of 9 fs, and 4 nJ/pulse. The pulses were compressed to near transform limited pulse duration immediately after the laser oscillator and experienced temporal stretching due to group-velocity dispersion as they traveled to the microscope and through the objective into the sample. Tadepalli *et al*. examined a very similar setup and measured the stretched pulse duration on the sample is 62 fs at the objective focus.[59]

Laser pulses were reflected into the 100x oil-immersion inverted microscope objective with a dichromatic mirror, reflecting wavelengths > 700 nm into the objective while transmitting wavelengths < 700 nm from the sample to the CCD camera (Fig 2.10). Laser irradiation of cells was controlled with a SH-05 beam shutter (Thorlabs, Inc.) to expose cells to the laser pulses for 0.1 sec intervals.

2.4.8 Fluorescent beads

Fluorescent beads (Duke Scientific Corp.) were incubated with cells at 3.7 mg/mL for 3 to 5 hr before irradiation. The beads were 65 nm diameter polystyrene, carboxylic acid coated, and fluorescent at wavelengths similar to fluorescein (absorb at 490 nm, emit at 520 nm). Beads are expected to be very homogeneous because these they are also sold as a standard for use in particle sizing applications. Within the cell, the carboxylic acid

coated beads may change size and surface considerably. This is a common problem with the incorporation of any well characterized material into a biological system and has been previously referred to as a "corona."[60] This corona does add to the uncertainty of these results, but typically protein layers that do not exceed ~1 nm. With the diffusion constant depending linearly on the particle radius, this increase in radii is not sufficient to explain the over 10 fold variation in observed diffusion rates. Bead internalization occurred spontaneously during incubation, presumably under similar mechanisms to previously reported endocytic pathways of bead internalization.[61] The cells were rinsed to remove extracellular beads prior to laser irradiation and fluorescence examination.

2.4.9. Diffusion theory

GPMV structure and viscosity were quantified through the tracking of single, diffusive fluorescent beads within the vesicle. By tracking a single particle over time, the position, x(t), of the particle was determined. The mean-square displacement, MSD, of the particle's position is proportional to the time step, Δt, such that

$$MSD(\Delta t) = <|\mathbf{x}(t) - \mathbf{x}(t+\Delta t)|^2>_t = 2nD\Delta t \quad (1)$$

where D is the diffusion constant and n is the system dimensionality (*e.g.* 1D, 2D, or 3D), as summarised in Table 1. Within our system, only the horizontal position of the bead was tracked as the bead's vertical position was not quantified; thus $n = 2$. The viscosity, μ, of the surrounding media can also be calculated by measuring x(t) of a particle of known radius, r, according to

$$\mu = \frac{k_B T}{2\pi n D r} \ , \quad (2)$$

with Boltzmann's constant, k_B, and temperature, T.

2.4.10 Diffusion terminology

The observed viscosities in cells have been shown to vary greatly with the size of the diffusing probe used.[37, 38, 48, 50] The term "true viscosity" is reserved for the observed viscosity of a very small particle (≤ 1 nm radius), while the term "effective viscosity" is used to represent the observed viscosity of larger particles. Commonly effective viscosities can be orders of magnitude higher than true viscosities due to a filtering effect in some materials that allow free diffusion of small particles and restricted motion of larger particles. For example, Luby-Phelps *et al*.[48] demonstrated the cytoplasm was more than a crowded protein environment and contained filamentary structure restricting diffusion through the examination of fluorescent dextran with fluorescence recovery after photobleaching (FRAP).

2.4.11. Trajectory analysis

Beads were tracked through custom-made Matlab software by identification of the fluorescent centroid and proper bead tracking was visually confirmed for sub-pixel resolution of bead location to ± 50 nm in each of the two lateral dimensions. The height of the particle was not tracked and thus only diffusion in two dimensions was analyzed. MSD(Δt) is plotted for all tracked particles and a linear fitting was determined to the values of MSD($2\delta t$), MSD($3\delta t$), and MSD($4\delta t$). The tracking of beads in glycerol-water mixtures allowed for error analysis of the setup and demonstrated 8% random error in our results (Fig. 2.13). For those particles that showed considerable curvature for $\Delta t \leq 4\delta t$, it was determined that δt is too slow compared to the collision rate of the particle to the surrounding obstacles and diffusion constant could not be accurately determined. This ratio of δt to collision rate limited the smallest confinement dimensions possible to be analyzed by our methods to ~300 nm.

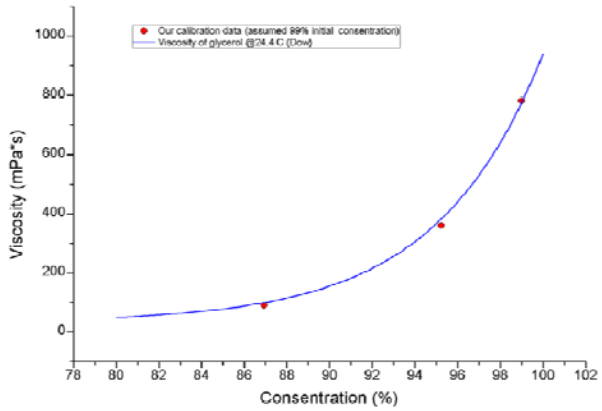

Figure 2.13. The calculated viscosity of water-glycerin mixtures from single particle tracking as compared to expected viscosities. 8% random error is observed for solution viscosities ranging from 40 to 800 cP.

2.5. ACKNOWLEDGMENTS

Mary-Margaret T. Kober, Päivö Kinnunen, David A. Reis, Bradford G. Orr, and Mark M. Banaszak Holl made essential contributions to this research. Partial support for this project was provided by the Michigan Nanotechnology Institute for Medicine and Biological Sciences, the National Institute of Biomedical Imaging and Bioengineering (R01-EB005028), and by the NSF Frontiers in Physics FOCUS Center under grant PHY-0114336. Fellowship support was received from the NIH Michigan Molecular Biophysics Training Program (T32 GM008270-20), the Applied Physics program, and the Graham Environmental Sustainability Institute. The authors thank Meghan Liroff, Tom Dunham, Pascale Leroueil, Kevin McDonough, and Alina Kotlya.

2.6. REFERENCES

1. Barros, L. F.; Kanaseki, T.; Sabirov, R.; Morishima, S.; Castro, J.; Bittner, C. X.; Maeno, E.; Ando-Akatsuka, Y.; Okada, Y., Apoptotic and necrotic blebs in epithelial cells display similar neck diameters but different kinase dependency. *Cell Death and Differentiation* **2003,** 10, (6), 687-697.
2. Hagmann, J.; Burger, M. M.; Dagan, D., Regulation of plasma membrane blebbing by the cytoskeleton. *Journal of Cellular Biochemistry* **1999,** 73, (4), 488-499.
3. Huot, J.; Houle, F.; Rousseau, S.; Deschesnes, R. G.; Shah, G. M.; Landry, J., SAPK2/p38-dependent F-actin reorganization regulates early membrane blebbing during stress-induced apoptosis. *Journal of Cell Biology* **1998,** 143, (5), 1361-1373.
4. Mills, J. C.; Stone, N. L.; Erhardt, J.; Pittman, R. N., Apoptotic membrane blebbing is regulated by myosin light chain phosphorylation. *Journal of Cell Biology* **1998,** 140, (3), 627-636.
5. Paluch, E.; Piel, M.; Prost, J.; Bornens, M.; Sykes, C., Cortical actomyosin breakage triggers shape oscillations in cells and cell fragments. *Biophysical Journal* **2005,** 89, (1), 724-733.
6. Paluch, E.; Sykes, C.; Prost, J.; Bornens, M., Dynamic modes of the cortical actomyosin gel during cell locomotion and division. *Trends in Cell Biology* **2006,** 16, (1), 5-10.
7. Rafelski, S. M.; Theriot, J. A., Crawling toward a unified model of cell motility: Spatial and temporal regulation of actin dynamics. *Annual Review of Biochemistry* **2004,** 73, 209-239.
8. Dai, J. W.; Ting-Beall, H. P.; Hochmuth, R. M.; Sheetz, M. P.; Titus, M. A., Myosin I contributes to the generation of resting cortical tension. *Biophysical Journal* **1999,** 77, (2), 1168-1176.
9. Charras, G. T.; Yarrow, J. C.; Horton, M. A.; Mahadevan, L.; Mitchison, T. J., Non-equilibration of hydrostatic pressure in blebbing cells. *Nature* **2005,** 435, (7040), 365-369.
10. Rentsch, P. S.; Keller, H., Suction pressure can induce uncoupling of the plasma membrane from cortical actin. *European Journal of Cell Biology* **2000,** 79, 975-981.
11. Sebbagh, M.; Renvoize, C.; Hamelin, J.; Riche, N.; Bertoglio, J.; Breard, J., Caspase-3-mediated cleavage of ROCK I induces MLC phosphorylation and apoptotic membrane blebbing. *Nature Cell Biology* **2001,** 3, (4), 346-352.
12. Sheetz, M. P.; Sable, J. E.; Dobereiner, H. G., Continuous membrane-cytoskeleton adhesion requires continuous accommodation to lipid and cytoskeleton dynamics. *Annual Review of Biophysics and Biomolecular Structure* **2006,** 35, 417-434.
13. Yanai, M.; Kenyon, C. M.; Butler, J. P.; Macklem, P. T.; Kelly, S. M., Intracellular pressure is a motive force for cell motion in Amoeba proteus. *Cell Motility and the Cytoskeleton* **1996,** 33, (1), 22-29.
14. Sengupta, P.; Baird, B.; Holowka, D., Lipid rafts, fluid/fluid phase separation, and their relevance to plasma membrane structure and function. *Seminars in Cell & Developmental Biology* **2007,** 18, (5), 583-590.
15. Gores, G. J.; Herman, B.; Lemasters, J. J., Plasma-Membrane Bleb Formation and Rupture - a Common Feature of Hepatocellular Injury. *Hepatology* **1990,** 11, (4), 690-698.
16. Cunningham, C. C., Actin Polymerization and Intracellular Solvent Flow in Cell-Surface Blebbing. *Journal of Cell Biology* **1995,** 129, (6), 1589-1599.
17. Keller, H.; Rentsch, P.; Hagmann, J., Differences in cortical actin structure and dynamics document that different types of blebs are formed by distinct mechanisms. *Experimental Cell Research* **2002,** 277, (2), 161-172.
18. Paluch, E.; van der Gucht, J.; Sykes, C., Cracking up: symmetry breaking in cellular systems. *Journal of Cell Biology* **2006,** 175, (5), 687-692.

19. Jungbluth, A.; Vonarnim, V.; Biegelmann, E.; Humbel, B.; Schweiger, A.; Gerisch, G., Strong Increase in the Tyrosine Phosphorylation of Actin Upon Inhibition of Oxidative-Phosphorylation - Correlation with Reversible Rearrangements in the Actin Skeleton of Dictyostelium Cells. *Journal of Cell Science* **1994,** 107, 117-125.
20. Charras, G. T.; Hu, C. K.; Coughlin, M.; Mitchison, T. J., Reassembly of contractile actin cortex in cell blebs. *Journal of Cell Biology* **2006,** 175, (3), 477-490.
21. Malorni, W.; Straface, E.; Donelli, G.; Giacomoni, P. U., UV-induced cytoskeletal damage, surface blebbing and apoptosis are hindered by alpha-tocopherol in cultured human keratinocytes. *European Journal of Dermatology* **1996,** 6, (6), 414-420.
22. Vogel, A.; Noack, J.; Huttman, G.; Paltauf, G., Mechanisms of femtosecond laser nanosurgery of cells and tissues. *Applied Physics B-Lasers and Optics* **2005,** 81, (8), 1015-1047.
23. Shimada, T.; Watanabe, W.; Matsunaga, S.; Higashi, T.; Ishii, H.; Fukui, K.; Isobe, K.; Itoh, K., Intracellular disruption of mitochondria in a living HeLa cell with a 76-MHz femtosecond laser oscillator. *Optics Express* **2005,** 13, (24), 9869-9880.
24. Watanabe, W.; Arakawa, N.; Matsunaga, S.; Higashi, T.; Fukui, K.; Isobe, K.; Itoh, K., Femtosecond laser disruption of subcellular organelles in a living cell. *Optics Express* **2004,** 12, (18), 4203-4213.
25. Konig, K.; Riemann, I.; Fischer, P.; Halbhuber, K. H., Intracellular nanosurgery with near infrared femtosecond laser pulses. *Cellular and Molecular Biology* **1999,** 45, (2), 195-201.
26. Konig, K.; Riemann, I.; Fritzsche, W., Nanodissection of human chromosomes with near-infrared femtosecond laser pulses. *Optics Letters* **2001,** 26, (11), 819-821.
27. Heisterkamp, A.; Maxwell, I. Z.; Mazur, E.; Underwood, J. M.; Nickerson, J. A.; Kumar, S.; Ingber, D. E., Pulse energy dependence of subcellular dissection by femtosecond laser pulses. *Optics Express* **2005,** 13, (10), 3690-3696.
28. Kumar, S.; Maxwell, I. Z.; Heisterkamp, A.; Polte, T. R.; Lele, T. P.; Salanga, M.; Mazur, E.; Ingber, D. E., Viscoelastic retraction of single living stress fibers and its impact on cell shape, cytoskeletal organization, and extracellular matrix mechanics. *Biophysical Journal* **2006,** 90, (10), 3762-3773.
29. Tirlapur, U. K.; Konig, K., Cell biology - Targeted transfection by femtosecond laser. *Nature* **2002,** 418, (6895), 290-291.
30. Stracke, F.; Rieman, I.; Konig, K., Optical nanoinjection of macromolecules into vital cells. *Journal of Photochemistry and Photobiology B-Biology* **2005,** 81, (3), 136-142.
31. Stavitskaya, E. Y.; Egorova, A. B.; Salmin, V. V.; Zobova, S. N.; Provorov, A. S., Modification of membrane-toxic effect of Nd-YAG laser by preliminary induction of cytochrome P-450 in bone marrow cells. *Bulletin of Experimental Biology and Medicine* **2001,** 132, (2), 811-813.
32. Supatto, W.; Debarre, D.; Moulia, B.; Brouzes, E.; Martin, J. L.; Farge, E.; Beaurepaire, E., In vivo modulation of morphogenetic movements in Drosophila embryos with femtosecond laser pulses. *Proceedings of the National Academy of Sciences of the United States of America* **2005,** 102, (4), 1047-1052.
33. Cicuta, P.; Donald, A., Microrheology: a review of the method and applications. *Soft Matter* **2007,** 3, 1449-1455.
34. Kural, C.; Serpinskaya, A. S.; Chou, Y. H.; Goldman, R. D.; Gelfand, V. I.; Selvin, P. R., Tracking melanosomes inside a cell to study molecular motors and their interaction. *Proceedings of the National Academy of Sciences of the United States of America* **2007,** 104, (13), 5378-5382.
35. Kural, C.; Kim, H.; Syed, S.; Goshima, G.; Gelfand, V. I.; Selvin, P. R., Kinesin and dynein move a peroxisome in vivo: A tug-of-war or coordinated movement? *Science* **2005,** 308, (5727), 1469-1472.

36. Kim, S. Y.; Gitai, Z.; Kinkhabwala, A.; Shapiro, L.; Moerner, W. E., Single molecules of the bacterial actin MreB undergo directed treadmilling motion in Caulobacter crescentus. *Proceedings of the National Academy of Sciences of the United States of America* **2006,** 103, (29), 10929-10934.
37. Banks, D. S.; Fradin, C., Anomalous diffusion of proteins due to molecular crowding. *Biophysical Journal* **2005,** 89, (5), 2960-2971.
38. Guigas, G.; Kalla, C.; Weiss, M., Probing the nanoscale viscoelasticity of intracellular fluids in living cells. *Biophysical Journal* **2007,** 93, (1), 316-323.
39. Zohdy, M. J.; Tse, C.; Ye, J. Y.; O'Donnell, M., Optical and acoustic detection of laser-generated microbubbles in single cells. *IEEE Transactions on Ultrasonics Ferroelectrics and Frequency Control* **2006,** 53, (1), 117-125.
40. Vogel, A.; Linz, N.; Freidank, S.; Paltauf, G., Femtosecond-laser-induced nanocavitation in water: Implications for optical breakdown threshold and cell surgery. *Physical Review Letters* **2008,** 100, (3), 4.
41. Alberts, B.; Johnson, A.; Lewis, J.; Raff, M.; Roberts, K.; Walter, P., *Molecular Biology of the Cell*. 4th ed.; Garland Publishing: New York, NY, 2002.
42. Vogel, G.; Thilo, L.; Schwarz, H.; Steinhart, R., Mechanism of Phagocytosis in Dictyostelium-Discoideum - Phagocytosis Is Mediated by Different Recognition Sites as Disclosed by Mutants with Altered Phagocytotic Properties. *Journal of Cell Biology* **1980,** 86, (2), 456-465.
43. Faulstich, H.; Zobeley, S.; Heintz, D.; Drewes, G., Probing the Phalloidin Binding-Site of Actin. *Febs Letters* **1993,** 318, (3), 218-222.
44. Isenburg, G., Actin binding-proteins lipid interactions. *Journal of Muscle Research and Cell Motility* **1991,** 12, (2), 136-144.
45. Cunningham, C. C.; Gorlin, J. B.; Kwiatkowski, D. J.; Hartwig, J. H.; Janmey, P. A.; Byers, H. R.; Stossel, T. P., Actin-Binding Protein Requirement for Cortical Stability and Efficient Locomotion. *Science* **1992,** 255, (5042), 325-327.
46. Veatch, S. L.; Cicuta, P.; Sengupta, P.; Honerkamp-Smith, A.; Holowka, D.; Baird, B., Critical fluctuations in plasma membrane vesicles. *Acs Chemical Biology* **2008,** 3, (5), 287-293.
47. Baumgart, T.; Hammond, A. T.; Sengupta, P.; Hess, S. T.; Holowka, D. A.; Baird, B. A.; Webb, W. W., Large-scale fluid/fluid phase separation of proteins and lipids in giant plasma membrane vesicles. *Proceedings of the National Academy of Sciences of the United States of America* **2007,** 104, (9), 3165-3170.
48. Luby-Phelps, K.; Taylor, D. L.; Lanni, F., Probing the Structure of Cytoplasm. *Journal of Cell Biology* **1986,** 102, (6), 2015-2022.
49. Mastro, A. M.; Keith, A. D., Diffusion in teh aqueous compartment. *Journal of Cell Biology* **1984,** 99, (1), S180-S187.
50. Weiss, M.; Elsner, M.; Kartberg, F.; Nilsson, T., Anomalous subdiffusion is a measure for cytoplasmic crowding in living cells. *Biophysical Journal* **2004,** 87, (5), 3518-3524.
51. Laster, S. M.; Mackenzie, J. M., Bleb formation and F-actin distribution during mitosis and tumor necrosis factor-induced apoptosis. *Microscopy Research and Technique* **1996,** 34, (3), 272-280.
52. Tank, D. W.; Wu, E. S.; Webb, W. W., Enhanced Molecular Diffusibility in Muscle Membrane Blebs - Release of Lateral Constraints. *Journal of Cell Biology* **1982,** 92, (1), 207-212.
53. Miyoshi, H.; Umeshita, K.; Sakon, M.; ImajohOhmi, S.; Fujitani, K.; Gotoh, M.; Oiki, E.; Kambayashi, J.; Monden, M., Calpain activation in plasma membrane bleb formation during tert-butyl hydroperoxide-induced rat hepatocyte injury. *Gastroenterology* **1996,** 110, (6), 1897-1904.

54. Janicke, R. U.; Sprengart, M. L.; Wati, M. R.; Porter, A. G., Caspase-3 is required for DNA fragmentation and morphological changes associated with apoptosis. *Journal of Biological Chemistry* **1998,** 273, (16), 9357-9360.
55. Hong, S. P.; Bielinska, A. U.; Mecke, A.; Keszler, B.; Beals, J. L.; Shi, X. Y.; Balogh, L.; Orr, B. G.; Baker, J. R.; Holl, M. M. B., Interaction of poly(amidoamine) dendrimers with supported lipid bilayers and cells: Hole formation and the relation to transport. *Bioconjugate Chemistry* **2004,** 15, (4), 774-782.
56. Hong, S. P.; Leroueil, P. R.; Janus, E. K.; Peters, J. L.; Kober, M. M.; Islam, M. T.; Orr, B. G.; Baker, J. R.; Holl, M. M. B., Interaction of polycationic polymers with supported lipid bilayers and cells: Nanoscale hole formation and enhanced membrane permeability. *Bioconjugate Chemistry* **2006,** 17, (3), 728-734.
57. Janicke, R. U.; Ng, P.; Sprengart, M. L.; Porter, A. G., Caspase-3 is required for alpha-fodrin cleavage but dispensable for cleavage of other death substrates in apoptosis. *Journal of Biological Chemistry* **1998,** 273, (25), 15540-15545.
58. McCarthy, N. J.; Whyte, M. K. B.; Gilbert, C. S.; Evan, G. I., Inhibition of Ced-3/ICE-related proteases does not prevent cell death induced by oncogenes, DNA damage, or the Bcl-2 homologue Bak. *Journal of Cell Biology* **1997,** 136, (1), 215-227.
59. Tadepalli, N. R.; Alexander, D.; Doerr, D.; Li, J.; Zhang, H., Femtosecond pulse stretching in microscope objectives used for micro/nanomachining. *Journal of Laser Applications* **2005,** 17, (4), 270-272.
60. Lynch, I.; Dawson, K. A.; Linse, S., Detecting Cryptic Epitopes Created by Nanoparticles. *Science STKE* **2006,** 327, pe14.
61. Reece, J. C.; Vardaxis, N. J.; Marshall, J. A.; Crowe, S. M.; Cameron, P. U., Uptake of HIV and latex particles by fresh and cultured dendritic cells and monocytes. *Immunology and Cell Biology* **2001,** 79, (3), 255-263.

CHAPTER 3

STOICHIOMETRY AND STRUCTURE OF POLY(AMIDOAMINE) DENDRIMER-LIPID COMPLEXES

3.1. INTRODUCTION

Understanding the interaction of nanoparticles with the plasma membrane of living cells is of fundamental importance for designing medical therapeutics, as well as for predicting effects from environmental exposure. Poly(amidoamine) (PAMAM) dendrimers are advantageous in applications and as a test system due to their uniformity, aqueous solubility, easily modified surface chemistry, and controlled size.[1] For targeted therapeutics, a minimal dendrimer-membrane interaction is preferred to avoid interfering with the targeting moieties.[2-6] Systemic therapeutics, such as transfection vectors, require a strong dendrimer-membrane interaction for enhanced delivery of the dendrimer's cargo through the plasma membrane and cytoplasmic barriers.[7-9] Additionally, the increasing commercial use of nanoparticles motivates an awareness of nanoparticle properties that are likely to yield adverse effects from environmental and human exposure.[10-13] Therefore, appropriate control of the nanoparticle-membrane interaction is an essential component of nanoparticle–based devices.

Previous research has identified the nanoparticle properties that are predictive of membrane disruption.[12-14] Specifically, nanoparticle net charge and surface area are the primary predictors of membrane disruption, more so than nanoparticle shape, flexibility,

or chemical composition.[12, 13] Membrane binding, pore formation, and leakage induced by cationic nanoparticles was demonstrated *in vivo*, *in vitro,* and on phospholipid model membranes.[8, 14-21] However, previous experiments were unable to resolve the molecular-scale details of the nanoparticle-membrane interaction.

Isothermal titration calorimetry (ITC) has been performed previously with PAMAM dendrimers and assorted surfactants, demonstrating strong dependence on dendrimer charge.[22, 23] Ionic bonding of anionic surfactants to the protonated amines was suggested as the primary mechanism of interaction and saturation was observed at charge neutrality. ITC has also been used for examination of the effects of nanoparticles on the stabilization and phase of phospholipid vesicles.[24, 25] To elucidate the details of dendrimer-lipid interactions, atomistic molecular dynamics,[26, 27] coarse-grained dynamics,[28-31] and mesoscale thermodynamic models[32, 33] have been used. All of these models demonstrate a strong dendrimer-lipid interaction. The atomistic models indicated the particular atomic moieties dominating the interaction, the thermodynamic models provided plausible continuum configurations, and the coarse-grained models provided the longest duration dynamics. However, no theoretical technique has yet been able to reproduce the generation dependence on membrane disruption observed experimentally while providing consistency of the limited deformability of the molecules. Interactions between the hydrophobic dendrimer moieties and the hydrophobic lipid tails have been identified in all models as important influences on the interaction of dendrimers with fluid phase bilayers.

The molecular mechanisms of nanoparticle-induced membrane disruption have been speculated to be (I) lipid vesicle enclosing the dendrimer(s),[33, 34] (II) lipid micelle

enclosing the dendrimer(s),[34] (III) a "carpeting" of the membrane by dendrimers,[35] or (IV) a barrel-stave mechanism of dendrimer supported membrane pores.[28, 30, 35] The latter two models were developed to explain membrane disruption induced by helical, amphiphilic peptides; however, these models have been adapted for deformable synthetic polymers.[30, 36] These models for the mechanisms of membrane degradation vary significantly in the number of lipids per dendrimer, the necessity of dendrimer cooperativity, and the predicted size of the resulting complex, as described in detail below (Figs. 2 and 5).

In this chapter, we examine dendrimer-lipid interactions through measuring enthalpy with ITC and the sizes of the resulting dendrimer-lipid complexes with AFM, TEM, MD, and DLS. These results are analyzed in terms of the stoichiometry and structure for the resulting dendrimer-lipid complex. Variations in dendrimer generation (G), dendrimer termination, and phospholipid head group were explored to describe dendrimer-dependent differences in binding to lipids. Within ITC, key dendrimer/lipid ratios of binding are identified by changes in the magnitude of the heat released. Upon mixing dendrimers and lipids, a change in enthalpy was only observed when both the dendrimers and the lipids had a net charge. For these interactions, both the stoichiometry and detailed energetics of the interaction were determined. The ratio of anionic phospholipids per dendrimer suggests that both dendrimer flattening and membrane curvature are induced to facilitate dendrimer-lipid contact. Analysis of calorimetry and microscopy data suggests that large dendrimers (> G6) form dendrimer-encased vesicle complexes either as a key component of larger dendrimer-lipid aggregates or as isolated complexes in solution (Model I, Fig. 3.2C and 5B). Whereas small- and medium-sized

dendrimers (≤ G6) interact with stoichiometries and structure consistent with a flattened-dendrimer model (Model III, Figs. 5A and 6).

3.2. RESULTS AND DISCUSSION

The ΔH of cationic dendrimer-anionic lipid interactions was primarily negative, indicating a net exothermic interaction, while cationic dendrimer-cationic lipid interactions were endothermic and zwitterionic lipids gave no heat release (Fig. 3.1). The overall curve shape of ΔH vs. n for cationic dendrimers and anionic lipids was likely the result of both an aggregation and supramolecular complex formation (Fig. 3.2). Three molar ratios are identified within each titration, n_A, n_L and n_D (with units of dendrimers/lipid), that provide insight into the dendrimer-lipid interaction. The molar ratio n_A represents the ratio at which the heat released per dendrimer reached the maximum. From the first injection of dendrimers into the solution of vesicles until a molar ratio of n_A, ΔH decreased as each added dendrimer released more heat than the previous. The molar ratio n_L represents the point ΔH began to increase and we hypothesize the system transitioned from a regime of abundant lipids to a regime of scarce lipids, as each injected dendrimer released less heat than the previous. The molar ratio n_D represents the smallest molar ratio at which ΔH was zero. We hypothesize the system transitioned from a regime of scarce dendrimers to abundant dendrimers at the molar ratio n_D. Following these hypotheses, at molar ratios less than n_L, there were few free dendrimers in solution since there were ample lipids to interact with all dendrimers in solution. At molar ratios greater than n_L, injected dendrimers were not able to release as much heat as those previously injected, hence the decreasing magnitude of ΔH. At

molar ratios greater than n_D, the free lipids were consumed by the dendrimers and there was no heat release due to dendrimer-lipid interactions upon further addition of dendrimers.

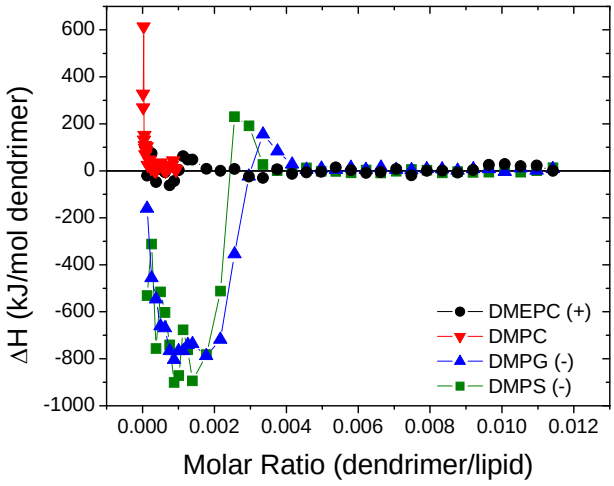

Figure 3.1. Change in enthalpy vs. molar ratio upon titration of G5 into various phospholipid SUVs at 50°C in PBS. The interaction of G5 and anionic lipids demonstrated significant heat release ($\Delta H < 0$) and a specific saturating stoichiometry after which no dendrimer-lipid interaction was observed. $\Delta H^0 = 0 \pm 10$ kJ/mol for the polycationic dendrimers and zwitterionic lipids. The polycationic polymer-cationic lipid interaction had only an initial endothermic interaction.

Repetitions of these experiments with varying initial concentrations revealed interesting trends. For a particular dendrimer generation, termination, and lipid type, the molar ratios at which ΔH went to zero (from n_L to n_D, Fig. 3.2A) was independent of the initial concentrations of dendrimers or lipids. In contrast, the molar ratios for which the initial decrease in ΔH occurred (0 to n_A, Fig. 3.2A) depended on the initial concentrations of dendrimers and lipids. We hypothesize the initial interaction of dendrimers and phospholipid vesicles was a flocculation, as previously reported,[8,37] and supported by DLS data (Fig. 3.3).

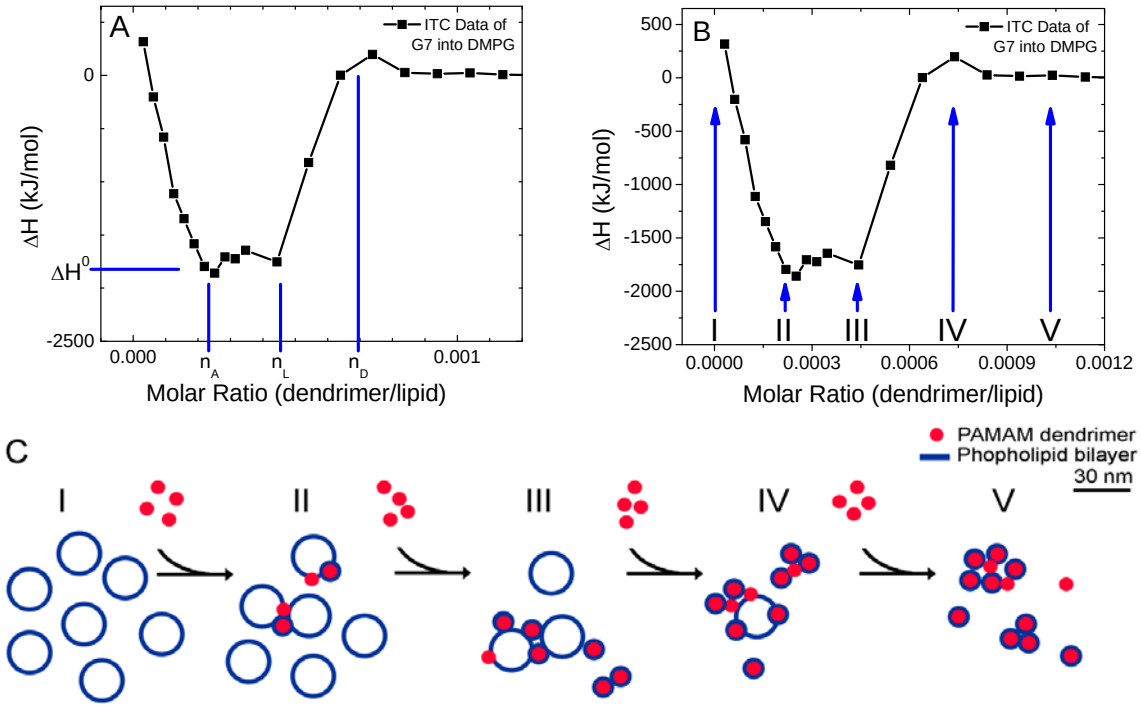

Figure 3.2. Analysis of ITC measured enthalpy vs. molar ratio. (A) As dendrimers were injected into the lipids, initially there were abundant lipids. The heat release per dendrimer increased as the lipid vesicles aggregated until the stoichiometric ratio of n_A. The heat release was equal to ΔH^0 between n_A and n_L. At the molar ratio n_L, the lipids became scarce and each injected dendrimer released less heat. At the molar ratio n_D, all the lipids were consumed and no further dendrimer-lipid interaction was observed. (B, C) The mixture of dendrimers with lipids vesicles resulted in aggregation as the dendrimers bind to the membranes. Further addition of dendrimers resulted in the formation of dendrimer-lipid complexes of well defined stoichiometry and continued flocculation and/or aggregation.

ΔH^0 of the dendrimer-lipid interaction is defined to be the maximum heat release measured throughout the titration. At the molar ratios for which ΔH^0 was measured (between n_A and n_L), there were lipid vesicles in solution available for interaction with each dendrimer. Titrations of polycationic G5 into anionic phospholipids, DMPS and DMPG, demonstrated a similar exothermic interaction (ΔH^0 = -800 ± 100 kJ/mol of G5, respectively) and complexation stoichiometries (Fig. 3.1). The heat absorbed upon interaction of G5 with DMPC, a zwitterionic lipid, is ΔH^0 = 0 ± 10 kJ/mol (Fig. 3.1).

Titrations of polycationic G5 and cationic DMEPC resulted in an initially endothermic interaction at low dendrimer/lipid ratios. Multiple initial injections with constant ΔH could not be observed even when increasing the relative lipid concentration up to 10^5 DMEPC/G5. A further discussion of the differences between types of phospholipids is given below.

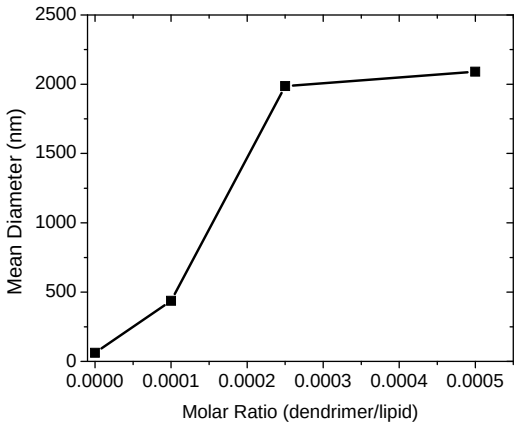

Figure 3.3. Mean diameter of G5-DMPS mixtures as measured with dynamic light scattering (DLS). DMPS was prepared into SUVs and measured upon addition of G5. This data was collected at 50 °C in PBS. Similar data has been obtained for G3, G5, and G8 in DMPG (not shown). The flocculation at higher dendrimer/lipid ratios causes aggregates too large for DLS analysis.

Interactions between DMPG and various PAMAM dendrimers were examined to determine the effects of polymer size and surface chemistry (Fig. 3.4). G3, G5, G5-Ac(40%), G5-Ac(100%), G6, G7, G8, and G9 were separately titrated into DMPG SUVs at 50°C. A greater number of primary amines per dendrimer yielded greater heat release and a greater number of lipids bound per dendrimer regardless of dendrimer generation or termination (Figs. 3 and 4).

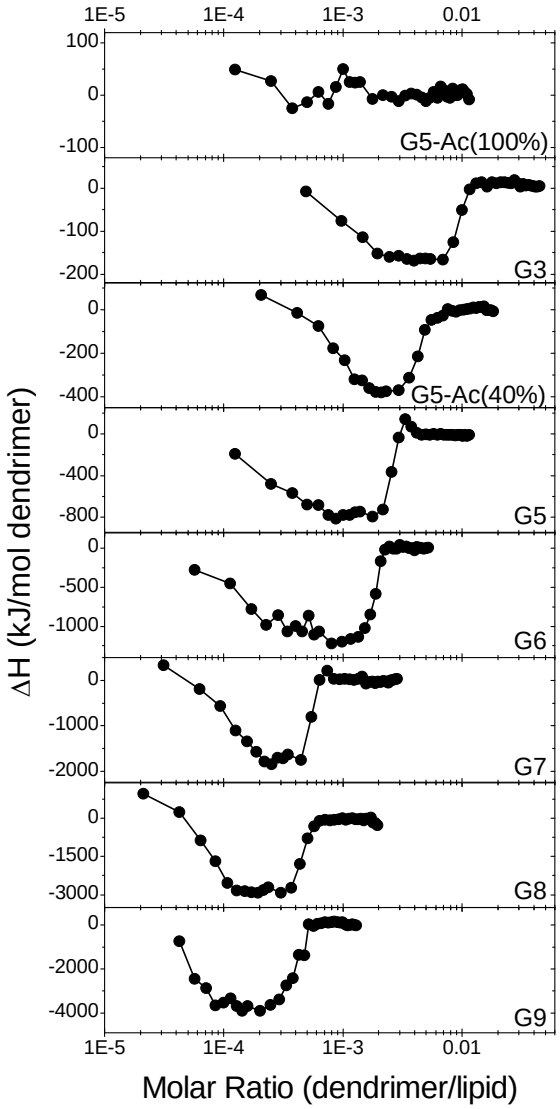

Figure 3.4. ΔH vs. molar ratio upon titration of assorted PAMAM dendrimers into DMPG SUVs at 50°C in PBS. Increasing the number of primary amines per dendrimer resulted in more lipids per dendrimer necessary for saturation and an increase in heat release (Fig. 3.5).

Small- and medium-sized polycationic dendrimers (≤ G6) released heat upon interacting with anionic phospholipids in linear proportion to the number of protonated primary amines per dendrimer. As shown in Fig. 3.5, linear fits to n_L^{-1}, n_D^{-1}, and ΔH^0 vs. the number of primary amines per dendrimer reveals that dendrimer-DMPG interaction can be characterized by 4.5 ± 0.1 lipids/primary amine, 2.2 ± 0.1 lipids/primary amine,

and -6.3 ± 0.3 kJ/ mol primary amine, respectively. Fig. 3.5 does not include analysis of n_A because n_A is dependent on the initial concentrations of dendrimers and lipids and is not a robust characteristic of the molecules studied. These binding stoichiometries, with greater than one lipid/primary amine, indicate that the binding is more complex than simple ionic binding, as previously observed with sodium dodecyl sulfate (SDS) and PAMAM dendrimers.[22]

The largest dendrimers, G8 and G9, displayed significant decreases in the energy and stoichiometry of lipid binding per dendrimer terminal group. This was presumably due to the decreased steric accessibility and reduced surface area per terminal group in these larger dendrimers. This demonstrates the interplay of the polymer size and the total number of primary amines per dendrimer in affecting the dendrimer-lipid interaction. Previous studies of PAMAM dendrimers and phospholipids, which indicated a strong dependence on the generation and termination of the dendrimers,[13, 14] are explained well by these observations of generation-dependent interactions with lipids.

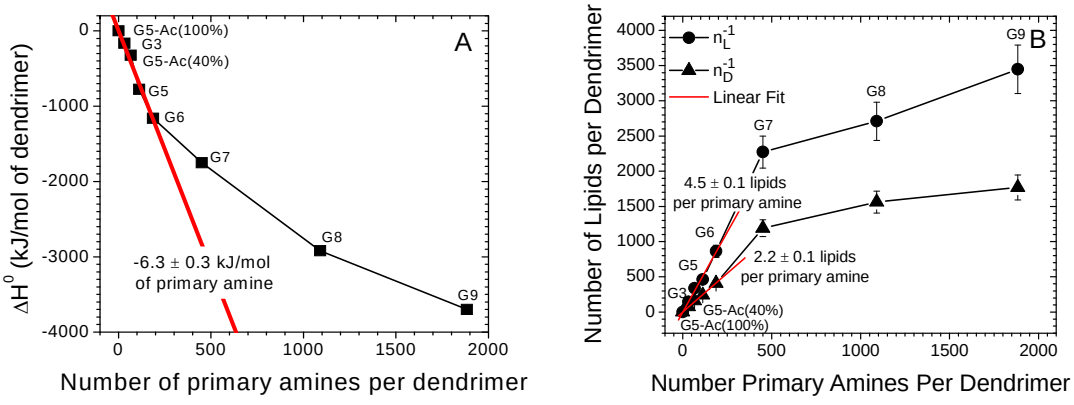

Figure 3.5. A scatter plot of the ΔH^0, n_L^{-1}, and n_D^{-1} versus the number of primary amines per dendrimer. Smaller dendrimers (< G7) had (A) maximum heat release and (B) binding stoichiometries proportional to the number of primary amines per dendrimer. The binding of larger dendrimers (> G7) required fewer lipids and provided less enthalpy

release per primary amine presumably due to the increasing density of primary amines on the dendrimer surface and steric limitations.

An explanation for the role of the dendrimer generation and termination on membrane disruption is given below to address the following questions of the resulting dendrimer-lipid complex.

- What are the dendrimer-lipid complexes that result from nanoparticle-induced membrane pore formation?
- Is the membrane *planar* on the length scale of a dendrimer or is there significant *curvature* around the dendrimer?
- Is the dendrimer located in the *hydrophobic* or *hydrophilic* region of the membrane?
- Does the dendrimer simultaneously interact with the surface of *one or two* vesicles?
- How does a lipid become *bound* to a dendrimer and unable to bind to another dendrimer?

Consideration of the lipids per dendrimer stoichiometry, the limited deformability of the dendrimer, and the density of the lipid bilayer addresses these questions. To bind to the lipids, as determined by ITC, means to interact with the lipids in such a way that heat is released and the lipids are associated with the dendrimer, limiting the lipids interaction with additional dendrimers. Once all of the lipids have been saturated by dendrimers, the further addition of dendrimers appears enthalpically identical to adding dendrimers to a solution deplete of lipids.

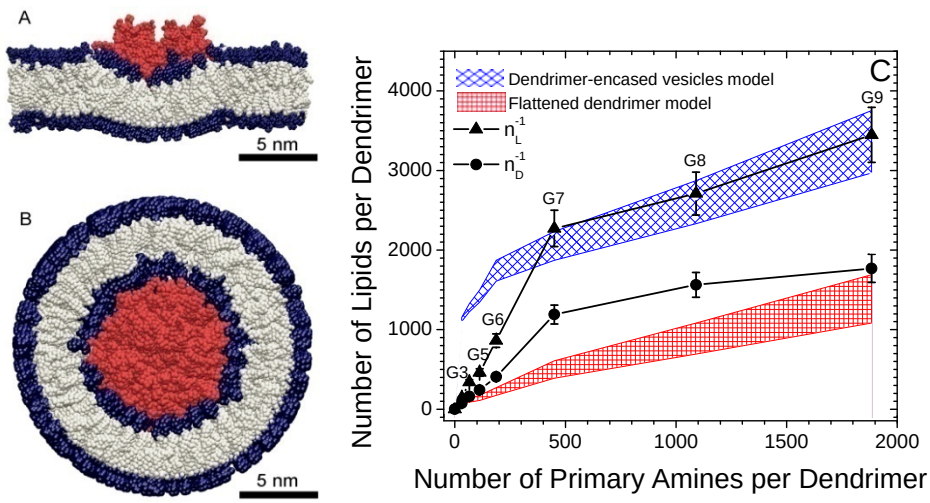

Figure 3.6. (A) Flattened-dendrimer model and (B) dendrimer-encased vesicle model of dendrimer lipid complexes. These models depict the interaction of a single dendrimer with a lipid bilayer and suggest a fundamental structure of local dendrimer-lipid interaction. Aggregation of the flattened dendrimers may induce sufficient curvature to create a separated vesicle and separated vesicles may readily aggregate. (C) ITC determined binding stoichiometries for the dendrimer-lipid complexes compared with the expected stoichiometry of these models. Small and medium dendrimers (< G6) flatten over the membrane, induce slight membrane curvature and/or flocculation of vesicles. Larger dendrimers (> G6) become encased by a lipid vesicle. (A) G5 and (B) G7 are colored red. The hydrophilic head groups are colored blue and the hydrophobic tails are colored grey. This data is also shown in Table 3.1.

One model of the dendrimer-lipid bilayer interaction includes the dendrimer flattening over the bilayer while the bilayer stays generally planar, the *flattened-dendrimer model* (Model III from above, Figs. 5A and 6). The molar ratio of lipids per dendrimer in this model depends on the area over which the dendrimers spans the bilayer. G3 PAMAM dendrimers have been observed by AFM flattening on a hard, anionic surface covering an area of 32 nm^2, at which time it is 1 nm tall.[38] With a DMPG monolayer density of 0.58 nm^2/lipid,[39] 110 lipids of a planar bilayer would be within the area of 32 nm^2. Similarly, atomistic molecular dynamics simulationshave measured G3 stretching over a fluid-disordered lipid bilayer where the dendrimer was in close

proximity to 56 lipid molecules on the top bilayer leaflet (Fig. 3.7); doubling this number to incorporate both leaflets yields 112 lipids/G3.[27] These estimates for the flattened dendrimer model are in good agreement with the ITC measured range of 76-140 lipids (n_D^{-1} to n_L^{-1}) for G3-DMPG.

Table 3.1. Stoichiometric comparison of ITC results and proposed dendrimer-lipid models

PAMAM Dendrimer	n_D^{-1}	n_L^{-1}	Flattened-dendrimer model [A,B]	Dendrimer-encased vesicle model [B,C]
	(lipids/dendrimer)			
G3	76	140	***70*** - ***110***	1100 - 1200
G5	240	460	***110*** - ***170***	1300 - 1500
G6	410	860	170 - 270	1600 - 1900
G7	1200	2300	390 - 610	***1900*** - ***2200***
G8	1600	2700	690 - 1100	***2300*** - ***2900***
G9	1800	3800	1100 - 1700	***3000*** - ***3800***

[A] Assuming a lipid density of 0.58 nm^2/lipid/monolayer and the maximum dendrimer extension on the surface equals that observed on mica under water.[39]
[B] Numbers in bold and italics indicate a general agreement between the model and the ITC-determined stoichiometries.
[C] Analogous to an estimate by Mecke et al.[34] with the minimum dendrimer radius equal to that observed in simulations.

The estimated number of lipids per dendrimer in the flattened-dendrimer model is shown in Fig. 3.6C. Varying experimental conditions yield a range of flattened dendrimers sizes, such as modifying the pH in AFM measurements,[38] the phase of the bilayer,[27] and the charge of the planar surface,[40] commonly with 20% variation in diameter of the flattened dendrimer. Thus, the number of lipids per dendrimer in the flattened dendrimer model is estimated for a range of dendrimer sizes within 20 % of the AFM measurement, which is taken to be the upper-limit on dendrimer deformability.

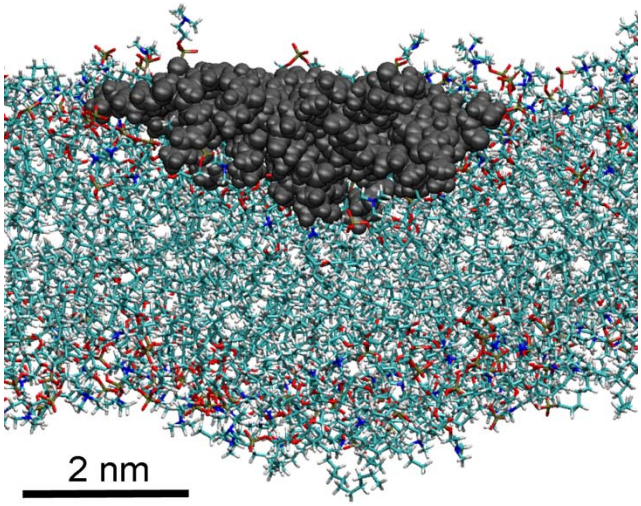

Figure 3.7. Molecular dynamics simulation result of G3 PAMAM dendrimer binding to a fluid-disordered phase DMPC bilayer. The dendrimer was within 3 Å of 56 lipid molecules. Doubling this to calculate the lipid molecules in the bilayer below the dendrimer yields 112 lipids/G3 and good agreement with ITC measured stoichiometries of 76-140 DMPG/G3.

The flattened-dendrimer model raises two important concerns: (1) how could the 1 nm tall dendrimer occupy both leaflets of the bilayer and (2) how does the membrane compensate for the large deformation energy required to flatten the dendrimer?[40] This first concern is alleviated by allowing the dendrimer to bind simultaneously to two separate bilayers, thereby achieving saturation by occupying leaflets from two different bilayers. This explanation is only feasible in solution experiments, such as those presented here, and not on a monolayer of adherent living cells or on a supported lipid bilayer. Another possibility is that the dendrimer sequesters into the tail region of the bilayer, binding to both leaflets of one bilayer simultaneously, as the precursor to a micelle.[32] The former option is expected if the dendrimer is found in the hydrophilic, head group region of the bilayers, while latter is expected if the dendrimer is found within the hydrophobic lipid tail region. ITC stoichiometric data cannot distinguish between these two possibilities, yet results from ITC on larger dendrimers (Fig. 3.6) and molecular

dynamics simulations (Fig. 3.7) indicate the dendrimers are found in a hydrophilic environment.

The second concern of energy balance is clarified by considering the energetics of a pore in a bilayer. The energy to make a large pore within a lipid bilayer can be estimated by the line tension multiplied by the pore contour length. Lipid bilayer line tension has been estimated to be 40 pN and the perimeter of a circular pore resulting from the removal of 100 lipids is 27 nm;[41] therefore, the energy required to form this pore would be approximately 650 kJ/mol. Since this value is greater than the energy necessary to flatten G3 (400 kJ/mol),[40] the flattened-dendrimer model is energetically consistent for G3 and DMPG. The membrane may accommodate the dendrimer by forming a pocket to reduce the dendrimer deformation, as shown previously[27] and in Figs. 5A and 6; however, this is not expected to cause pore formation from a single small dendrimer or significantly affect the estimates from the flattened-dendrimer model.

A similar analysis for G7 shows that the flattened-dendrimer model does not suffice to explain the ITC data. G7 on mica has been shown to stretch over 180 nm^2, corresponding to 610 lipids on a DMPG bilayer.[40] This is far fewer than the 1200-2300 lipids needed for saturation, as observed by ITC. Further, flattening G7 to 180 nm^2 requires 80,000 kJ/mol[40] and the removal of 2300 lipids from a membrane would require 3100 kJ/mol in the line tension and pore contour length. Thus, through both stoichiometric and energetic comparisons, G7 is not expected to reach the equilibrium stoichiometry by flattening on a planar bilayer.

A possible structure for the G7-DMPG complex is the *dendrimer-encased vesicle model* (Model I from above, Fig. 3.6B). This structure may be present as an isolated

supramolecular complex in solution or as a component of a larger dendrimer-lipid aggregate. This model is defined as a bilayer wrapped around each dendrimer as the dendrimer interacts with the hydrophilic surface of the membrane. The resulting dendrimer-encased vesicle(s) may stay bound to the larger vesicle structure or detach and create a membrane pore.[31] Regardless of the aggregated state of these structures, to maintain the average stoichiometry with this model, each dendrimer is on average individually wrapped by a bilayer of lipids and the diameter of a dendrimer-encased vesicle structure is approximately equal to the diameter of the dendrimer plus twice the bilayer thickness (Fig. 3.6B).

The number of lipids per vesicle encasing a G7 is estimated to be in the range of 1900 to 2200, in agreement with the 1200-2300 lipids/G7 observed via ITC (n_D^{-1} to n_L^{-1}). This estimate assumes the lateral lipid head group density and the lipid tail volume are equal to that of dendrimer-free lipid vesicles and the inner radius of the surrounding vesicle equal to the outer diameter of the dendrimer. The lower bound for the outer radius of the dendrimers is given by molecular dynamics simulations of dendrimers in solution without the incentive for the dendrimers to stretch to large sizes for greater interaction with the lipids. According to variations observed in small angle x-ray scattering, small angle neutron scattering, and molecular dynamics studies,[42] it is possible that the dendrimer could stretch as much as 20% to interact with more membrane surface, as represented in Fig. 3.6C. In this model, the dendrimer occupies both leaflets of a bilayer by inducing a highly convex membrane curvature on the vesicle exterior and limiting additional dendrimer binding to the outer leaflet. The induced membrane curvature is energetically costly due to the small radius of curvature, but encouraged by

the numerous dendrimer-membrane interactions. This energy compensation has been previously estimated[34] and dendrimers larger than or equal to G7 are energetically able to support such a dendrimer-encased vesicle complex.

Dendrimers of sixth-generation or smaller were not capable of individually supporting a surrounding vesicle. This conclusion is reached independently by either energetic or stoichiometric analysis. Stoichiometrically, the dendrimer-encased vesicle model for small dendrimers (≤ G6) is inconsistent with the ITC data (Fig. 3.6C). The number of lipids required to surround the dendrimer in a bilayer vesicle with an inner vesicle radius equal to the outer dendrimer radius, while preserving lateral head group area and lipid tail volume from dendrimer-free vesicles, is significantly more lipids per dendrimer than experimentally measured for these small dendrimers. For example, the estimated 1600-1900 lipids/dendrimer for a vesicle-encased G6 is significantly higher than the ITC measured 410-860 DMPG/G6. Thus, the dendrimer-encased vesicle model was not the average structure for individual dendrimers of sixth-generation or smaller.

The ITC results for G8 and G9 suggest the dendrimer-encased vesicle model for these generations of dendrimers as well. Due to the large size of G8 and G9, the encasing vesicles experienced less curvature and greater stabilization by the numerous primary amines per dendrimer. Furthermore, significant flattening of these 260 kDa and 410 kDa macromolecules was predicted to be energetically prohibited. The agreement between the stoichiometry observed via ITC and the predicted number of lipids per vesicle encasing the dendrimer provide the strongest evidence to date of the dendrimer-encased vesicle complex (Fig. 3.6).

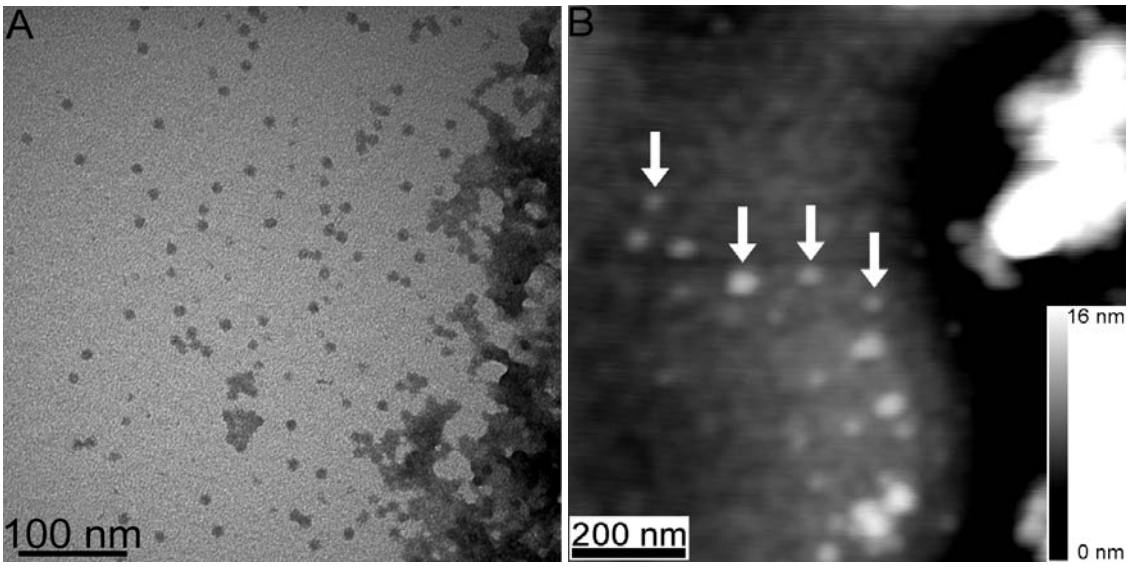

Figure 3.8. (A) TEM image of G8-DMPG complexes with a total molar ratio of n_L = 0.0003 G8/DMPG and (B) AFM measured topography of this sample. The uranyl acetate staining shows G8 may be isolated or in large aggregates. G8 appear dark and the lipids are not visible with this staining procedure. While TEM shows that each isolated complex contains primarily one G8, presumably the same complexes imaged by AFM (e.g. as indicated by arrows) have an average volume consistent with the dendrimer-encased vesicle model (Fig. 3.10).

TEM and AFM results show complexes in a mixture of G8 and DMPG consistent with the dendrimer-encased vesicle model. TEM images created with uranyl acetate stain reveal isolated G8, as well as regions of aggregated dendrimers. Aggregates were not visible in control samples of dendrimers or lipids alone and thus the aggregates are concluded to be a mixture of DMPG and G8. Due to staining and contrast constraints of TEM, lipid molecules in close proximity to the dendrimers were not visible (Fig. 3.8A and 8A). The complimentary technique of AFM was employed to measure the volume of the isolated dendrimer complexes with an average molar ratio of n_L (Fig. 3.8B). AFM experiments showed dendrimer-lipid aggregates as well as isolated complexes, in agreement with TEM results. Fig. 3.10 displays the distribution results from AFM, TEM,

ITC, and predictions from the dendrimer-encased vesicle and flattened-dendrimer models.

In addition to TEM examination of the dendrimer lipid complexes at the stoichiometric ratio of n_L (Fig. 3.8A), the dendrimer lipid complexes were also examined at the stoichiometric ratio of n_D (Fig. 3.9A). Again, regions of large dendrimer-lipid aggregates and regions of isolated dendrimers are observed. These regions of isolated dendrimers may be the result of individual dendrimer-lipid complexes in solution absorbing onto the TEM grid in a two-dimensional layer and/or they may represent the structure of three-dimensional dendrimer-lipid aggregates where individual dendrimers are separated by lipid bilayers wrapping the dendrimers (Fig. 3.2C). To compare further the TEM images with isolated dendrimers and the dendrimer-encased vesicle model, the measured and predicted areas were compared (Fig. 3.9). A cross-section through the equatorial plane of the dendrimer-encased vesicle complex has a total area of 270 nm^2, where 70 nm^2 would be through the G8 and 200 nm^2 would be through the bilayer wrapping the G8. Analysis of the isolated-dendrimer regions in Fig. 3.9A (i.e. surrounding the outlined aggregates) gives a total area of 88,000 nm^2 and contains 298 dendrimers. Therefore, the area per dendrimer from the TEM is 295 nm^2/G8 whereas the model predicts 270 nm^2/G8. This excellent agreement further supports the dendrimer-encased vesicle model as a common stoichiometry for the dendrimers and lipids.

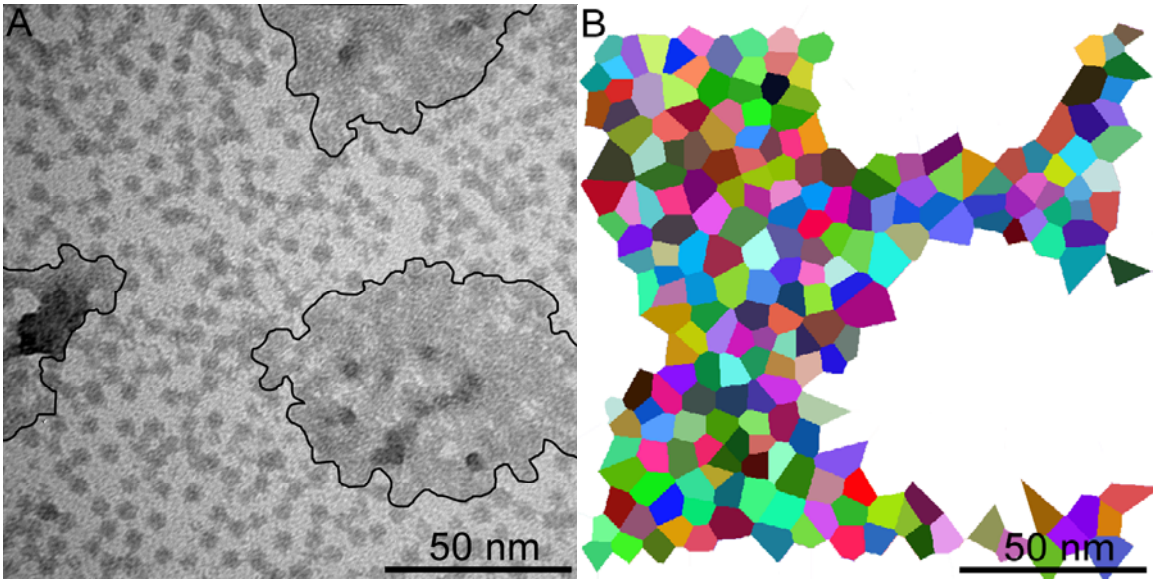

Figure 3.9. (A) TEM image of G8-DMPG complexes with a total molar ratio of n_D = 0.0006 G8/DMPG. A outline is drawn to separate the regions of individually resolvable dendrimers from aggregated dendrimers. (B) A distribution of area per G8 is obtained via a Voronoi diagram of the individual G8 and reveals an area per dendrimer consistent with the dendrimer-encased vesicle model (Fig. 3.10). Dendrimers within (A) that were not both individually resolvable and surrounded by individually resolvable dendrimers were not included in (B).

A distribution of the dendrimer complexes in Fig. 3.9A was obtained through creation of a Voronoi diagram to assess the area of each complex (Fig. 3.9B). Briefly, the Voronoi diagram was created by identifying a set of points on a plane (the center of each isolated G8 in this application) and then mapping regions of the entire plane to each point based on the closest neighboring points. This provided an assessment of the area surrounding each point and, in our case, the cross-sectional area (*A*) of each isolated G8-DMPG complex. Here, *A* is assumed to be a plane through a larger three-dimensional structure. For comparison with other models, the volume (*V*) of the structure was estimated by $V = \frac{4}{3\sqrt{\pi}} A^{3/2}$, as would be expected for a sphere. Again, good agreement

is found between the dendrimer-encased vesicle model and TEM of the the G8-DMPG mixture with mean volumes of 3900 ± 600 nm^3 and 3300 ± 1600 nm^3, respectively.

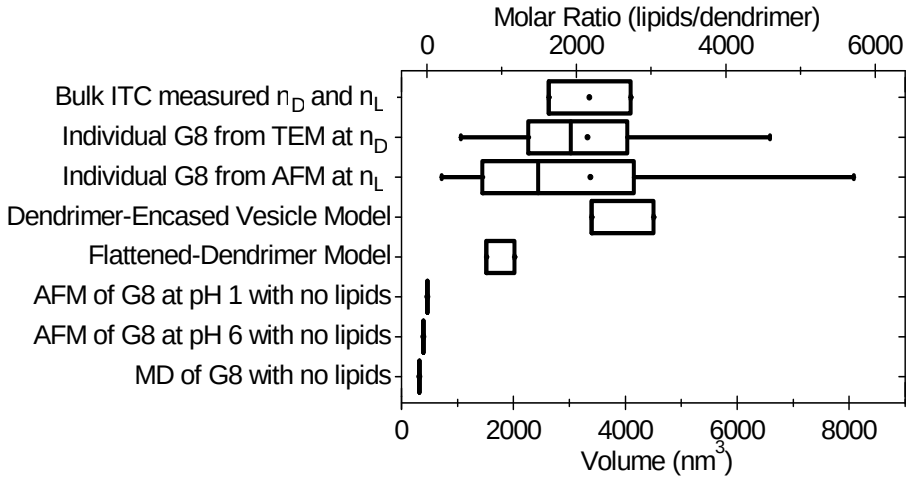

Figure 3.10. Examination of dendrimer-lipid complexes, as measured by AFM, TEM, and ITC, and estimated from models. Results are compared by both volume and stoichiometry by assuming a constant density of lipids (1.5 nm^3/lipid) and one dendrimer per complex. ITC, TEM, and AFM results suggest the average G8-DMPG complex is consistent with the dendrimer-encased vesicle model (Fig. 3.6B). The volume of lipids in the absence of lipids was previously measured.[38, 42]

This data suggests the following mechanism to describe the binding of dendrimers to lipid bilayers (Fig. 3.2C). (1) Dendrimer(s) bind to the membrane due to a combination of forces, such as electrostatics, hydrophobicity, desolvation, etc., (2) Dendrimer(s) and membrane deform to increase interaction area, including dendrimer flattening and membrane curving around the dendrimer(s). (3a) If the dendrimer is large enough and has enough primary amines, then the curvature of the membrane around the dendrimer results in a complete encapsulation of the dendrimer by the bilayer, yielding a dendrimer-encased vesicle complex, perhaps aided by cooperativity from other dendrimers and/or as part of a larger dendrimer-lipid aggregate. (3b) If an individual dendrimer smaller than G7 contacts the bilayer, then it is unable to individually become wrapped in a lipid bilayer or, thus, to produce a pore in the membrane. (3c) If the lipid

concentration is relatively large compared to the dendrimer concentration, then the dendrimers can flocculate the vesicles, presumably by binding to multiple bilayers simultaneously. (3d) If the dendrimer concentration is relatively large relative to the lipid concentration, than multiple dendrimers may aggregate on the surface of a single bilayer and create a pore, analogous to the carpeting mechanism. Since each small dendrimer may be able to maintain a small amount of membrane curvature, if multiple small dendrimers act collectively, it is feasible that they could each stabilize a portion of a vesicle surrounding multiple small dendrimers. This model of collective action by small dendrimers would explain the presence of membrane pores from small dendrimers at higher dendrimer concentrations while being consistent with the ITC stoichiometric data. If such a cooperative mechanism of pore formation occurred, the relationship between saturating stoichiometries and number of primary amines per dendrimer indicates that multiple smaller dendrimers (e.g. two G6 or four G5) would collectively have as many primary amines as one G7 and, thus, be capable of supporting a bilayer wrapping around the aggregated dendrimers.

Further consideration of Fig. 3.1 reveals interesting similarities and differences between the interactions of PAMAM dendrimers and various phospholipids. For example, the observation that $\Delta H^0 = 0$ for G5 and DMPC can be understood as either (1) bilayer disruption was dependent on entropic effects, such as membrane curvature, dendrimer deformation, desolvation, or counter-ion release without a measureable enthalpy contribution or (2) bilayer disruption occurred on a time scale orders of magnitude longer than that of initial binding, and thus, is unobservable with ITC. This result is particularly interesting because experimental and theoretical techniques such as

atomic force microscopy (AFM),[13-16, 33, 34, 36, 43, 44] vesicle leakage,[8, 37] whole-cell leakage,[13-16, 21] computer simulations,[26-30, 32] differential scanning calorimetry,[7, 45-47] electron paramagnetic resonance,[48, 49] and Raman spectroscopy[45] demonstrated that a spontaneous interaction exists between protonated PAMAM dendrimers and fluid phase zwitterionic phospholipids, commonly results in membrane degradation within minutes of mixing. Since the interaction is experimentally observed within a few minutes of dendrimer-lipid mixing, option (2) is eliminated and entropy is determined to be the driving factor for membrane disruption on zwitterionic lipids. A hydrophobic interaction between the inner dendrimer and lipid tails may encourage a dendrimer-membrane interaction, as suggested by computational studies.[27] Additionally, entropic contributions from counter ion release or desolvation from the charged macromolecules may yield an entropic driving force for dendrimer-lipid binding.[50] Interestingly, toxicological and AFM studies indicated that the surface area and net charge of nanoparticles may be the best predictor of zwitterionic membrane disruption.[12, 13]

The ΔH from ITC is not directly comparable to the ΔH from implicit solvent computations. The ITC result of $\Delta H = 0$ for G5-DMPC interactions incorporated desolvation effects, where as previous simulation results of a nonzero ΔH of dendrimer-DMPC interactions[27] considered only the direct dendrimer-lipid interaction without incorporating contributions from desolvation.

The positive enthalpy of interaction for G5 and DMEPC data indicates the dendrimers entropically favored an interaction with the lipids and paid an enthalpic cost to do so. This endothermic interaction may be similar to the aggregation of G5 and anionic lipids; however, possibility a simultaneous exothermic interaction of G5-anionic

lipids did not occur for G5-cationic lipids. This data is supportive of the hypothesis that the interaction between dendrimers and lipids is enhanced by hydrophobic interactions while their relative charge affects the enthalpic contribution to their interaction.

3.3. CONCLUSIONS

ITC, DLS, AFM, TEM, and MD were performed with assorted PAMAM dendrimers and phospholipids. The interaction enthalpy depended largely on the relative electrostatic charge of the dendrimer and the phospholipids. The ΔH^0 and saturating stoichiometry of the dendrimer-DMPG interactions were linearly dependent on the number of primary amines per dendrimer, regardless of dendrimer generation or termination, for dendrimers of sixth-generation and smaller. The lack of heat released upon dendrimer-DMPC interaction suggests the binding and eventual pore formation[16] are driven by changes in entropy rather than enthalpy for these zwitterionic lipids. Models of the dendrimers bound to the lipids were analyzed by considering (1) the number of lipids per dendrimer, (2) the density of lipids molecules within the bilayer, and (3) the deformability of the dendrimer. For increasing dendrimer generation, the requirement of membrane curvature around the bilayer became a necessary component in the resulting dendrimer-lipid complex to achieve sufficient lipids in close proximity to each dendrimer. As isolated or aggregated complexes, dendrimers larger than G6 become encased in a bilayer of lipids, on average, while smaller dendrimers do not.

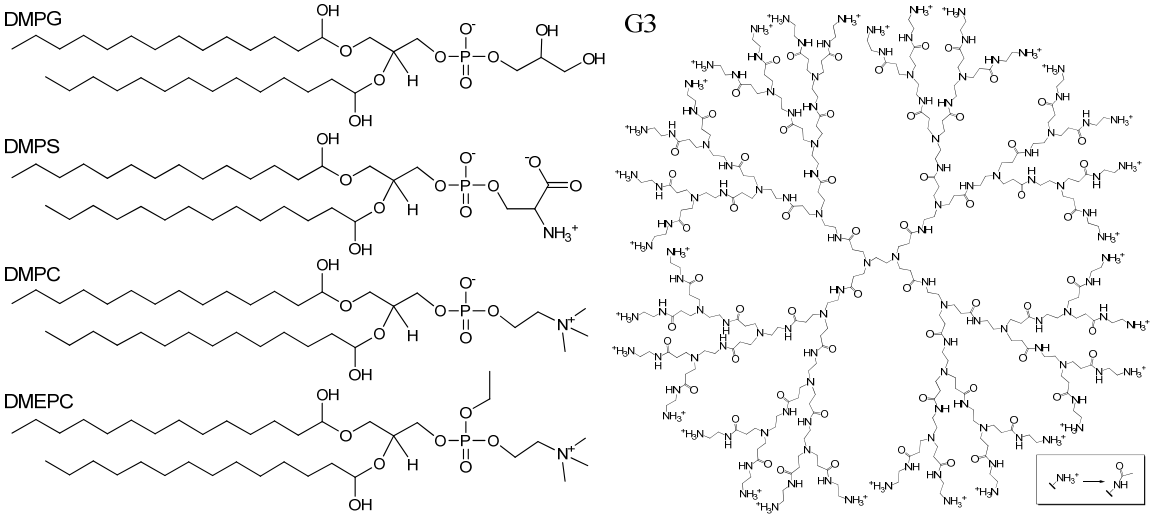

Figure 3.11. Molecular structure of the phospholipids and PAMAM dendrimers used in this study. The PAMAM dendrimer contains protonated primary amines at pH 7.4. However, to reduce the total charge on the dendrimer, the terminal amines may be acetylated, as shown in the inset.

Table 3.2. Charge and mass of phospholipids and PAMAM dendrimers.

Lipid	**Net Charge (*e*)**	**T_m (°C)**
DMPG	-1	23
DMPS	-1	35
DMPC	0	23
DMEPC	+1	24
PAMAM Dendrimer	**Mass (kD)[a]**	**Charge (*e*)[b]**
G5-Ac(100%)	32	0
G3	6.9	31
G5-Ac(40%)	29	70
G5	27	112
G6	46	187
G7	106	450
G8	260	1090
G9	428	1880

3.4. METHODS

Purified, biomedical-grade PAMAM dendrimers were obtained from Dendritech, Inc. of generation (G) 3, 5, 6, 7, 8, and 9 with native primary amine termination (Fig. 3.12 and Table 3.2). All primary amine PAMAM dendrimers dialyzed with a molecular weight cutoff membrane against distilled water for at least three days with at least four washes. Potentiometric titration was conducted to determine the average number of primary amines. Molecular weight and dispersity were characterized with gel permeation chromatography. Acetylation was performed as published previously and shown in Fig. 3.12.[51] Samples were lyophilized for three days resulting in a white solid. The primary amines are expected to be protonated at pH 7.4 and the tertiary amines are not; therefore, the charge of each dendrimer is equal to its number of primary amines. The mass and charge of each dendrimer are listed in Table 3.2.

Dried powders of 1,2-Dimyristoyl-sn-Glycero-3-(Phospho-L-Serine); 1,2-Dimyristoyl-sn-Glycero-3-(Phospho-rac-(1-glycerol)); 1,2-Dimyristoyl-sn-Glycero-3-Phosphocholine; and 1,2-Dimyristoyl-sn-Glycero-3-Ethylphosphocholine (DMPS, DMPG, DMPC, and DMEPC, respectively) were obtained from Avanti Polar Lipids, Inc. and prepared as small unilaminar vesicles (SUVs). Briefly, weighed lipid powders were mixed with chloroform, sonicated for > 5 min, and dried under vacuum for > 8 hours. The resulting film of lipids was mixed with buffer and alternately shaken vigorously for > 15 sec and incubated at 37°C for > 1 hr for at least two repetitions to produce multilaminar vesicles (MLVs). Small unilaminar vesicles (SUVs) were produced through sonication of MLVs, as previously reported.[15] No lipids were kept at room

temperature for greater than 4 days. The charge and transition temperatures of these phospholipids are listed in Table 3.2.

Dendrimer and phospholipid solutions were prepared in 1x Dulbecco's phosphate buffered saline without Calcium, Magnesium, or Phenol Red (PBS, Thermo Scientific, Inc., pH 7.4, 138 mM NaCl).

ITC was performed with a VP-ITC (MicroCal, Inc.) with dendrimers in the injection syringe and lipids in the experimental cell (usually 80 μM) while the references cell contained PBS. Stirring of the experimental cell occurred at 372 rpm throughout the titration. Sample degassing, instrument maintenance, and cleaning was performed according to manufacturers recommendations. Baseline fitting to raw ITC data was performed following automated routines within Origin 7.0 data acquisition and analysis software (OriginLab Corp.), with minor corrections at user's discretion (Fig. 3.13). Resulting peak integrations of power vs. time from the raw ITC data are plotted as energy per mole of injectant (ΔH) at the molar ratio of dendrimers per lipid (n) in the sample cell after each injection. ITC experiments were performed at 50°C, well above the phase transition for all lipids used, resulting in fluid-disordered phase bilayers.[52] The last injections of each titration yielded ΔH equal to control experiments without lipids present and these values were set equal to zero for analysis of the dendrimer-lipid interaction.

Analysis of the ITC data did not include mathematical fitting to traditional binding models due to the variety of possible models that fit the data for cationic dendrimers interacting with anionic lipids. If the processes that resulted in the observed ITC line shape were occurring simultaneously and independently, then these two processes may have both contributed to the observed net ΔH of interaction via an

endothermic interaction at very low stoichiometries (n < 0.0001 dendrimer/lipid, e.g. flocculation), followed by an exothermic interaction at higher stoichiometries (0.0005 < n < 0.01 dendrimer/lipid, e.g. supramolecular complex formation) (Fig. 3.2). However, if these two processes are competitive or cooperative, then the entirety of the measured ΔH may be attributed to just one of the processes while the other processes were not enthalpically dependent.

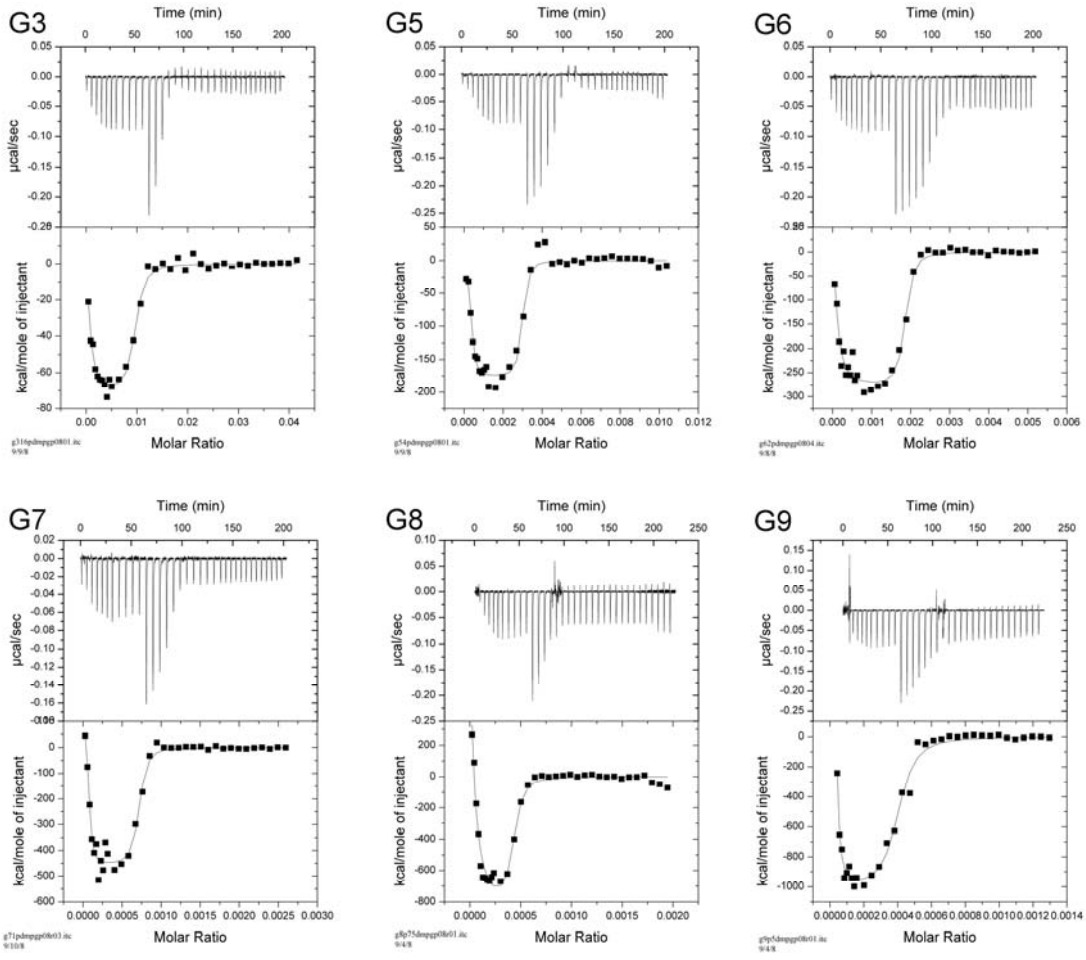

Figure 3.12. Raw data of power vs. time and ΔH vs. molar ratio for PAMAM dendrimers titrated into DMPG SUVs at 50 °C in PBS.

Transmission electron microscopy (TEM) was performed on a Philips CM-100. Sample preparation included the following: Mixtures of DMPG and G8 in PBS were placed on a 200-grain carbon-coated copper TEM grid for 5 min and excess lipid was removed by blotting. The initial lipid concentration was 80 μM and dendrimer concentration varied to achieve the desired molar ratio. The grid was rinsed with distilled H_20 and blotted dry to remove excess salt. 1% solution of urinal acetate in distilled H_20 was placed on the grid for 10 min and blotted dry. The remaining urinal acetate was a counter stain on the samples, making the dendrimers dark in the resulting TEM images. Staining and imaging constraints prohibited the viewing of lipids in the presence of dendrimers.

Molecular dynamics (MD) simulations were performed as described elsewhere.[27] Briefly, MD simulations utilized the CHARMM parameters for generic proteins (para22) for the dendrimer and CHARMM27 parameters for the lipids.[53, 54] Simulations were run at 300 K. Non-bonded interactions were cutoff at 13 Å and switched from 8 Å. Time steps of 2 fs were taken with implementation of the SHAKE routine. Initial dendrimer configurations were made with a recursive script in CHARMM.[55] Both the dendrimer and the lipids were separately equilibrated for 2 ns before being were combined. The simulation was run until dendrimer stopped moving along the direction perpendicular to the lipid bilayer for more than 5 ns. A distance-dependent dielectric function was employed as an implicit solvent model. This yielded significant (>10 fold) enhancement in required computational time but incorporated greater approximations through eliminating the entropic contribution from the solvent or counter ions.[26] Images from MD results within this chapter were created with the software VMD.[56]

The TEM samples were also measured with AFM. Samples were imaged using a PicoPlus 550 equipped with a multipurpose small scanner, capable of imaging up to 10 μm x 10 μm (Agilent (formerly Molecular Imaging); Santa Clara, CA). Scans were performed in tapping mode using silicon cantilevers (VistaProbes T300R, force constant 40 N/m, resonance frequency 300 kHz, length 125 μm; nanoScience Instruments; Phoenix, AZ). Scan rates were ≤ 2 Hz at 1024 lines per frame. All imaging was done in air at room temperature, nominally 25°C. Image flattening, line scans, and volume analysis were performed with Gwyddion (Czech Metrology Institute).

Dynamic light scattering (DLS) was performed on a Nanosizer ZS (Malvern Instruments Ltd.). Samples were prepared in a semi-micro cuvette to a volume of 0.5 mL and varying molar ratios. Samples were in PBS, stirred and 50 °C for > 5 min before measurement, and 50 °C during measurement, to replicate ITC conditions. All samples of dendrimers and lipids were observed to aggregate as the dendrimer/lipid molar ratio increased until the DLS was unable to determine accurately the average particle size due to the aggregates. The molar ratios at which DLS was unable to determine the average particle size were approximately n_L.

3.5. ACKNOWLEDGMENTS

The authors thank Lisa Prevette and Istvan Majoros from Michigan Nanotechnology Institute for Medicine and Biological Sciences (MNiMBS) for insightful discussions. C.V.K. received fellowship support from the NIH Michigan Molecular Biophysics Training Program (T32 GM008270-20), the Applied Physics program, and the Graham Environmental Sustainability Institute. This research was supported by a

grant from the National Institute of Biomedical Imaging and BioEngineering (R01-EB005028).

3.6. REFERENCES

1. Esfand, R.; Tomalia, D. A., Poly(amidoamine) (PAMAM) dendrimers: from biomimicry to drug delivery and biomedical applications. *Drug Discovery Today* **2001,** 6, (8), 427-436.
2. Langer, R., Drug delivery and targeting. *Nature* **1998,** 392, (6679), 5-10.
3. Quintana, A.; Raczka, E.; Piehler, L.; Lee, I.; Myc, A.; Majoros, I.; Patri, A. K.; Thomas, T.; Mule, J.; Baker, J. R., Design and function of a dendrimer-based therapeutic nanodevice targeted to tumor cells through the folate receptor. *Pharmaceutical research* **2002,** 19, (9), 1310-1316.
4. Kukowska-Latallo, J. F.; Candido, K. A.; Cao, Z. Y.; Nigavekar, S. S.; Majoros, I. J.; Thomas, T. P.; Balogh, L. P.; Khan, M. K.; Baker, J. R., Nanoparticle targeting of anticancer drug improves therapeutic response in animal model of human epithelial cancer. *Cancer Research* **2005,** 65, (12), 5317-5324.
5. Shiota, M.; Ikeda, Y.; Kaul, Z.; Itadani, J.; Kaul, S. C.; Wadhwa, R., Internalizing antibody-based targeted gene delivery for human cancer cells. *Human Gene Therapy* **2007,** 18, (11), 1153-1160.
6. Parveen, S.; Sahoo, S. K., Polymeric nanoparticles for cancer therapy. *Journal of Drug Targeting* **2008,** 16, (2), 108-123.
7. Braun, C. S.; Vetro, J. A.; Tomalia, D. A.; Koe, G. S.; Koe, J. G.; Middaugh, C. R., Structure/function relationships of polyamidoamine/DNA dendrimers as gene delivery vehicles. *Journal of Pharmaceutical Sciences* **2005,** 94, (2), 423-436.
8. Zhang, Z. Y.; Smith, B. D., High-generation polycationic dendrimers are unusually effective at disrupting anionic vesicles: Membrane bending model. *Bioconjugate Chemistry* **2000,** 11, (6), 805-814.
9. Zhang, S. B.; Zhao, B.; Jiang, H. M.; Wang, B.; Ma, B. C., Cationic lipids and polymers mediated vectors for delivery of siRNA. *Journal of Controlled Release* **2007,** 123, (1), 1-10.
10. Fischer, D.; Li, Y. X.; Ahlemeyer, B.; Krieglstein, J.; Kissel, T., In vitro cytotoxicity testing of polycations: influence of polymer structure on cell viability and hemolysis. *Biomaterials* **2003,** 24, (7), 1121-1131.
11. Maynard, A. D.; Aitken, R. J.; Butz, T.; Colvin, V.; Donaldson, K.; Oberdorster, G.; Philbert, M. A.; Ryan, J.; Seaton, A.; Stone, V.; Tinkle, S. S.; Tran, L.; Walker, N. J.; Warheit, D. B., Safe handling of nanotechnology. *Nature* **2006,** 444, (7117), 267-269.
12. Oberdorster, G.; Oberdorster, E.; Oberdorster, J., Nanotoxicology: An emerging discipline evolving from studies of ultrafine particles. *Environmental Health Perspectives* **2005,** 113, (7), 823-839.
13. Leroueil, P. R.; Berry, S. A.; Duthie, K.; Han, G.; Rotello, V. M.; McNerny, D. Q.; Baker, J. R.; Orr, B. G.; Holl, M. M. B., Wide varieties of cationic nanoparticles induce defects in supported lipid bilayers. *Nano Letters* **2008,** 8, (2), 420-424.
14. Leroueil, P. R.; Hong, S. Y.; Mecke, A.; Baker, J. R.; Orr, B. G.; Holl, M. M. B., Nanoparticle interaction with biological membranes: Does nanotechnology present a janus face? *Accounts of Chemical Research* **2007,** 40, (5), 335-342.
15. Hong, S. P.; Leroueil, P. R.; Janus, E. K.; Peters, J. L.; Kober, M. M.; Islam, M. T.; Orr, B. G.; Baker, J. R.; Holl, M. M. B., Interaction of polycationic polymers with supported lipid bilayers and cells: Nanoscale hole formation and enhanced membrane permeability. *Bioconjugate Chemistry* **2006,** 17, (3), 728-734.
16. Hong, S. P.; Bielinska, A. U.; Mecke, A.; Keszler, B.; Beals, J. L.; Shi, X. Y.; Balogh, L.; Orr, B. G.; Baker, J. R.; Holl, M. M. B., Interaction of poly(amidoamine) dendrimers with supported

lipid bilayers and cells: Hole formation and the relation to transport. *Bioconjugate Chemistry* **2004,** 15, (4), 774-782.
17. Monteiro-Riviere, N. A.; Nemanich, R. J.; Inman, A. O.; Wang, Y. Y. Y.; Riviere, J. E., Multi-walled carbon nanotube interactions with human epidermal keratinocytes. *Toxicology Letters* **2005,** 155, (3), 377-384.
18. Oberdorster, E., Manufactured nanomaterials (Fullerenes, C-60) induce oxidative stress in the brain of juvenile largemouth bass. *Environmental Health Perspectives* **2004,** 112, (10), 1058-1062.
19. Tinkle, S. S.; Antonini, J. M.; Rich, B. A.; Roberts, J. R.; Salmen, R.; DePree, K.; Adkins, E. J., Skin as a route of exposure and sensitization in chronic beryllium disease. *Environmental Health Perspectives* **2003,** 111, (9), 1202-1208.
20. Oberdorster, G.; Gelein, R. M.; Ferin, J.; Weiss, B., Association of Particulate Air-Pollution and Acute Mortality - Involvement of Ultrafine Particles. *Inhalation Toxicology* **1995,** 7, (1), 111-124.
21. El-Sayed, M.; Ginski, M.; Rhodes, C.; Ghandehari, H., Transepithelial transport of poly(amidoamine) dendrimers across Caco-2 cell monolayers. *Journal of Controlled Release* **2002,** 81, (3), 355-365.
22. Wang, C.; Wyn-Jones, E.; Sidhu, J.; Tam, K. C., Supramolecular complex induced by the binding of sodium dodecyl sulfate to PAMAM dendrimers. *Langmuir* **2007,** 23, (4), 1635-1639.
23. Sidhu, J.; Bloor, D. M.; Couderc-Azouani, S.; Penfold, J.; Holzwarth, J. F.; Wyn-Jones, E., Interactions of poly(amidoamine) dendrimers with the surfactants SDS, DTAB, and C12EO6: An equilibrium and structural study using-a SDS selective electrode, isothermal titration calorimetry, and small angle neutron scattering. *Langmuir* **2004,** 20, (21), 9320-9328.
24. Wang, B.; Zhang, L.; Bae, S. C.; Granick, S., Nanoparticle-induced surface reconstruction of phospholipid membranes. *Proceedings of the National Academy of Sciences of the United States of America* **2008,** 105, (47), 18171–18175.
25. Zhang, L. F.; Granick, S., How to stabilize phospholipid liposomes (using nanoparticles). *Nano Letters* **2006,** 6, (4), 694-698.
26. Kelly, C. V.; Leroueil, P. R.; Nett, E. J.; Wereszczynski, J. M.; Baker, J. R.; Orr, B. G.; Holl, M. M. B.; Andricioaei, I., Poly(amidoamine) dendrimers on lipid bilayers I: Free energy and conformation of binding. *Journal of Physical Chemistry B* **2008,** 112, (31), 9337-9345
27. Kelly, C. V.; Leroueil, P. R.; Orr, B. G.; Holl, M. M. B.; Andricioaei, I., Poly(amidoamine) dendrimers on lipid bilayers II: Effects of bilayer phase and dendrimer termination. *Journal of Physical Chemistry B* **2008,** 112, (31), 9346-9353.
28. Lee, H.; Larson, R. G., Coarse-grained molecular dynamics studies of the concentration and size dependence of fifth- and seventh-generation PAMAM dendrimers on pore formation in DMPC bilayer. *Journal of Physical Chemistry B* **2008,** 112, (26), 7778-7784.
29. Lee, H.; Larson, R. G., Lipid bilayer curvature and pore formation induced by charged linear polymers and dendrimers: The effect of molecular shape. *Journal of Physical Chemistry B* **2008,** 112, (39), 12279-12285.
30. Lee, H.; Larson, R. G., Molecular dynamics simulations of PAMAM dendrimer-induced pore formation in DPPC bilayers with a coarse-grained model. *Journal of Physical Chemistry B* **2006,** 110, (37), 18204-18211.
31. Smith, K. A.; Jasnow, D.; Balazs, A. C., Designing synthetic vesicles that engulf nanoscopic particles. *Journal of Chemical Physics* **2007,** 127, (8).
32. Ginzburg, V. V.; Balijepailli, S., Modeling the thermodynamics of the interaction of nanoparticles with cell membranes. *Nano Letters* **2007,** 7, (12), 3716-3722.

33. Mecke, A.; Uppuluri, S.; Sassanella, T. M.; Lee, D. K.; Ramamoorthy, A.; Baker, J. R.; Orr, B. G.; Holl, M. M. B., Direct observation of lipid bilayer disruption by poly(amidoamine) dendrimers. *Chemistry and Physics of Lipids* **2004,** 132, (1), 3-14.
34. Mecke, A.; Majoros, I. J.; Patri, A. K.; Baker, J. R.; Holl, M. M. B.; Orr, B. G., Lipid bilayer disruption by polycationic polymers: The roles of size and chemical functional group. *Langmuir* **2005,** 21, (23), 10348-10354.
35. Oren, Z.; Shai, Y., Mode of action of linear amphipathic alpha-helical antimicrobial peptides. *Biopolymers* **1998,** 47, (6), 451-463.
36. Erickson, B.; Kelly, C. V.; Leroueil, P. R.; Berry, S. A.; James R. Baker, J.; Orr, B. G.; Holl, M. M. B., Interactions of Poly(amidoamine) Dendrimers with Survanta Lung Surfactant: The Importance of Lipid Domains. *Langmuir* **2008,** 24, (19), 11003-11008.
37. Karoonuthaisiri, N.; Titiyevskiy, K.; Thomas, J. L., Destabilization of fatty acid-containing liposomes by. polyamidoamine dendrimers. *Colloids and Surfaces B-Biointerfaces* **2003,** 27, (4), 365-375.
38. Betley, T. A.; Holl, M. M. B.; Orr, B. G.; Swanson, D. R.; Tomalia, D. A.; Baker, J. R., Tapping mode atomic force microscopy investigation of poly(amidoamine) dendrimers: Effects of substrate and pH on dendrimer deformation. *Langmuir* **2001,** 17, (9), 2768-2773.
39. Garidel, P.; Blume, A., 1,2-Dimyristoyl-sn-glycero-3-phosphoglycerol (DMPG) monolayers: influence of temperature, pH, ionic strength and binding of alkaline earth cations. *Chemistry and Physics of Lipids* **2005,** 138, (1-2), 50-59.
40. Mecke, A.; Lee, I.; Baker, J. R.; Holl, M. M. B.; Orr, B. G., Deformability of poly(amidoamine) dendrimers. *European Physical Journal E* **2004,** 14, (1), 7-16.
41. Wohlert, J.; den Otter, W. K.; Edholm, O.; Briels, W. J., Free energy of a trans-membrane pore calculated from atomistic molecular dynamics simulations. *Journal of Chemical Physics* **2006,** 124, (15), 9.
42. Maiti, P. K.; Cagin, T.; Wang, G. F.; Goddard, W. A., Structure of PAMAM dendrimers: Generations 1 through 11. *Macromolecules* **2004,** 37, (16), 6236-6254.
43. Mecke, A.; Lee, D. K.; Ramamoorthy, A.; Orr, B. G.; Holl, M. M. B., Synthetic and natural polycationic polymer nanoparticles interact selectively with fluid-phase domains of DMPC lipid bilayers. *Langmuir* **2005,** 21, (19), 8588-8590.
44. Parimi, S.; Barnes, T. J.; Prestidge, C. A., PAMAM Dendrimer Interactions with Supported Lipid Bilayers: A Kinetic and Mechanistic Investigation. *Langmuir* **2008,** 24, (23), 13532-13539.
45. Gardikis, K.; Hatziantoniou, S.; Viras, K.; Wagner, M.; Demetzos, C., A DSC and Raman spectroscopy study on the effect of PAMAM dendrimer on DPPC model lipid membranes. *International Journal of Pharmaceutics* **2006,** 318, (1-2), 118-123.
46. Klajnert, B.; Epand, R. M., PAMAM dendrimers and model membranes: Differential scanning calorimetry studies. *International Journal of Pharmaceutics* **2005,** 305, (1-2), 154-166.
47. Klajnert, B.; Stanislawska, L.; Bryszewska, M.; Palecz, B., Interactions between PAMAM dendrimers and bovine serum albumin. *Biochimica Et Biophysica Acta-Proteins and Proteomics* **2003,** 1648, (1-2), 115-126.
48. Ottaviani, M. F.; Daddi, R.; Brustolon, M.; Turro, N. J.; Tomalia, D. A., Structural Modifications of DMPS Vesicles upon Interaction with Poly(amidoamine) Dendrimers Studied by CW-Electron Paramagnetic Resonance and Electron Spin-Echo Techniques. *Langmuir* **1999,** 15, 1973-1980.
49. Ottaviani, M. F.; Matteini, P.; Brustolon, M.; Turro, N. J.; Jockusch, S.; Tomalia, D. A., Characterization of starburst dendrimers and vesicle solutions and their interactions by CW- and pulsed-EPR, TEM, and dynamic light scattering. *Journal of Physical Chemistry B* **1998,** 102, (31), 6029-6039.

50. Record, M. T.; Lohman, T. M.; Dehaseth, P., Ion Effects on Ligand-Nucleic Acid Interactions. *Journal of Molecular Biology* **1976,** 107, (2), 145-158.
51. Majoros, I. J.; Myc, A.; Thomas, T.; Mehta, C. B.; Baker, J. R., PAMAM dendrimer-based multifunctional conjugate for cancer therapy: Synthesis, characterization, and functionality. *Biomacromolecules* **2006,** 7, (2), 572-579.
52. Ipsen, J. H.; Karlstrom, G.; Mouritsen, O. G.; Wennerstrom, H.; Zuckermann, M. J., Phase-Equilibria in the Phosphatidylcholine-Cholesterol System. *Biochimica Et Biophysica Acta* **1987,** 905, (1), 162-172.
53. Brooks, B. R.; Bruccoleri, R. E.; Olafson, B. D.; States, D. J.; Swaminathan, S.; Karplus, M., Charmm - a Program for Macromolecular Energy, Minimization, and Dynamics Calculations. *Journal of Computational Chemistry* **1983,** 4, (2), 187-217.
54. MacKerell, A. D.; Bashford, D.; Bellott, M.; Dunbrack, R. L.; Evanseck, J. D.; Field, M. J.; Fischer, S.; Gao, J.; Guo, H.; Ha, S.; Joseph-; McCarthy, D.; Kuchnir, L.; Kuczera, K.; Lau, F. T. K.; Mattos, C.; Michnick, S.; Ngo, T.; Nguyen, D. T.; Prodhom, B.; Reiher, W. E.; Roux, B.; Schlenkrich, M.; Smith, J. C.; Stote, R.; Straub, J.; Watanabe, M.; Wiorkiewicz-Kuczera, J.; Yin, D.; Karplus, M., ll-atom empirical potential for molecular modeling and dynamics studies of proteins. *J. Phys. Chem. B* **1998,** 102 (18), 3586-3616.
55. Mercier, G. A., Dendrimer Builder. *http://server.ccl.net/chemistry/resources/messages/1996/05/20.009-dir/index.html* **1996**.
56. Humphrey, W.; Dalke, A.; Schulten, K., VMD: Visual molecular dynamics. *Journal of Molecular Graphics* **1996,** 14, (1), 33-&.

CHAPTER 4

POLY(AMIDOAMINE) DENDRIMERS ON LIPID BILAYERS I: FREE ENERGY AND CONFORMATION OF BINDING

4.1. INTRODUCTION

Functionalized nanoparticles are a novel focus of modern medicine. Nanoparticles are chemically modified for precisely defined properties in attempts to create agents for gene therapy and targeted drug delivery. As nanodevices approach a living animal cell, the first interaction is with the cellular plasma membrane. Nanometer-sized particles are especially effective at penetrating the plasma membrane and altering the natural processes within the cell.[1-8] Nanoparticles can be effective carriers of therapeutic cargos through the plasma membrane, likely due to one of two internalization mechanisms: physical rupturing and pore formation[1-3] or receptor-mediated, energy dependent cellular processes, such as endocytosis.[6-8]

Synthetic polymer nanodevices have been developed from polylysine, polyethylenimine, and assorted dendrimers.[9] PAMAM dendrimers are a widely studied synthetic polymer for both medical and basic science applications.[10-12] Their structure incorporates the starburst addition of repeating units around the ethylenediamine core to the desired generation (G) (Fig. 4.1). Dendrimers are particularly useful due to their high homogeneity (polydispersity index ≈ 1.01)[2] and use as a framework in multifunctional nanodevices. PAMAM dendrimers are natively terminated with primary amines and are

commonly modified by the covalent addition of small functional molecules (e.g. chromophores, chemotherapeutics, targeting moieties) and less reactive terminations (e.g. acetamide or hydroxyl) to create a nanodevice capable of targeting, binding, internalizing, labeling, and/or treating diseased cells.[10, 13-15]

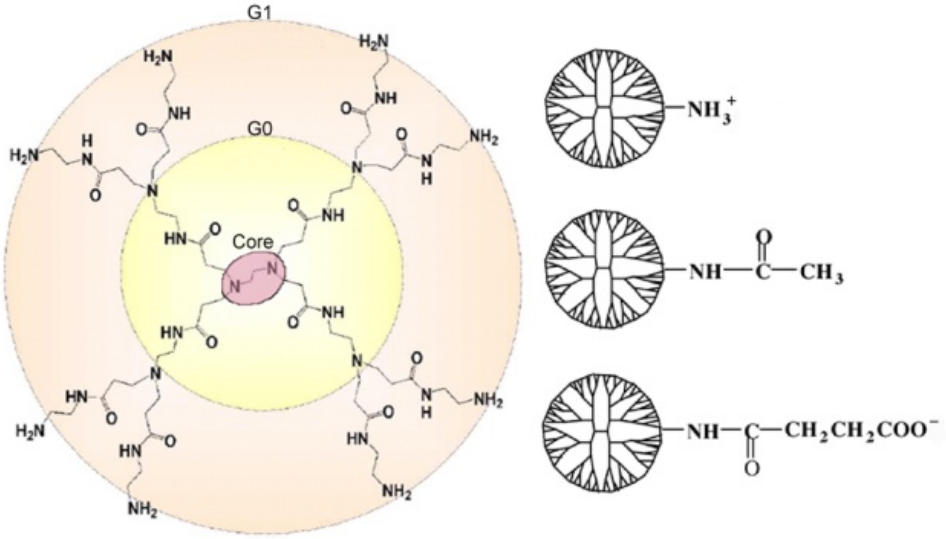

Figure 4.1. The composition of a natively-terminated first generation (G1) PAMAM dendrimer and three possible terminations: protonated primary amine (-NH3+), neutral acetamide (-Ac), and deprotonated carboxylic acid (-COO-). A summary of dendrimer properties is given in Table 4.1.

For example, acetylization of the PAMAM dendrimer's primary amine end groups can reduce non-specific binding, enhance functional capabilities, and minimize nanoparticle toxicity.[10, 14-16] Positively charged nanoparticles are more likely to bind and internalize into cells than are the uncharged analogues.[2, 3] This strong relationship between nanoparticle termination and biological behavior demonstrates the importance of understanding the mechanisms of nanoparticle-membrane interactions for effective nanodevice design.

Table 4.1. Properties of the G3 PAMAM dendrimers.

PAMAM Dendrimer	Terminal group[A]	Number of atoms per dendrimer	Mass (kD)	Charge (*e*)
G3-NH_3^+	-NH_3^+	1124	6.94	+32
G3-Ac	-$NHCOCH_3$	1252	8.25	0
G3-COO^-	-$NHCOCH_2CH_2COO^-$	1412	10.1	-32

[A]All 32 primary amines of each G3 PAMAM dendrimer are converted to this terminal chemistry.

Atomic force microscopy (AFM) has been used to experimentally study the effects of PAMAM dendrimers on DMPC lipid bilayers with nanometer scale resolution.[17-19] Drastic differences in the dendrimer-lipid interaction were observed for varying dendrimer termination. Charged G5 dendrimers at 20 nM caused membrane disruption via removal of membrane material via the formation of membrane holes and the expansion of preexisting defects. In contrast, neutral G5 dendrimers at 20 nM did not cause as much membrane degradation, but predominantly accumulated around the edge of preexisting holes without removing lipid molecules.

Ginzburg and Balijepalli[20] have utilized continuum thermodynamic models to demonstrate the effects nanoparticle surface charge density has on membrane binding. This model provides a phase diagram of nanoparticle-membrane structures, including regimes of nanoparticle binding within the bilayer's hydrophobic tails and enclosed within vesicles. Lee et al.[21] have looked at dendrimer-phospholipid binding in greater detail through coarse grained simulations, providing qualitatively similar conclusions of nanoparticle charge and size dependence on membrane disruption.

The research reported in this paper presents a quantitative analysis of molecular dynamic simulations of the dendrimer-membrane binding process. To date, only a qualitative picture existed concerning the pore formation process by nanoparticles on

lipid bilayers.[20, 21] Specifically, we examine the differences in energetics and forces of interaction between charged PAMAM dendrimers with zwitterionic DMPC bilayers. Three types of G3 PAMAM dendrimers were examined: positively-charged primary amine (G3-NH_3^+), uncharged acetamide (G3-Ac), and negatively-charged carboxyl (G3-COO^-). The CHARMM27 force field is used for atomistic Langevin dynamics simulations along an interaction coordinate defined as the center of mass separation distance between the dendrimer and lipid bilayer. A distance-dependent dielectric function was used. A potential of mean force is calculated along the interaction coordinate, from which the forces of interaction are extracted. Further, the dendrimers' structure (radii of gyration, asphericities, and atomic distributions) and binding morphology are examined as a function of their proximity to the lipid membrane.

4.2. METHODS

Umbrella sampling[22] and the weighted histogram analysis method (WHAM)[23] were employed to extract the free energy of binding along the interaction coordinate defined as the dendrimer and lipid bilayer center of mass separation distance. The potential of mean force (PMF)[24], or free energy, along the interaction coordinate (z) is extracted from the coordinate's distribution function, averaged over all degrees of freedom as represented in the configurational vector ($\boldsymbol{X}$),

$$PMF(z_0) = -k_B T \log \int e^{-\frac{V(\mathbf{X})}{k_B T}} \delta(z_0 - z(\mathbf{X})) d\mathbf{X}, \quad (1)$$

with Boltzmann constant (k_B), the temperature (T), and the CHARMM[25] potential (V) with the protein parameter set 22.[26]

The PMF along particular (slow) coordinates is a central concept in the statistical mechanical representation of molecular systems and has been widely used in computational applications[27-30] The PMF reveals the equilibrium conformation (i.e. PMF minimum) and free energy changes. The negative gradient of the PMF is exactly the force averaged over the conformational ensemble.[24] In the umbrella sampling calculation performed here long-time events along the interaction coordinate are encouraged to happen within the ns time scale by step-wise moving of the umbrella sampling window offset along the interaction coordinate.

The interaction coordinate (z), defined as the dendrimer-lipid center of mass separation distance, was examined from values of 2.8 to 6.9 nm. Sampling dynamics occurred in equally spaced widows along the interaction coordinate with 0.05 nm step size and a harmonic confinement of the interaction coordinate to the window center by 500 kcal mol^{-1} nm^{-2}. To start the simulations, the dendrimer and lipid bilayer were equilibrated with a harmonic confinement to z=6 nm for 500 ps. The result of this equilibration was used as the initial conditions for the production dynamics in the z=6 nm window as well as the starting configuration for the equilibration at z=5.95 nm, which lasted another 100 ps. The result of the equilibration at 5.95 nm was used to begin the z=5.9 nm window equilibration and so forth until all windows from 6 to 2.8 nm were recursively equilibrated. Once each window was equilibrated, production runs were calculated in parallel for 4 ns per window with atomic configurations saved every 2 ps. To confirm that z>6 nm was outside the interaction range of the dendrimer with the lipid bilayers, further sampling windows were run for 6.05 nm$\leq z \leq$6.9 nm with identical

recursive equilibration procedures starting from the z=6 nm configuration and recursively stepping to larger z.

The interaction coordinate versus time was recorded during all production runs and later used with WHAM to calculate the PMF.[23, 24] The recursive calculation of the PMF via WHAM was performed until a fitting threshold of 0.001 kcal/mol was achieved.[27] WHAM results for the PMF were demonstrated to be dependent on the threshold such that more stringent thresholds resulted in a difference smaller than that between the PMF at z=6 nm and z=6.9 nm. Since the PMF at this extended range is flat and a sufficiently low threshold value was too costly to compute, a linear fit to the PMF was calculated for z=6.0 to 6.9 nm and subtracted for the entirety of the PMF.

The initial structure for the DMPC bilayer originated from a pre-equilibrated patch of 32 lipid molecules replicated 16 times to create a single patch with 512 lipid molecules, from which a 10 nm diameter circular disk was extracted. Lipid equilibration occurred at every step during the creation of the final 10 nm patch for greater than 200 ps each. The equilibrated DMPC disk consisted of 263 phospholipid molecules at a lipid density (60 $Å^2$/lipid) and bilayer thickness (4.3 nm) in agreement with experimental measurements of DMPC bilayers.[31, 32]

The focus of this paper is the examination of binding of dendrimers to a membrane with biological relevance. The primary contribution to the initial binding of dendrimers to membranes was thought to be the interaction between the charged dendrimer moieties with the polar lipid head groups.[33-35] Subsequently, the hydrophobic dendrimer moieties and lipid tails are likely playing an important factor in the later pore formation and penetration of the dendrimer into the bilayer. This manuscript focuses on

the initial binding of dendrimers to the lipid bilayer surface. As such, in the interest of computational efficiency, the lipid tail atoms have been fixed in location. This approximation limits the lateral and vertical motion of the individual lipid molecules; however it does not considerably alter the motion of the lipid head groups. This lipid tail fixation is not expected to significantly affect the binding for large dendrimer-lipid separations ($z \geq 4$ nm) but does affect the binding at smaller separations. The effects of this approximation, and the influence of lipid tail mobility in general, is the subject of a companion article.[36]

Three different PAMAM dendrimers of varying surface chemistry are simulated with DMPC bilayers using the CHARMM27 parameters for lipids[37] and, for dendrimers, parameters from set 22, within the CHARMM c32b2 academic software package.[37, 38] The G3 dendrimers natively contain 32 terminal groups, a net zero charge, and 1092 atoms before modifying the terminal chemistry. The terminations are modified to yield the G3-NH_3^+, G3-Ac and G3-COO^- dendrimers (Fig. 4.1), to make the dendrimers representative of a physiological pH 7 environment.[39] Dendrimer properties are given in Table 4.1 with each protonated primary amine terminal group having a +e charge and each deprotonated carboxylic acid terminal group having a -e charge. This yields three different dendrimers terminations giving the dendrimers a net charge of +32e, 0, or -32e. The initial structure for the dendrimer was generated by a recursive script in CHARMM[38] and equilibrated for over 400 ps in the absence of lipids. At this point the temperature, potential energy, and radius of gyration were stabilized. All images of the molecular structure within this manuscript were created with the software VMD.[40]

Electrostatic interactions are modeled by spatially-dependent screening incorporated by an r-dependent dielectric function of the type $\varepsilon(r)=4r$.[41] This model accounts for the enthalpic electrostatic screening effects of the solvent, but does not incorporate solvent entropic contributions. Non-bonded interactions are cutoff for atom-atom separation distances greater than 1.3 nm and switched at 0.8 nm.

The accuracy of the distance-dependent dielectric function on the dendrimer structure has been previously compared to molecular dynamics in explicit water with counter ions with satisfactory results.[17, 41-44] While the 4r-dependent dielectric solvent model is an approximation relative to explicit water solvation, the size of these simulations, if surrounded by appropriate explicit solvent molecules, would have created a system with a volume of 3,600 nm^3 and 260,000 atoms. Already, simulation of the system with implicit solvent is computationally challenging, especially for the highly demanding process of developing a potential of mean force, as is performed here. Similar calculations using explicit water are currently too computationally demanding. The distance dependent dielectric simulations we perform provide new, meaningful details of the energetics and morphology of dendrimer-phospholipid binding, while avoiding drawbacks that explicit solvent simulations may incorporate, such as excessive computation time impeding the achievement of ergodicity, slow water equilibration, or insufficient averaging of counter ion distribution.

As an example of current difficulties using explicit solvent, recently Chang et al.[45] have performed similar nanoparticle-lipid bilayer molecular dynamics on a considerably smaller system and had difficulty achieving adequate equilibration of the explicit solvent. Their study of lipid-nanoparticle interactions includes a carbon nanoparticle (≈1/10th the

size of the G3 dendrimer) and demonstrates hysteresis effects over the course of the simulations due to the initial water molecule positions and slow water equilibration times. Therefore, the use of implicit solvent will be necessary for computational studies of the dynamics of nanoparticles and membranes for the time being, especially nanoparticles of the relatively large size and internal complexity of dendrimers.

An alternative to the 4r dielectric function is the use of generalized Born solvation models.[46-48] For example, implicit solvent models using the analytical continuum electrostatics (ACE) or generalized Born using molecular volume (GBMV) analysis[49, 50] have been effectively utilized with the CHARMM force field to study protein folding/unfolding.[51, 52] ACE and GBMV and other models[53] have demonstrated, for proteins, good agreement with the thermal unfolding properties reported by experiments and MD simulations with explicit water (with exceptions such as differences in solvent dynamics leading to a dewetting transition.)[54-56] However, our tentative utilization of generalized Born implicit solvent models within simulations of dendrimers and lipids yielded results that were unsatisfactory because of the lack of well established parameters for solvation of lipids in water.

Although an explicit atomic representation of water molecules is the most accurate means to account for the effect of the solvent on molecular kinetics and thermodynamics,[55, 56] we already have presented the computational limitations regarding the simulation for 129 windows for >35,000 dendrimer and lipid atoms in addition to explicit solvent atoms. Additionally the implicit solvent model enhances computational time due through instantaneous (adiabatic) equilibration of implicit water around the solute. If water would be explicitly represented, it would be out of equilibrium for this

duration and the objective of simulating representative dendrimer dynamics in equilibrated water would not be obtained. Implicit representation is not necessarily a poorer choice in this regard because it maintains the time scale separation of water dynamics and dendrimer dynamics by instantaneous relaxation akin to an adiabatic separation. Given these considerations, in combination with the necessity of many trajectories to sample even the most probable conformations reasonably well, we have opted for an implicit water representation.

The constant temperature ensemble was generated using Langevin dynamics to simulate the thermal fluctuations within an implicit solvent by incorporating random fluctuations, ($\mathbf{R}_i(t)$), and a damping constant (γ) into Newton's equations, as shown in Eq. 2. $\mathbf{x}_i$ represents the position of the ith atom of mass m_i in CHARMM potential V,

$$m_i \ddot{\mathbf{x}}_i = -\nabla V\big|_{\mathbf{x}_i} - \gamma m_i \dot{\mathbf{x}}_i + \mathbf{R}_i(t). \qquad (2)$$

The friction coefficient γ is related to $\mathbf{R}_i(t)$ by fluctuation-dissipation; $\langle \mathbf{R}_i(0) \bullet \mathbf{R}_i(t) \rangle = 2m_i k_B T \gamma \delta(t)$. For bulk water, γ=91 ps^{-1}. During equilibration, γ was decreased to 10 ps^{-1} because lower γ values accelerate molecular kinetics while yielding identical equilibrium structures. During dynamics, we set γ=50 ps^{-1} to mimic the decreased viscosity within the dendrimer. During both equilibration and production runs, the temperature was set to 300K.

4.3. RESULTS AND DISCUSSION

The binding of G3-NH_3^+, G3-Ac, and G3-COO^- to DMPC bilayers was simulated (Fig. 4.2). The energetics, macromolecular structure, and mechanisms of interaction are examined with atomistic detail. The PMF has been calculated along the interaction

coordinate defined as the center of mass separation for the dendrimer-lipid system from 2.8 to 6.9 nm (Fig. 4.3). The charged dendrimers (G3-NH_3^+ and G3-COO^-), are more strongly attracted to the lipids than the uncharged dendrimer (G3-Ac). As listed in Table 4.2, the total free energy released upon interaction with the bilayer is 36, 26 and 47 kcal/mol for G3-NH_3^+, G3-Ac, and G3-COO^-, respectively. The majority of the released energy occurs at smaller separation distances, where the dendrimer and lipid have made contact and the attractive force is large. Within these simulations, G3-COO^- released the most energy per molecule upon binding to the DMPC bilayer; however, G3-NH_3^+ released the most energy per mass. As shown in Fig. 4.3B and Table 4.2 with the mass-weighted energy release of binding per dendrimer is 5.2, 3.2, and 4.7 x 10^{-3} kcal/g for G3-NH_3^+, G3-Ac, and G3-COO^-, respectively. In both the per-molecule and per-mass analyses, G3-Ac released the least energy upon binding.

Table 4.2. Simulation results of G3 PAMAM dendrimers binding to DMPC bilayers.

PAMAM Dendrimer	Energy Released Upon Binding		Maximum Attractive force	Maximum Radius of Gyration	Maximum Asphericity
	(kcal/mol)	(10^{-3} kcal/g)	(pN)	(nm)	(10^{-2})
G3-NH_3^+	36	5.2	170	1.55	9
G3-Ac	26	3.2	200	1.3	7
G3-COO^-	47	4.7	240	1.4	6

The derivative of the PMF as a function of the interaction coordinate is the mean force between the dendrimer and lipid bilayer (Fig. 4.4). The attractive force between the dendrimers and lipid bilayers ranged from 0 to 240 pN (Table 4.2), depending on dendrimer termination and dendrimer-lipid separation distance. The attractive force increases as contact is made between the dendrimer and lipids and decreases to zero as

the dendrimer and lipid approach their equilibrium separation distances of $z \approx 3$ nm. The attractive force before contact is made ($z > 4.5$ nm) seems to depend only on the magnitude of dendrimer charge, and not on the sign of the charge; G3-NH_3^+ and G3-COO^- have similar forces of attraction (≈35 pN) in this range. At distances $z < 4.5$ nm, variables such as number of atoms per dendrimer and terminal group size contribute to the differences between the dendrimers. The maximum attractive force is greatest for the carboxyl dendrimer, the largest of the three dendrimers examined.

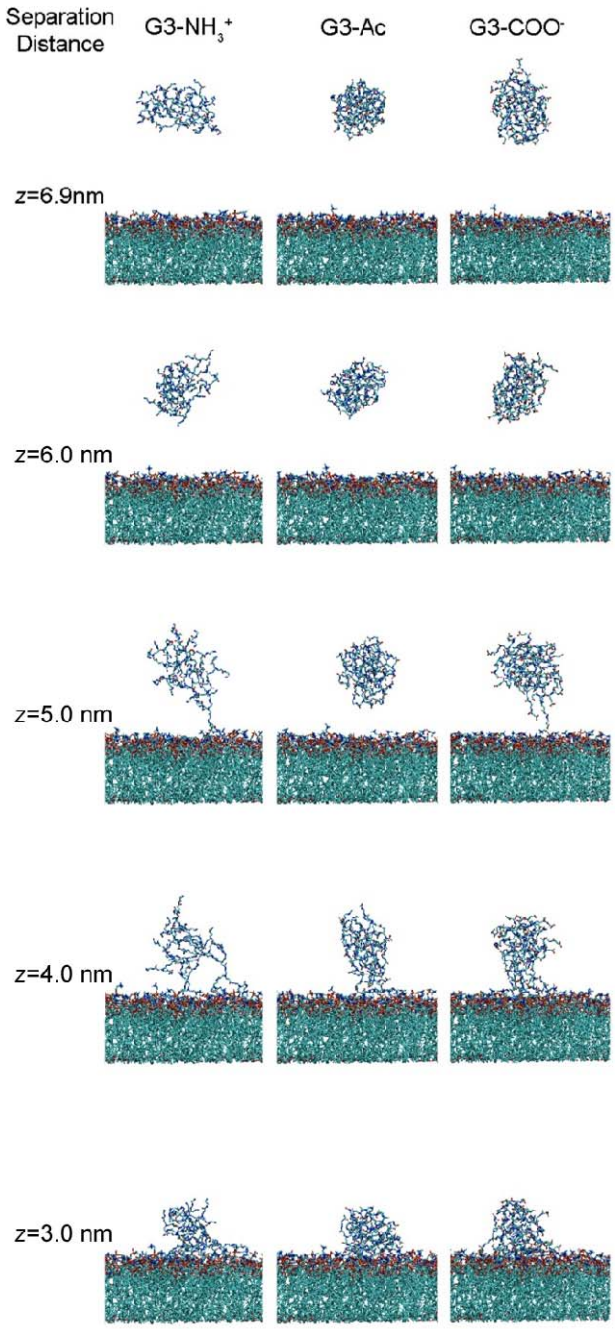

Figure 4.2. Images of G3-NH3+, G3-Ac, and G3-COO- at center of mass separation distances of 6.9, 6.0, 5.0, 4.0, and 3.0 nm from the DMPC bilayer. For z>6 nm, there is no interaction between the dendrimers and lipids. At z = 3nm the dendrimers are near the equilibrium separation, as determined by the potential of mean force (Fig. 4.3). Notice the variation in dendrimers' size, shape, and density, as quantified in Figs. 4.5 and 4.6. Animations of dendrimers binding to the DMPC bilayer are found in the supplemental material.

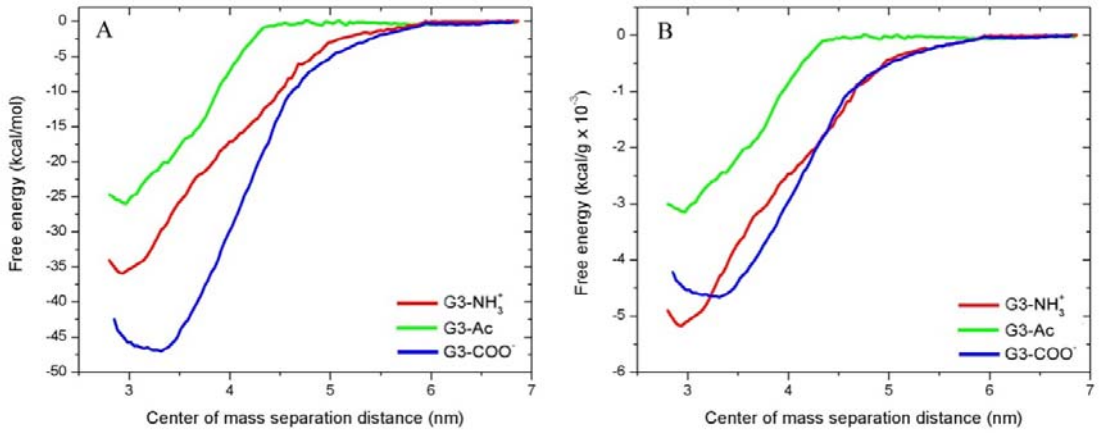

Figure 4.3. Potential of mean forces for dendrimers, of varying termination, binding to DMPC bilayers. (A) shows the energy per molecule binding to the bilayers while (B) shows the energy per mass. The total energy release for the binding is 36, 26, and 47 kcal/mol and 5.2, 3.2, 4.7 x 10-3 kcal/g for the G3-NH3+, G3-Ac, and G3-COO-, respectively.

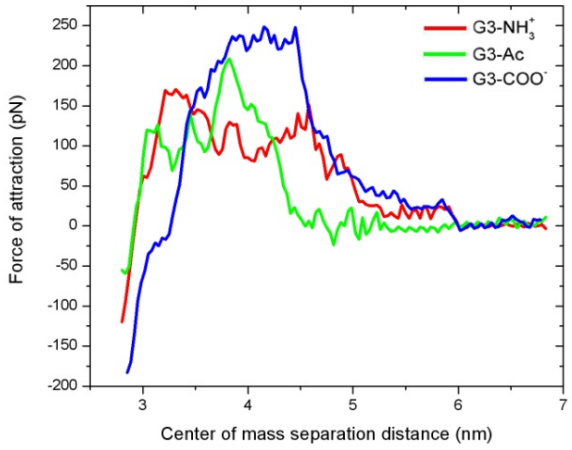

Figure 4.4. Attractive force between dendrimers of varying termination and a DMPC bilayer. There is no force at larger separation distances (z>6 nm), which increases to 170, 200, and 240 pN for G3-NH3+, G3-Ac, and G3-COO-, respectively.

The dendrimer structure is affected by the lipids, as quantified by the dendrimers' radii of gyration within each umbrella sampling window. The radius of gyration (R_G) of a dendrimer represents the magnitude by which the dendrimer atoms are stretched out away from their close-packed state. R_G is calculated according to Eq. 3, incorporating the

dendrimer's mass (M) and center of mass ($\mathbf{x}_0$), in addition to each dendrimer atom's mass (m_i) and position ($\mathbf{x}_i$),

$$R_G = \frac{1}{M}\sqrt{\sum_i m_i \left|\mathbf{x}_i - \mathbf{x}_0\right|^2} \,. \tag{3}$$

The radius of gyration increases, by 19% on average, as the dendrimer approaches the lipids (Fig. 4.5A). As the system becomes close to the equilibrium separation (z<3.7 nm) the radius of gyration decreases to approximately the initial, isolated values. The dendrimer elongates in response to the interactions with the lipid and settles into an equilibrated size similar to that without the influence of lipids. Throughout the entire range of interaction coordinate, the size of the three dendrimers is ordered as G3-NH_3^+ > G3-COO^- > G3-Ac, with the smallest mass dendrimer demonstrating the largest R_G.

The asphericity (A) is a quantifiable description of how deformed from a reference spherical shape the dendrimer has become (Fig. 4.5B). The asphericity has been calculated according to Eq. 4 by comparing the eigenvectors $I_{x,y,z}$ of the dendrimer's moment of inertia matrix,[57]

$$A = 1 - 3\frac{\left\langle I_x I_y + + I_x I_z + I_y I_z \right\rangle}{\left\langle (I_x + I_y + I_z)^2 \right\rangle} \,. \tag{4}$$

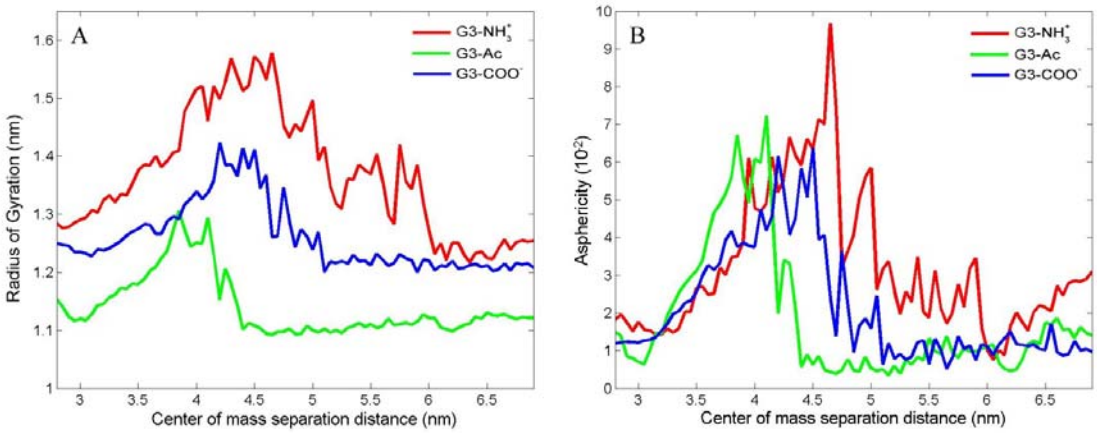

Figure 4.5. Radius of gyration and asphericity versus interaction coordinate for the three different dendrimers. The dendrimers become influenced by the lipids for z<6 nm and the radii of gyration and asphericities increase. Both the radii of gyration and asphericities decreases as the dendrimers approach their equilibrium bound states at z≈3 nm. These results can be qualitatively observed in the images of the simulation shown in Fig. 4.2.

The three dendrimers in this study have similar asphericity (A=0.014) at z≈6 nm, which demonstrates the slight asymmetry in the PAMAM dendrimer core. As the dendrimer and lipids become closer, the asphericities of the dendrimers increase to A≥0.06 at z≈4.2 nm, a 4.3 fold increase. With further decrease in separation, the dendrimer returns to a near spherical shape and settles into the equilibrium interaction coordinate, z≈3 nm, with A=0.015.

Upon decreasing dendrimer-lipid separation distance the dendrimer stretches normal to the bilayer for greater contact with the lipids. This transition to larger asphericity occurs simultaneously with the increasing dendrimer radius of gyration, increased attractive force to the bilayer, and initial contact between the dendrimer and lipids. The charged dendrimers contact the bilayer at z=5.1 nm, while the uncharged dendrimer does not contact the bilayer until z=4.5 nm (Fig. 4.2).

Turning from these average quantities, it is useful to examine the distribution of the dendrimer atoms in more detail. This can provide an understanding of the dendrimer structural change upon binding. Normalized histograms of radial atomic positions from the dendrimers' centers of mass demonstrate the distribution of dendrimer atoms (Fig. 4.6A, B, C) and the terminations (Fig. 4.6D, E, F). At large bilayer-dendrimer separation, the atoms within the dendrimer are distributed with nearly uniform density. Specifically, the dendrimer terminal groups are distributed throughout the dendrimer with both large and small separation distances. This may be surprising, as the terminal groups might be expected to form an outer shell due to electrostatics. At z=4.5 nm the charged terminal groups are pulled away from the dendrimer center as they become attracted to the DMPC bilayer.

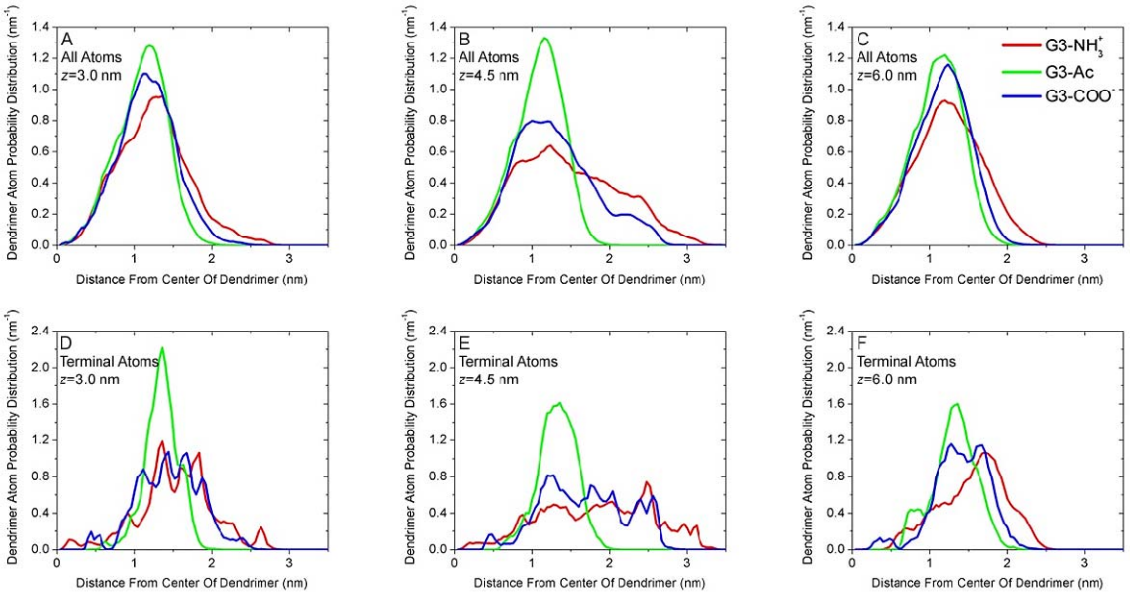

Figure 4.6. Atomic distributions for G3-NH3+, G3-Ac, and G3-COO- at varying interaction coordinates. The vertical axis is a normalized probability distribution of (A, B, C) all dendrimer atoms or (D, E, F) the 32 most terminal carbon or nitrogen atoms in each dendrimer. The horizontal axis is the radial distance from dendrimer center of mass. Results have been averaged over a 4 ns simulation within each sampling window: (A, D) z=3.0 nm, (B, E) z=4.5 nm, and (C, F) z=6.0 nm.

The atomic details of the dendrimer-lipid interaction have been examined at the equilibrium separation distance for all three dendrimers on the DMPC bilayer. Each atom in the DMPC molecule has been compared by its proximity to the dendrimer and differences in the binding morphology of the three dendrimers are identified. The individual atoms on the lipid molecules, as labeled in Fig. 4.7A, have been examined via counting how many of each DMPC atom type are within 2, 3, 4, 5, or 6 Å of the dendrimer (Fig. 4.7B). This analysis considers all DMPC atoms of identical structure as a single type and the resulting count is normalized by the degeneracy of each atom type. The data of Fig. 4.7B has been further compared in Fig. 4.7C by subtracting the data of G3-Ac from the data of G3-NH_3^+ and G3-COO^-. In this way the binding morphology of the charged terminal groups can be more clearly observed. Conclusions from this data include (1) fewer positively charged choline atoms close to G3-NH_3^+, (2) more negatively charged phosphate atoms are close to G3-NH_3^+, (3) fewer negatively charged phosphate atoms are close to G3-COO^-, and (4) G3-NH_3^+ are able to penetrate deeper into the DMPC bilayer and closer to more of the glycerol atoms.

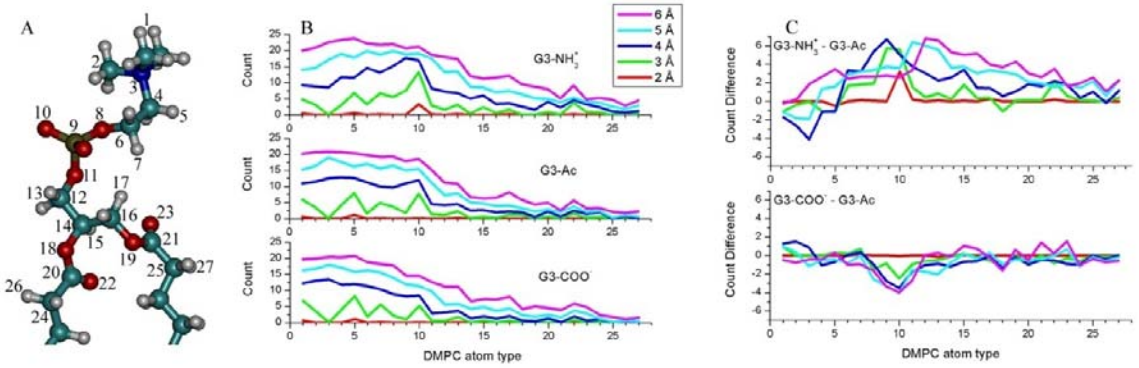

Figure 4.7. Plot of which DMPC atoms are in close proximity to each dendrimer at the equilibrium dendrimer-lipid separation distance. The atoms in each DMPC molecule have been assigned a number, according to (A), and plotted on the horizontal axis of (B) and (C). Identical DMPC atoms have been assigned the same number and the results have been normalized appropriately. The vertical axis of (B) represents the average number of DMPC atoms of each type that are within 2, 3, 4, 5, or 6 Å of the dendrimer at

the equilibrium interaction coordinate. (C) shows the difference between the charged and uncharged dendrimers.

The morphology of the equilibrated structure is examined in terms of the area that the dendrimers occupy over the lipid bilayer. The dendrimers cover an area of 9.6, 8.2, or 7.9 nm^2 for G3-NH_3^+, G3-AC, or G3-COO^-, respectively, with G3-NH_3^+ flattening out the most in covering the greatest area of lipids. This analysis measures the footprint, or the area of their shadow on the lipids. The structures have also been examined by the area of the smallest circle inscribing the projection of the dendrimer on to the bilayer plane. The smallest circles containing the dendrimer have area of 14.9, 9.4, or 10.4 nm^2 for G3-NH_3^+, G3-AC, or G3-COO^-, respectively. By comparing the size of the inscribing circle to the size of the dendrimer footprint, it is revealed how spherically symmetrical and dense the dendrimers are over the bilayer. G3-NH_3^+ stretches out the farthest on the bilayer, as represented by its largest inscribing circle. These effects are observed qualitatively in the top view of the bound dendrimers in Fig. 4.8. Interestingly, G3-COO^- is the largest mass dendrimer, but displays the smallest footprint upon binding to the lipids. This is one of the many ways by which the longer termination of G3-COO^- affects atomic structure and yields considerable differences from the other terminations.

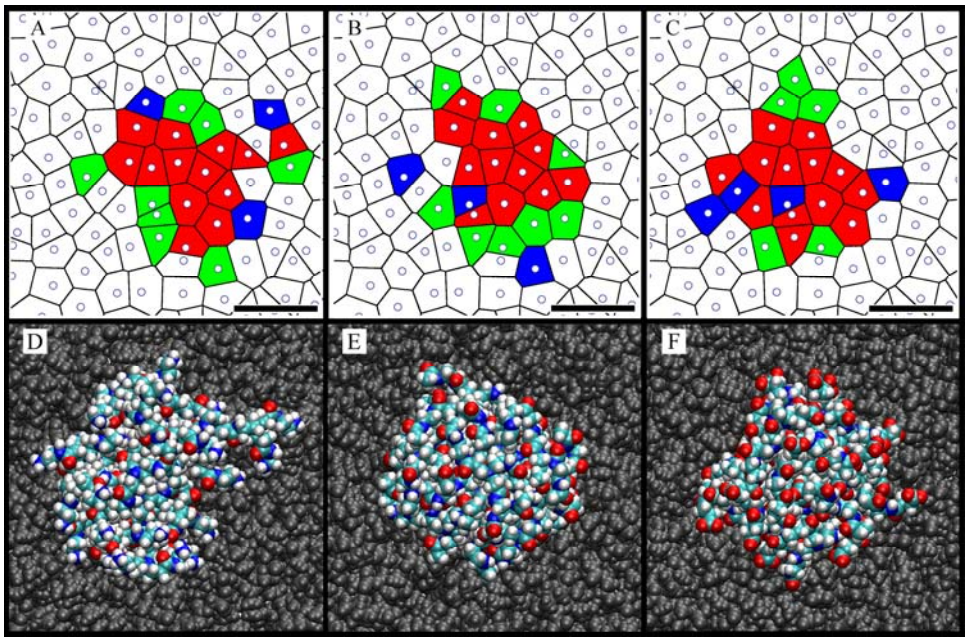

Figure 4.8. (A, B, C) Voronoi diagram of the top leaflet of the DMPC bilayer with coloration according to portion of time each DMPC molecule is within 3 Å of the dendrimer. (D, E, F) Top view of dendrimers bound to the bilayer. (A, D) G3-NH3+, (B, E) G3-Ac, and (C, F) G3-COO-. (A, B, C) Circles correspond to each lipid molecule's center of mass projected onto the bilayer plane and the thin black lines represent the boundaries between lipid molecules. Lipid molecules colored red represent those that are within 3 Å of the dendrimer in 100% of the simulation frames; green indicates close proximity 50-100% of the time and blue indicates 1-50%. Scale bar in each image is 2 nm. (D, E, F) Lipids are colored grey and dendrimers are colored cyan, blue, white and red for atom types C, N, H, and O, respectively.

A final analysis of the morphology of the dendrimers equilibrated on the DMPC bilayers was performed with a Voronoi diagram (Fig. 4.8A, B, C).[58] Each circle represents the center of mass of a DMPC molecule on the top bilayer leaflet projected onto the bilayer plane. The thin black lines represent the division between DMPC molecules and those points that are half way between the two closest lipids. This representation provides a mapping of the top DMPC leaflet with which we can map which DMPC molecules are strongly interacting with the bound dendrimers. This has been represented by a coloration of the DMPC molecules on the Voronoi diagram. DMPC molecules that are within 3 Å of the dendrimer for 100% of the acquired

simulation frames of the equilibrated structure are colored red; those that are within 3 Å of the dendrimer in 50 – 100% of frames are colored green and 1-50% are colored blue.

The surprising result from these Voronoi diagrams is the similarity between the number and distribution of lipids in close proximity to the dendrimers, regardless of the dendrimer termination. All three dendrimers are within 3 Å of 12 - 13 particular lipid molecules in all of the simulation frames, 5 – 8 lipids are within 3 Å for 50 – 100% of the frames, and 3 – 4 lipids are within 3 Å for 1 – 50% of the frames. Variations between dendrimer binding morphologies (number of lipids, likelihood of switching between lipids, etc.) as a function of dendrimer termination are possible, although not observed over this time scale. Combined analysis of Fig. 4.8 and Table 4.3 provides a quantitative understanding of bound configuration of a G3 PAMAM dendrimer on a DMPC bilayer.

Table 4.3. Area occupied by the dendrimers on the lipid bilayer.

PAMAM Dendrimer	Area of dendrimer foot print (nm^2)[A]	Area of inscribing circle (nm^2) [A]
G3-NH_3^+	9.6	14.9
G3-Ac	8.2	9.4
G3-COO^-	7.9	10.4

[A] The standard deviation of observed areas was 2% for the footprints and 6% for the inscribing circles.

4.4. CONCLUSIONS

Simulations have been performed to quantitatively analyze the interaction between G3 PAMAM dendrimers of varying terminal chemistry to DMPC lipid bilayers. Three different dendrimer terminations were simulated. The 32 end groups of each G3 dendrimer are modified to all be either positively charged primary amine, uncharged acetamide, or negatively charged carboxyl. Umbrella sampling is performed along the

interaction coordinate defined as the center of mass separation of the dendrimer and lipid bilayer and the potential of mean force is calculated. These simulations are of importance due to their quantitative analysis of the dendrimer-lipid interaction. The calculated forces and energies of interaction are similar to those from other known ligand binding forces[59] and aid in the design of functionalized nanoparticles for biomedical applications.

The qualitative conclusions from these simulations are identical to those observed experimentally: charged dendrimers more favorably interact with zwitterionic membranes than do neutral dendrimers. Additionally, these simulations provide a quantitative description of this interaction. An average force of 35 pN attracts the charged dendrimers to the lipid before the dendrimer and lipid make contact with each other. In contrast, neutral dendrimers have negligible interactions. After the dendrimer has made contact with the lipids, average attractive forces of 170, 200, and 240 pN are observed for G3-NH_3^+, G3-Ac, and G3-COO^-, respectively. A net free energy release for dendrimer binding to the DMPC bilayers is measured to be 36, 26, 47 kcal/mol and 5.2, 3.2, 4.7 x 10^{-3} kcal/g for G3-NH_3^+, G3-Ac, and G3-COO^-, respectively.

These results are directly applicable to nanodevice design, or other nanoparticles, for medical purposes. This research contributes to the growing understanding of the critical importance of nanoparticle size and surface chemistry to biological activity. Nanodevices utilized for gene delivery applications commonly exploit cationic nanoparticles for strong binding to nucleic acids.[9, 10, 60-62] However, targeting these gene delivery nanodevices is challenging due to the influence of the remaining charged terminal groups. By further comparing the forces and energies of non-specific

nanoparticle binding to relevant system components, such as targeting moieties and cellular receptors, optimized nanoparticles can be designed and implemented.

4.5 ACKNOWLEDGMENTS

Pascale R. Leroueil,Elizabeth K. Nett, Jeffery M. Wereszczynski, James R. Baker, Jr., Bradford G. Orr, Mark M. Banaszak Holl, and Ioan Andricioaei were essential contributors to this research. Fellowship support was received from the NIH Michigan Molecular Biophysics Training Program (T32 GM008270-20), the Applied Physics program, and the Graham Environmental Sustainability Institute. Computational time was provided by the Center for Advanced Computing at the University of Michigan and Lawrence Livermore National Laboratory. The authors thank Christine Orme and Timothy Sullivan. This research was supported by a grant from the National Institute of Biomedical Imaging and BioEngineering (R01-EB005028) and from the NSF CAREER award program (CHE-0548047).

4.6. REFERENCES

1. Hong, S. P.; Bielinska, A. U.; Mecke, A.; Keszler, B.; Beals, J. L.; Shi, X. Y.; Balogh, L.; Orr, B. G.; Baker, J. R.; Holl, M. M. B., Interaction of poly(amidoamine) dendrimers with supported lipid bilayers and cells: Hole formation and the relation to transport. *Bioconjugate chemistry* **2004,** 15, (4), 774-782.
2. Hong, S. P.; Leroueil, P. R.; Janus, E. K.; Peters, J. L.; Kober, M. M.; Islam, M. T.; Orr, B. G.; Baker, J. R.; Holl, M. M. B., Interaction of polycationic polymers with supported lipid bilayers and cells: Nanoscale hole formation and enhanced membrane permeability. *Bioconjugate Chemistry* **2006,** 17, (3), 728-734.
3. Leroueil, P. R.; Hong, S. Y.; Mecke, A.; Baker, J. R.; Orr, B. G.; Holl, M. M. B., Nanoparticle interaction with biological membranes: Does nanotechnology present a janus face? *Accounts of Chemical Research* **2007,** 40, (5), 335-342.
4. Qiao, R.; Roberts, A. P.; Mount, A. S.; Klaine, S. J.; Ke, P. C., Translocation of C-60 and its derivatives across a lipid bilayer. *Nano Letters* **2007,** 7, (3), 614-619.
5. Xing, X. L.; He, X. X.; Peng, J. F.; Wang, K. M.; Tan, W. H., Uptake of silica-coated nanoparticles by HeLa cells. *Journal of Nanoscience and Nanotechnology* **2005,** 5, (10), 1688-1693.
6. Manunta, M.; Nichols, B. J.; Tan, P. H.; Sagoo, P.; Harper, J.; George, A. J. T., Gene delivery by dendrimers operates via different pathways in different cells, but is enhanced by the presence of caveolin. *Journal of Immunological Methods* **2006,** 314, (1-2), 134-146.
7. Chithrani, B. D.; Ghazani, A. A.; Chan, W. C. W., Determining the size and shape dependence of gold nanoparticle uptake into mammalian cells. *Nano Letters* **2006,** 6, (4), 662-668.
8. Manunta, M.; Tan, P. H.; Sagoo, P.; Kashefi, K.; George, A. J. T., Gene delivery by dendrimers operates via a cholesterol dependent pathway. *Nucleic Acids Research* **2004,** 32, (9), 2730-2739.
9. Pack, D. W.; Hoffman, A. S.; Pun, S.; Stayton, P. S., Design and development of polymers for gene delivery. *Nature Reviews Drug Discovery* **2005,** 4, (7), 581-593.
10. Quintana, A.; Raczka, E.; Piehler, L.; Lee, I.; Myc, A.; Majoros, I.; Patri, A. K.; Thomas, T.; Mule, J.; Baker, J. R., Design and function of a dendrimer-based therapeutic nanodevice targeted to tumor cells through the folate receptor. *Pharmaceutical research* **2002,** 19, (9), 1310-1316.
11. Duncan, R.; Izzo, L., Dendrimer biocompatibility and toxicity. *Advanced Drug Delivery Reviews* **2005,** 57, (15), 2215-2237.
12. Tomalia, D. A., Birth of a new macromolecular architecture: dendrimers as quantized building blocks for nanoscale synthetic polymer chemistry. *Progress in Polymer Science* **2005,** 30, (3-4), 294-324.
13. Landmark, K. J.; DiMaggio, S.; Ward, J.; Vogt, S.; Hong, S.; Kotlyar, A.; Penner-Hahn, J. E.; James R. Baker, J.; Holl, M. M. B.; Orr, B. G., Synthesis, Characterization, and In Vitro Testing of Superparamagnetic Iron Oxide Nanoparticles Targeted Using Folic Acid-Conjugated Dendrimers. *Submitted* **2007**.
14. Majoros, I. J.; Thomas, T. P.; Mehta, C. B.; Baker, J. R., Poly(amidoamine) dendrimer-based multifunctional engineered nanodevice for cancer therapy. *Journal of medicinal chemistry* **2005,** 48, (19), 5892-5899.

15. Patri, A. K.; Majoros, I. J.; Baker, J. R., Dendritic polymer macromolecular carriers for drug delivery. *Curr. Opin. Chem. Biol.* **2002,** 6, (4), 46-471
16. Choi, Y.; Baker, J. R., Targeting cancer cells with DNA-Assembled dendrimers - A mix and match strategy for cancer. *Cell Cycle* **2005,** 4, (5), 669-671.
17. Mecke, A.; Lee, I.; Baker, J. R.; Holl, M. M. B.; Orr, B. G., Deformability of poly(amidoamine) dendrimers. *European Physical Journal E* **2004,** 14, (1), 7-16.
18. Mecke, A.; Majoros, I. J.; Patri, A. K.; Baker, J. R.; Holl, M. M. B.; Orr, B. G., Lipid bilayer disruption by polycationic polymers: The roles of size and chemical functional group. *Langmuir* **2005,** 21, (23), 10348-10354.
19. Mecke, A.; Uppuluri, S.; Sassanella, T. M.; Lee, D. K.; Ramamoorthy, A.; Baker, J. R.; Orr, B. G.; Holl, M. M. B., Direct observation of lipid bilayer disruption by poly(amidoamine) dendrimers. *Chemistry and physics of lipids* **2004,** 132, (1), 3-14.
20. Ginzburg, V. V.; Balijepalli, S., Modeling the Thermodynamics of the Interaction of Nanoparticles with Cell Membranes. *Nano Lett.* **2007**.
21. Lee, H.; Larson, R. G., Molecular Dynamics Simulations of PAMAM Dendrimer-Induced Pore Formation in DPPC Bilayers with a Coarse-Grained Model. *J.Phys.Chem.B 2006, 110, 18204-18211* **2006,** 110, 18204-18211.
22. Torrie, G. M.; Valleau, J. P., Non-Physical Sampling Distributions in Monte-Carlo Free-Energy Estimation - Umbrella Sampling. *Journal of Computational Physics* **1977,** 23, (2), 187-199.
23. Kumar, S.; Bourzida, D.; Swendsen, R. H.; Kollman, P. A.; Rosenberg, J. M., The Weighted Histogram Analysis Method for Free-Energy Calculations on Biomolecules .1. the Method. *Journal of Computational Chemistry* **1992,** 13, (8), 1011-1021.
24. Kirkwood, J., Statistical mechanics of fluid mixtures. *Journal Of Chemical Physics* **1935,** 3, 300-313.
25. Brooks, B. R.; Bruccoleri, R. E.; Olafson, B. D.; States, D. J.; Swaminathan, S.; Karplus, M., Charmm - a Program for Macromolecular Energy, Minimization, and Dynamics Calculations. *Journal of Computational Chemistry* **1983,** 4, (2), 187-217.
26. MacKerell, A. D.; Bashford, D.; Bellott, M.; Dunbrack, R. L.; Evanseck, J. D.; Field, M. J.; Fischer, S.; Gao, J.; Guo, H.; Ha, S.; Joseph-McCarthy, D.; Kuchnir, L.; Kuczera, K.; Lau, F. T. K.; Mattos, C.; Michnick, S.; Ngo, T.; Nguyen, D. T.; Prodhom, B.; Reiher, W. E.; Roux, B.; Schlenkrich, M.; Smith, J. C.; Stote, R.; Straub, J.; Watanabe, M.; Wiorkiewicz-Kuczera, J.; Yin, D.; Karplus, M., All-atom empirical potential for molecular modeling and dynamics studies of proteins. *Journal of Physical Chemistry B* **1998,** 102, (18), 3586-3616.
27. Roux, B., The Calculation of the Potential of Mean Force using Computer-Simulations. *Computer Physics Communications* **1995,** 91, (1-3), 275-282.
28. Mitchell, J. B. O.; Laskowski, R. A.; Alex, A.; Thornton, J. M., BLEEP - Potential of mean force describing protein-ligand interactions: I. Generating potential. *Journal Of Computational Chemistry* **1999,** 20, 1165-1176.
29. Roux, B.; Karplus, M., Ion-transport in a model gramicidin channel - structure and thermodynamics. *Biophysical journal* **1991,** 59, 961-981.
30. Sprik, M.; Ciccotti, G., Free energy from constrained molecular dynamics. *Journal Of Chemical Physics* **1998,** 109, 7737-7744.
31. Johnson, S. J.; Bayerl, T. M.; McDermott, D. C.; Adam, G. W.; Rennie, A. R.; Thomas, R. K.; Sackmann, E., Structure of an Adsorbed Dimyristoylphosphatidylcholine

Bilayer Measured with Specular Reflection of Neutrons. *Biophysical journal* **1991,** 59, (2), 289-294.
32. Kucerka, N.; Liu, Y. F.; Chu, N. J.; Petrache, H. I.; Tristram-Nagle, S. T.; Nagle, J. F., Structure of fully hydrated fluid phase DMPC and DLPC lipid bilayers using X-ray scattering from oriented multilamellar arrays and from unilamellar vesicles. *Biophysical journal* **2005,** 88, (4), 2626-2637.
33. Zhang, Z. Y.; Smith, B. D., High-generation polycationic dendrimers are unusually effective at disrupting anionic vesicles: Membrane bending model. *Bioconjugate Chemistry* **2000,** 11, (6), 805-814.
34. Karoonuthaisiri, N.; Titiyevskiy, K.; Thomas, J. L., Destabilization of fatty acid-containing liposomes by. polyamidoamine dendrimers. *Colloids and Surfaces B-Biointerfaces* **2003,** 27, (4), 365-375.
35. Fischer, D.; Li, Y. X.; Ahlemeyer, B.; Krieglstein, J.; Kissel, T., In vitro cytotoxicity testing of polycations: influence of polymer structure on cell viability and hemolysis. *Biomaterials* **2003,** 24, (7), 1121-1131.
36. Kelly, C. V.; Leroueil, P. R.; Orr, B. G.; Holl, M. M. B.; Andricioaei, I., Poly(amidoamine) dendrimers on lipid bilayers II: effects of bilayer phase and dendrimer termination. *Submitted* **2008**.
37. Feller, S. E.; MacKerell, A. D., An improved empirical potential energy function for molecular simulations of phospholipids. *Journal of Physical Chemistry B* **2000,** 104, (31), 7510-7515.
38. Mercier, G. A., Dendrimer Builder. *http://server.ccl.net/chemistry/resources/messages/1996/05/20.009-dir/index.html* **1996**.
39. Maiti, P. K.; Cagin, T.; Lin, S. T.; Goddard, W. A., Effect of solvent and pH on the structure of PAMAM dendrimers. *Macromolecules* **2005,** 38, (3), 979-991.
40. Humphrey, W.; Dalke, A.; Schulten, K., VMD: Visual molecular dynamics. *Journal of Molecular Graphics* **1996,** 14, (1), 33.
41. Pickersgill, R. W., A rapid method of calculating charge charge interaction energies in proteins. *Protein engineering* **1988,** 2, 247-248.
42. Lee, I.; Athey, B. D.; Wetzel, A. W.; Meixner, W.; Baker, J. R., Structural molecular dynamics studies on polyamidoamine dendrimers for a therapeutic application: Effects of pH and generation. *Macromolecules* **2002,** 35, (11), 4510-4520.
43. Paulo, P. M. R.; Lopes, J. N. C.; Costa, S. M. B., Molecular Dynamics Simulations of Charged Dendrimers: Low-to-Intermediate Half-Generation PAMAMs. *J. Phys. Chem. B* **2007,** 111, (36), 10651-10664.
44. Brooks, C. L.; Karplus, M.; Pettitt, B. M., *Proteins: A Theoretical Perspective of Dynamics, Structure, and Thermodynamics*. John Wiley & Sons: 1990.
45. Chang, R.; Violi, A., Insights into the effect of combustion-generated carbon nanoparticles on biological membranes: A computer simulation study. *Journal of Physical Chemistry B* **2006,** 110, (10), 5073-5083.
46. Feig, M.; Brooks, C. L., Recent advances in the development and application of implicit solvent models in biomolecule simulations. *Current Opinion in Structural Biology* **2004,** 14, (2), 217-224.
47. Bashford, D.; Case, D. A., Generalized born models of macromolecular solvation effects. *Annual Review of Physical Chemistry* **2000,** 51, 129-152.

48. Qiu, D.; Shenkin, P. S.; Hollinger, F. P.; Still, W. C., The GB/SA continuum model for solvation. A fast analytical method for the calculation of approximate Born radii. *Journal of Physical Chemistry A* **1997,** 101, (16), 3005-3014.
49. Dominy, B. N.; Brooks, C. L., Development of a generalized born model parametrization for proteins and nucleic acids. *Journal of Physical Chemistry B* **1999,** 103, (18), 3765-3773.
50. Schaefer, M.; Karplus, M., A comprehensive analytical treatment of continuum electrostatics. *Journal of Physical Chemistry* **1996,** 100, 1578-1599.
51. Schaefer, M.; Bartels, C. M., Solution Conformations and Thermodynamics of Structured Peptides: Molecular Dynamics Simulation with an Implicit Solvation Model. *Journal of Molecular Biology* **1998,** 284, 835-848.
52. Calimet, N.; M.; Simonson, T., Protein Molecular Dynamics With the Generalized Born/ACE Solvent Model. *Proteins* **2001,** 45, 144-158.
53. Lazaridis, T.; Karplus, M., Effective energy function for proteins in solution. *Proteins-Structure Function and Genetics* **1999,** 35, (2), 133-152.
54. Rhee, Y. M.; Sorin, E. J.; Jayachandran, G.; Lindahl, E.; Pande, V. S., Simulations of the role of water in the protein-folding mechanism. *Proceedings of the National Academy of Sciences of the United States of America* **2004,** 101, 6456-6461.
55. ten Wolde, P. R.; Chandler, D., Drying-induced hydrophobic polymer collapse. *Proceedings of the National Academy of Sciences of the United States of America* **2002,** 99, 6539-6543.
56. Zhou, R. H.; Huang, X. H.; Margulis, C. J.; Berne, B. J., Hydrophobic collapse in multidomain protein folding. *Science* **2004,** 305, 1605-1609.
57. Rudnick, J.; Gaspari, G., The asphericity of random walks. *Journal of Physics A: Math. Gen.* **1986,** 19, L191-L193.
58. Voronoi, G. F., Nouvelles applications des paramètres continus à la théorie des formes quadratiques. *Journal für die Reine und Angewandte Mathematik* **1907,** 133, (97-178).
59. Moy, V. T.; Florin, E. L.; Gaub, H. E., Intermolecular Forces and Energies between Ligands and Receptors. *Science* **1994,** 266, (5183), 257-259.
60. Han, S.; Mahato, R. I.; Sung, Y. K.; Kim, S. W., Development of biomaterials for gene therapy. *Molecular Therapy* **2000,** 2, (4), 302-317.
61. Tang, M. X.; Redemann, C. T.; Szoka, F. C., In vitro gene delivery by degraded polyamidoamine dendrimers. *Bioconjugate Chemistry* **1996,** 7, (6), 703-714.
62. Haensler, J.; Szoka, F. C., POLYAMIDOAMINE CASCADE POLYMERS MEDIATE EFFICIENT TRANSFECTION OF CELLS IN CULTURE. *Bioconjugate Chemistry* **1993,** 4, (5), 372-379.

CHAPTER 5

POLY(AMIDOAMINE) DENDRIMERS ON LIPID BILAYERS II: EFFECTS OF BILAYER PHASE AND DENDRIMER TERMINATION

5.1. INTRODUCTION

Dendrimers are a major class of synthetic polymers currently in development for applications such as gene delivery, targeted drug delivery, and enhanced in vivo imaging.[1-5] Poly(amidoamine) (PAMAM) dendrimers, in particular, have shown to be very promising in these areas (Fig. 5.1).[6-10] Although attempts have been made to elucidate the mechanisms of polymer binding and internalization on living cells,[11-22] there is still much work to be done before fully capable nanodevices can be designed and created due to the remaining unknown mechanisms of nanoparticle-membrane interaction.

To address complicated, multi-component biological systems, models often dissect which components are most relevant to the observed or desired behavior. Lipid molecules are the most prevalent component of the plasma membrane and a more thorough understanding of the interaction of nanoparticles with lipid molecules will address many relevant issues pertaining to real cells. Lipid bilayer models have been shown to give qualitatively accurate predictions for in vitro cell studies in regards to membrane permeability and polymer internalization.[12, 18-20, 23, 24]

PAMAM dendrimers are used in medical applications for many of the same reasons that also make them good models for nanotoxicity and polymer internalization studies; dendrimers have high homogeneity (polydispersity index≈1.01), high water solubility, numerous modifiable end-groups, low immunogenicity, small diameter (<10 nm), and are highly deformable for multivalent interactions.[8, 9, 21, 25] The heterogeneous nature of other polymer samples often prevent researchers from determining which particle properties are inducing the observed cellular response. By contrast, because of their homogeneity, PAMAM dendrimers are prime study cases and are utilized in a focused approach as models to address many specific issues in cell biology, nanotoxicity, and medicine.

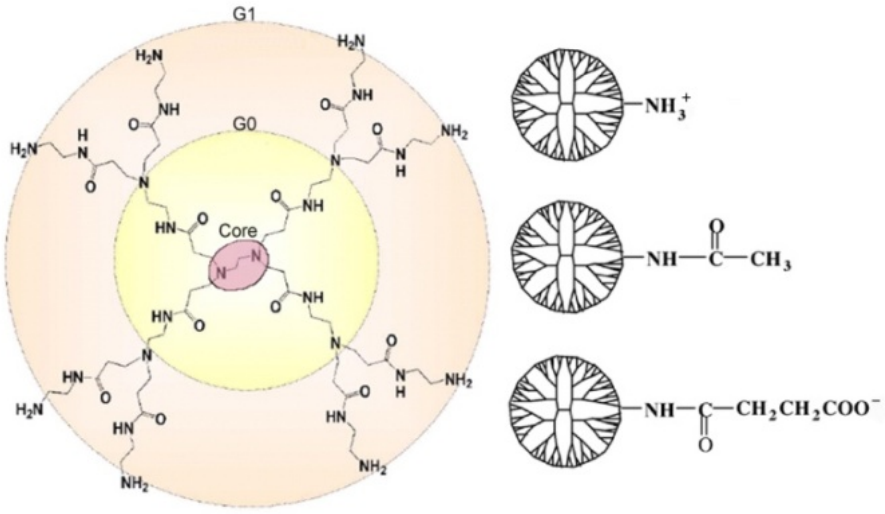

Figure 5.1. The atomic structure of first-generation (G1) PAMAM dendrimer and terminal groups: protonated primary amine ($-NH_3^+$), uncharged acetamide (-Ac), and deprotonated carboxylic acid ($-COO^-$). There are 32 terminal groups per G3 dendrimer and they are all modified to become +32e charged G3-NH_3^+, uncharged G3-AC, and the -32e charged G3-COO^-.

A companion paper addressing the binding free energy profile along the interaction coordinate and the morphology of generation-3 (G3) PAMAM dendrimers on

DMPC bilayers is also found within this publication.[17] The purpose of the present paper is to address, in a comparative manner, the differences between the dendrimer interaction with a fluid phase and with a gel phase of the lipid bilayer. This is important because experimental studies have shown that fluid phase lipids exposed to polymers have increased propensity to yield membrane pore formation, membrane leakage, and particle internalization, whereas the gel phase lipids tend to be more resistive to permeation and degradation.[20, 24] Our study will aid in achieving a better understanding of the binding and internalization mechanisms of polymers into living cells. Particularly, the means by which polymers interact with the fluid vs. gel phases of the lipid bilayers are important to cellular mechanisms involving lipid rafts and endocytosis.[26-28]

The polymer's surface greatly influences its interaction with cells. Active polymer targeting with specific receptor binding can be hindered by charged polymer moieties, such as protonated primary amine or deprotonated carboxylic acid. This is due to the highly energetic non-specific binding of these polymers to both targeted and non-targeted cells alike.[7, 8] Moreover, model membranes are heavily degraded by charged polymers, whereas neutral polymers cause less membrane disruption.[12, 18, 19]

Atomic force microscopy (AFM) has yielded nanometer resolution images of supported DMPC bilayers affected by PAMAM dendrimers of various generations (G3, G5, and G7) and terminations (primary amine, acetamide, and carboxylic acid).[19, 23] Experimental studies have shown that increasing dendrimer size or charge magnitude yields greater bilayer disturbance, as consistent with previous observations of a surface area dependance.[18, 29] It was also observed that no disruption of gel phase bilayers occurred, whereas neighboring fluid phase bilayers were highly degraded by primary

amine-terminated, G7 PAMAM dendrimers.[20] These studies demonstrated a strong dependence on dendrimer and lipid properties for the resulting dendrimer-bilayer interaction.

The binding of dendrimers to lipid bilayers has been previously explored computationally via coarse-grained molecular dynamics by Lee et al.[22] That study approximated the PAMAM dendrimers and 1,2-dipalmitoyl-*sn*-glycero-3-phosphocholine (DPPC) bilayer through the motion of computer-modeled beads designed to each represent approximately four heavy atoms and associated hydrogen atoms. That coarse graining procedure was an extension of the coarse grained force field developed by Marrinick and coworkers for proteins.[30] Even though the simulations involved no dendrimer-dendrimer interactions and only 0.5 μs simulation time, observations of G3 and G5 PAMAM dendrimers of varying acetylation on bilayers in the gel and fluid phases were roughly consistent with those from AFM. Coarse grained simulations yielded significant morphology differences for the dendrimers bound to gel vs. fluid phase bilayers. The primary amine terminated dendrimers bound to the fluid phase lipids, deformed, intercalated into the bilayer, and interacted with the lipid tails. In contrast, the dendrimers bound to the gel phase were confined to the top of the bilayer in a compact shape.

Lee et al.[22] observed that the morphology of the bound dendrimer varied greatly with dendrimer termination such that the amine terminated dendrimers caused bilayer pores, whereas the acetylated dendrimers avoided contact with the lipid tails, regardless of lipid phase. This observation is somewhat different from the AFM conclusions, which postulated that the acetylated G5 dendrimers rested fully within the lipid tail region and

were not seen on the surface of intact bilayers. These differences could easily be attributed to the short simulation time, approximate simulation force-field parameters, experimental artifacts from the mica supporting the lipids, and/or incorrect interpretation of the AFM data which only provided topographic and elastic information.

Our work presented in this manuscript uses an all-atom simulation to examine the binding of G3 PAMAM dendrimers of multiple terminations to lipids of varying phase for a more thorough understanding of the atomistic differences in dendrimer-membrane binding. Three hypotheses are put forth to elucidate the mechanisms of dendrimer-lipid binding. They demonstrate our expected dependence of the resulting interaction on the lipid phase and the dendrimer termination:

Hypothesis 1: The fluid phase lipid bilayer deforms to accommodate dendrimer-lipid interactions with more of the dendrimer and lipids in contact than the gel phase lipids.

Hypothesis 2: The dendrimers achieve a stronger interaction energy with fluid phase lipids than gel phase lipids due to the mobility of the fluid phase lipids allowing the dendrimers' terminal groups to obtain more favorable interactions.

Hypothesis 3: The charged dendrimers (G3-NH_3^+ and G3-COO^-) release more enthalpy upon binding than the uncharged dendrimer (G3-Ac) and, as such, the charged dendrimers are more morphologically altered upon binding.

The results presented here support the first hypothesis while providing counter evidence to the second and third hypotheses. In comparison to the hydrophobic dendrimer moieties, the dendrimer terminal groups make a relatively small contribution to the fluid vs. gel phase lipid energetics and deformation upon binding. Within this

manuscript the morphology and the mechanisms of dendrimer bound to lipid bilayers is examined quantitatively. Through these atomistic simulations, greater detail is obtained about the particular atomic configuration and morphology of the bound structures, as well as the enthalpic components to binding. The dendrimer radius of gyration, asphericity, and elastic energy of deformation are examined to quantitatively describe the dendrimer during binding. Further, the number and type of dendrimer-lipid contacts are described both morphologically and enthalpically. Through this analysis we directly address our three hypotheses.

5.2. METHODS

Atomistic simulations of G3 PAMAM dendrimers and DMPC lipids were performed. Dendrimer parameters were constructed from the CHARMM parameters for generic proteins (para22) whereas the lipid (DMPC) parameters came directly from CHARMM27.[31, 32] Simulations were run at 300 K with non-bonded interactions cutoff at 13 Å and switched from 8 Å. Time steps of 2 fs were taken with implementation of the SHAKE routine to remove variation in hydrogen atom bond lengths.

Initial dendrimer configurations were made with a recursive script in CHARMM.[33] Both the dendrimer and the lipids were separately equilibrated for 2 ns before being were combined into nine different simulations (3 dendrimers with 3 lipid states). All simulations ran until dendrimers stopped moving along the direction perpendicular to the lipid bilayer for more than 5 ns; the total simulation time for all nine systems was 90 ns. The atomic configurations were analyzed every 2 ps over the final 4 ns. All systems required greater than 10 ns to transition from initially contacting the fluid

phase bilayer to fully bind. All images of the molecular structure within this manuscript were created with the software VMD.[34]

The effects of the solvent were modeled implicitly by a distance dependent dielectric ($\varepsilon = 4r$) to mimic solvent screening effects and to make the atomistic simulations of macromolecules computationally feasible. This solvent approximation has been used previously in molecular dynamics simulations of macromolecules, such as dendrimers, and yielded reasonable agreement with experimental results.[17, 21, 35, 36] An explicit solvent representation in this large (3,600 nm^3) system would require an exceedingly long sampling time, and as such was deemed unfeasible for the present purpose. A more thorough discussion of the implications and rational behind this approximation is given in the companion manuscript also in this journal.[17] Generalized Born solvation models were examined but not pursued due to the lack of appropriate parameterization.[37, 38]

The lipid phase was imposed on the bilayer by varying the amount of restriction on the mobility of the lipid tails. The boundary condition for the fluid phase bilayer was a cylinder of fixed lipid molecules with an inner diameter of 10 nm. This setup maintains experimentally determined lipid surface density and bilayer thickness[39, 40] while permitting a circular lipid bilayer which drastically decreased computational time by reducing the number of lipid molecules as compared to a rectangular patch with periodic boundary conditions (while the latter conditions tend to be generally considered more accurate because they eliminate end-effects, they are not free of artifacts, either[41]). Membrane undulations may be an important aspect of nanoparticle-membrane interactions and are limited to length scales of the simulated system. However, the small

size of membrane simulations does not contribute to the disagreements in experimental and simulated membrane structural properties.[42]

This membrane model of a 10 nm lipid disk provided sufficient surroundings for the dendrimer to not sense the end of the lipids directly (i.e., the smallest distance between any dendrimer atom and the lipid edge was smaller than the cut-off of the pairwise non-bonded interactions). However, the hard wall boundary conditions imposed here are expected to limit both lipid spreading and long-range membrane effects, such as induced curvature. Unfortunately, these two membrane properties are particularly difficult to model simultaneously with reasonable computational resources. To better model lipid spreading, periodic boundary conditions would be preferred. However, this would require significantly more particles in the corners of the simulation box that are not influential to the binding process. To better model long-range membrane effects, a bilayer patch several orders of magnitude larger is required, which would increase prohibitively the computational cost. In compromise of these computational limitations, a large bilayer disk with hard, cylindrical boundary was modeled.

The gel phase bilayer was created through the complete immobilization of the lipid tails of the equilibrated fluid phase bilayer, maintaining the same surface roughness, lipid density, and bilayer thickness in both bilayer phases. The gel vs. fluid bilayer differences in lipid density were not incorporated into this model so that the only difference between these simulated phases was the lipid tail mobility. These models best examine the effects of lipid tail mobility on the structure of bound nanoparticles.

The interactions and deformations of the dendrimer have been examined in terms of the enthalpic contributions to binding. These were calculated as averages over the

production simulation run of the CHARMM potential energy terms corresponding to the atomic bonds (distance, angles, and torsions), van der Waals, and electrostatic energies. The all-atom trajectory of thermal fluctuations around equilibrium was also analyzed in separate regions of the system to determine the potential energy stored in the various parts. The dendrimer self-energy and the dendrimer-lipid interaction energies were examined. This analysis did not incorporate the effects of entropy and thus is not a free energy calculation; it quantifies solely the enthalpic component (or more accurately for the canonical ensemble in which the simulations were run, the energy component).

4.3. RESULTS

G3 PAMAM dendrimers of varying termination were allowed to freely interact with DMPC bilayers of either fluid or gel phase. The resulting equilibrated, bound configuration was analyzed in terms of the atomistic morphology and the enthalpic contributions to binding. The dendrimers were roughly spherical both when far from the lipid bilayers and when bound to the gel phase lipid bilayer (Fig. 5.2). The gel phase lipid tails were restricted from moving and the gel phase bilayer retains its planar shape upon dendrimer binding. On the contrary, the fluid phase lipids tails were free to move and did so substantially upon dendrimer binding. The dendrimer flattened and elongated upon binding to the fluid phase lipids due to interactions of hydrophobic dendrimer components to the lipid tails (Figs. 2 and 3).

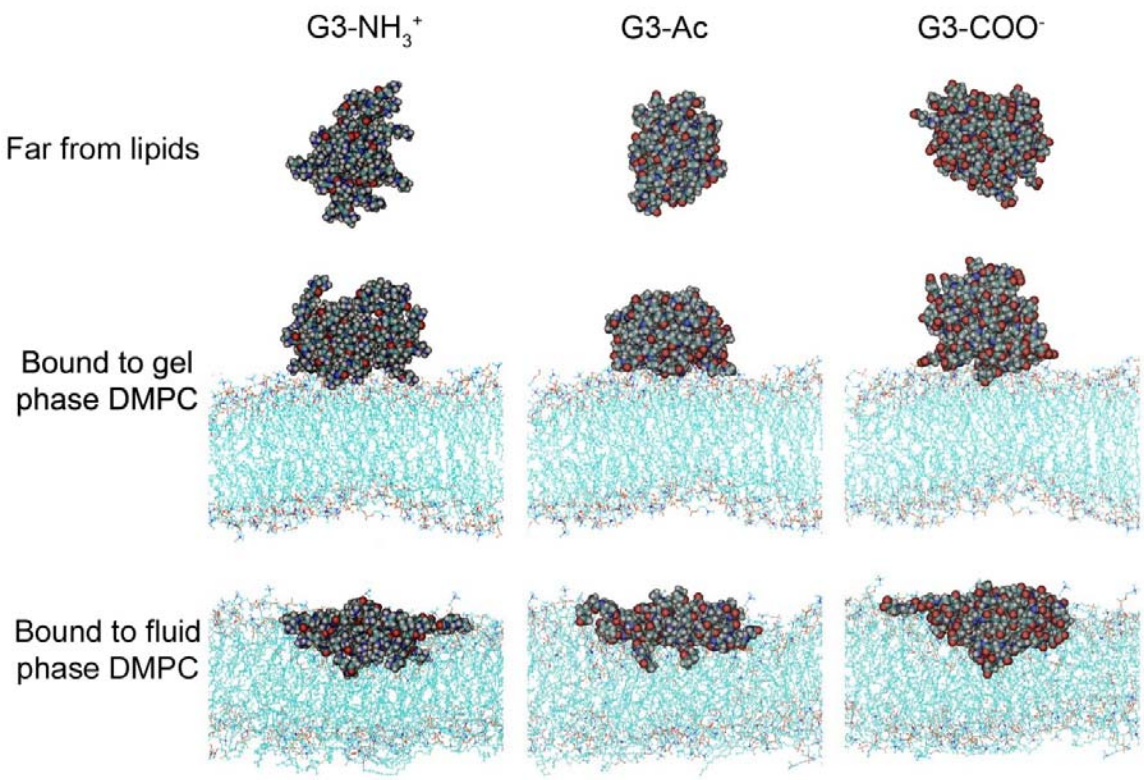

Figure 5.2. Representative images of the G3 dendrimer with varying terminations in equilibrated states: far from the lipids, bound to the gel phase DMPC bilayer, or bound to the fluid phase DMPC bilayer. These structures have been quantified in terms of dendrimer number and type of dendrimer-lipid contacts (Figs. 4 and 5), radius of gyration (Fig. 6A), asphericity (Fig. 6B), and self-energy (Fig. 7). Animations of the equilibrated dendrimers on the DMPC bilayers are found in the supplemental material.

The inner dendrimer components include hydrophobic and hydrophilic moieties. These moieties have been analyzed to determine their individual enthalpic contribution to binding. To facilitate the discussion of the dendrimer moieties, each has been given a unique name, as shown in Fig. 5.4. Similarly, each moiety within a termination has been named with the same convention utilized for the inner dendrimer components. The amides found throughout the dendrimer have been broken into carbonyl and secondary amine components for more detailed analysis than the traditional grouping as a single amide would permit.

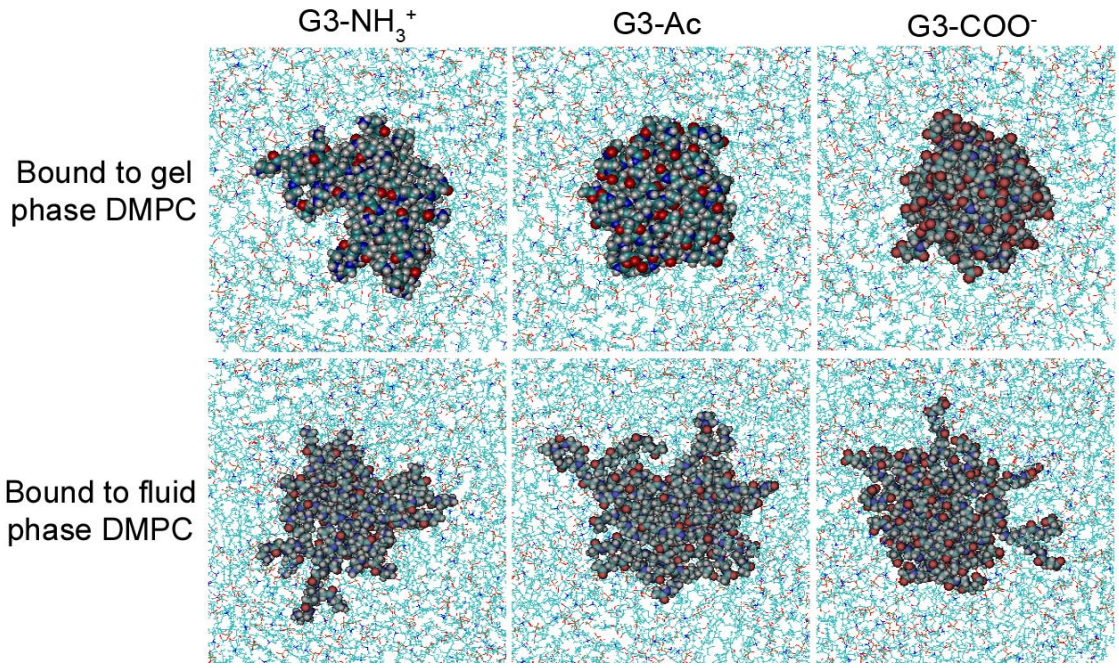

Figure 5.3. Top view of three different dendrimers on gel and fluid phase DMPC bilayers. The dendrimers increased both radius of gyration and asphericity as they bind to the fluid phase more so than upon binding to gel phase lipids, as represented here by the greater spreading of the dendrimers upon binding to fluid vs. gel phase. This increased interaction coincides with the availability of the hydrophobic lipid tails to interact with the hydrophobic dendrimer moieties.

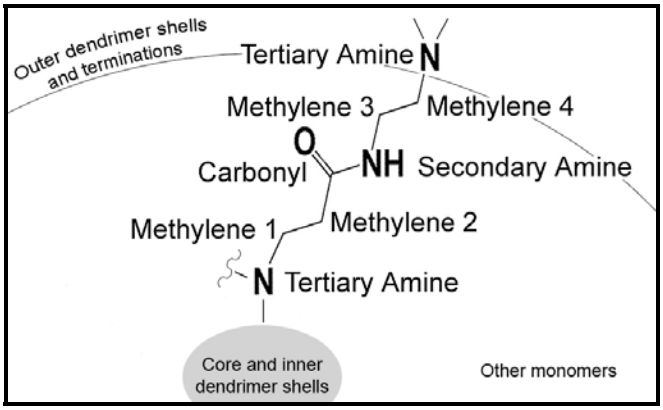

Figure 5.4. The internal structure of the G3 PAMAM dendrimers includes 60 of the repeating units shown here. Within each dendrimer, each methylene, secondary amine, and carbonyl is found 60 different times, while the tertiary amines occur only 30 different times per dendrimer. These internal dendrimer moieties are identical between all dendrimers. A similar naming convention has been implemented for the moieties within the dendrimer terminations.

The fluid phase bilayer formed a concave depression that accommodated a greater area for dendrimer-bilayer interaction. This dimple in the bilayer permitted more of the dendrimer to interact with the bilayer as well as more lipid molecules to interact with the dendrimer. This result is quantified by counting the number of dendrimer moieties within 3 Å of the lipids and the number of lipid molecules within 3 Å of the dendrimer (Fig. 5.5). In most situations, there were over twice as many interactions between dendrimer binding to fluid phase lipids than the gel phase lipids. The differences in deformability of the fluid vs. gel phase lipid bilayer resulted in a significantly different dendrimer binding morphology.

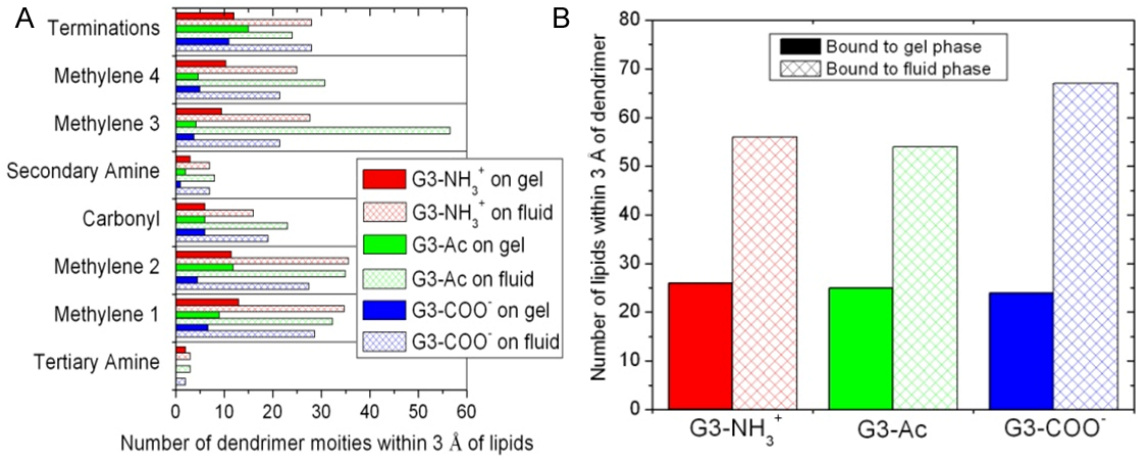

Figure 5.5. Number of dendrimer moieties within 3 Å of the lipid molecules and the number of lipid molecules within 3 Å of the dendrimer. The fluid phase bilayer permits a greater number of dendrimer-lipid interactions.

When either far from lipids or bound to gel phase lipids, the individual charged terminal groups of G3-NH_3^+ and G3-COO^- frequently extended away from the dendrimer core, whereas the G3-Ac maintained a highly compact structure. However, upon binding to fluid phase lipids, G3-Ac becomes most spread out as the hydrophobic dendrimer moieties reach to interact with the lipid tails. The morphological differences of G3-Ac with varied lipid environments are much greater than either G3-NH_3^+ or G3-COO^-.

Dendrimer morphology is quantified in terms of radius of gyration (R_G) and asphericity (A). The radius of gyration calculates the size of the dendrimer while incorporating density distributions,

$$R_G = \frac{1}{M}\sqrt{\sum_i m_i \left|\mathbf{x}_i - \mathbf{x}_0\right|^2}, \quad (1)$$

with the mass and location of the whole dendrimer (M, x_0) and each dendrimer atom (m_i, x_i).

The dendrimer radius of gyration is only slightly increased (< 2%) upon binding to the gel phase lipids, however upon binding to the fluid phase lipids, the radius of gyration increased between 10 to 40% (Fig. 5.6A). In comparing dendrimers with differing termination, G3-Ac was the smallest dendrimer in both the isolated and gel phase lipid environments, but obtained the largest radius of gyration on the fluid phase lipids. The trend is observed that, upon binding to fluid phase lipids, a dendrimer's radius of gyration increased more if it was hydrophobic and less if it was charged. G3-COO^- represented the middle ground in this regard between G3-Ac and G3-NH_3^+ due to the partially hydrophobic spacer present between the terminal secondary amine and the carboxylic acid.

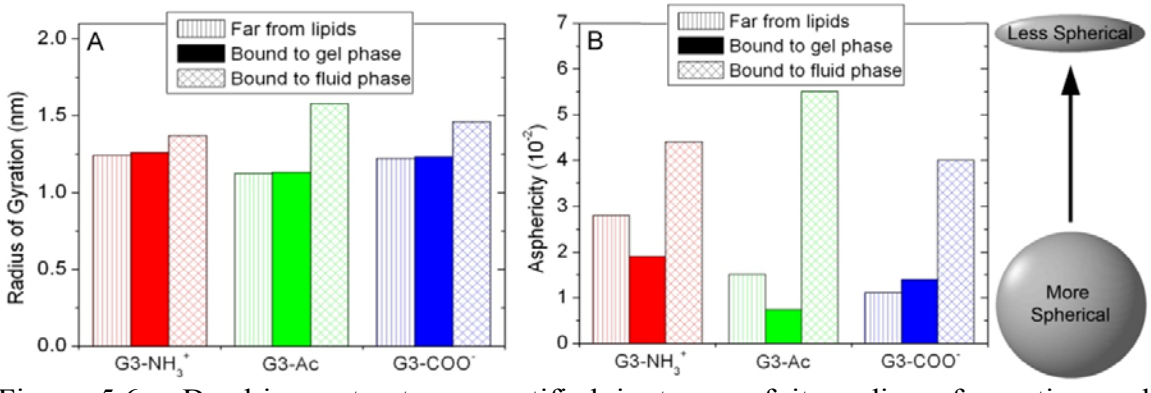

Figure 5.6. Dendrimer structure quantified in terms of its radius of gyration and asphericity, as defined in Eqs. (1) and (2). Upon binding to gel phase lipids, the

dendrimers neither increase their size nor flatten. However, upon binding to the fluid phase lipids, the dendrimers both increase in size and flatten considerably.

The morphological deviation of the dendrimer from that of a uniform density sphere was quantified by the dendrimer asphericity (A)[43],

$$A = 1 - 3\frac{\left\langle I_x I_y + + I_x I_z + I_y I_z \right\rangle}{\left\langle (I_x + I_y + I_z)^2 \right\rangle}, \quad (2)$$

where $I_{x,y,z}$ are the eigenvectors of the dendrimer's moment of inertia matrix. Upon binding to the gel phase bilayer, the asphericity of the amine and acetamide dendrimers decreased by 32 and 50%, respectively, while the carboxyl dendrimer increased by 23% (Fig 6B). Upon binding to fluid phase bilayers, the dendrimer asphericity increased by 50 to 360% as the dendrimer flatten and increase the number of lipid-dendrimer contacts. The changes in dendrimer shape and binding were analyzed in terms of the contributions to intra-dendrimer internal energy, i.e., the energy incorporated into the dendrimer which allowed for dendrimer deformation and enhanced binding. Quantification of this self-energy represents the extent to which the dendrimer deformed as a result of the dendrimer-lipid interaction (Fig. 5.7). Dendrimers increased their self-energy by 20 to 50% upon binding to the gel phase lipids and 60 to 440% upon binding to fluid phase lipids, with large variations depending on dendrimer termination.

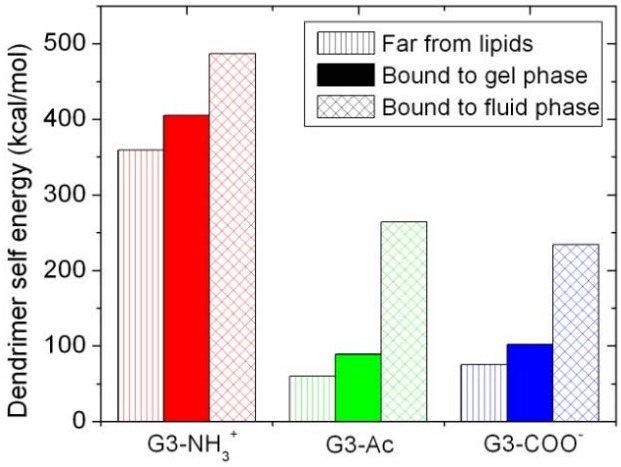

Figure 5.7. The dendrimer deformation quantified as the macromolecular self-energy. The self-energy of G3 PAMAM dendrimers is equal to the energy of the bonding, electrostatic, and van der Waals terms of the CHARMM force field between atoms in the dendrimer; this is a quantitative description of the dendrimer deformation upon binding. The dendrimers are in a higher energy, more deformed state when bound to the lipids, and more so for the fluid vs. gel phase lipids. G3-NH_3^+ begins in a more energetic state and deforms less to mediate binding as compared to G3-Ac or G3-COO^-.

The self-energy landscape of each system was approximately normally distributed in the equilibrium configuration. The differences between the means of each distribution are much greater than the standard error of the means for all data presented. The enthalpies of the lipid conformations are not presented since the differences between the mean enthalpy of various conformations was not significant due to the large number of lipid atoms not directly involved in the dendrimer binding and contributing to greater relative widths of the observed distributions.

Similarly, the strength of the dendrimer-membrane interaction was analyzed in terms of enthalpy. The binding of the dendrimer to the lipids is encouraged by an enthalpy release. This interaction enthalpy was calculated as the average, over the simulated trajectory, of the interaction energy between the whole dendrimer and the lipids as well as between different components of the dendrimer and the lipids (Fig. 5.8).

The restriction of the dendrimer to the bilayer plane has an entropic cost; however, binding may allow a greater number of conformations of lipid or dendrimer atoms. Therefore it is not clear whether or not binding was entropically favorable. Since these unbiased simulations demonstrated favorable binding between the dendrimer and the lipids, the binding process is favorable by free energy, and the magnitude of this free energy (calculated using a rigorous umbrella sampling formalism) is the subject of a companion article also in this journal.[17]

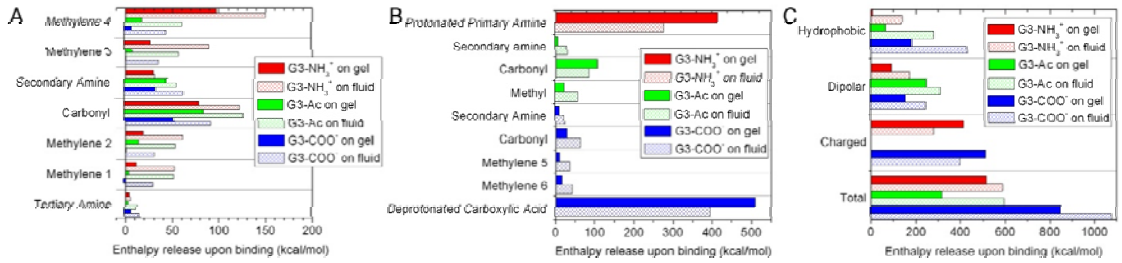

Figure 5.8. Enthalpy release from the interaction of the dendrimer with the lipids is shown for various parts of the dendrimer. For the inner dendrimer moieties shown in Fig. 4, the enthalpies of interaction for each moiety type are shown in (a). For each moiety found within the dendrimer terminations, as shown in Fig. 1, the enthalpies of interaction are shown in (b). The results of (a) and (b) are combined into (c) as the dendrimer moieties are categorized as hydrophobic, dipolar, or charged. The charged moieties bound more weakly to the fluid vs. gel phase lipids where the hydrophobic moieties bind over twice as strongly. The majority of the fluid vs. gel phase lipid binding differences is mediated by the hydrophobic dendrimer components.

The enthalpy of interaction was calculated for all six dendrimer-lipid configurations and for many dendrimer moieties within both the inner dendrimer shells (Fig. 5.8A) and the terminations (Fig. 5.8B). Fig. 5.8C combines all the dendrimer moieties into the categories hydrophobic, dipolar, or charged where the enthalpic contribution is shown for each type of moiety.

Within this sizeable data set, there are multiple interesting observations:

- The inner dendrimer shells did not interact strongly with the gel phase lipids. There were stronger interactions between the inner dendrimer and the fluid phase lipids where the dendrimer and lipids deform to mediate binding.
- The hydrophobic moieties displayed increased binding enthalpy on fluid vs. gel phase lipids as they favorably interact with the hydrophobic lipid tails in fluid phase lipids.
- The charged moieties decreased in their net enthalpic interaction on fluid vs. gel phase lipids even though over twice as many were within 3 Å of the lipids.
- G3-NH_3^+ showed the least increase in total interaction energy on fluid vs. gel phase lipids and G3-NH_3^+ contains the fewest hydrophobic moieties.

5.4. DISCUSSION

The most energetically influential moieties in binding were the charged moieties; however, their interactions were remarkably similar to the sum of the hydrophobic moieties on the fluid lipids. These results highlight the importance of internal dendrimer structure and hydrophobic/hydrophilic composition to biological activity.

The results reported in the present work provide specific energetic underpinnings for improving dendrimer design for enhanced targeting of particular membrane components. Initial binding is enhanced greatly by the addition of charged moieties to the dendrimer by strong dendrimer-lipid head group interactions. However, the dendrimers are more likely to penetrate into the lipid tails, deform, and prefer fluid phase bilayer if the dendrimer contains hydrophobic regions accessible to the lipid tails without diminishing the hydrophilic interactions.

These simulations provide further evidence regarding the location of dendrimers bound to lipids. In all systems, the dendrimers bound to the lipids. On gel phase lipids, the dendrimers remained atop of the bilayer and did not significantly deform to accommodate binding. On fluid phase lipids, however, the dendrimers did not remain atop the bilayer. The observed intercalation of the dendrimer into the hydrophobic bilayer regions is consistent with continuum models[44] and partially consistent with coarse grained models.[22] Coarse grained models suggest that only the charged dendrimers become secluded in the bilayer, whereas both the continuum models and atomistic models presented here suggest all dendrimers intercalate into the bilayer.

As the dendrimers bound to the fluid phase lipids and the lipids formed a divot to accommodate binding, the lipid head groups partially lined the divot. The lipids were arranged such that the hydrophobic dendrimer moieties were accessible to the hydrophobic lipid tails and the polar dendrimer moieties had some polar lipid head groups nearby also.

This paper addresses two central questions: 1) What are the atomistic causes and effects of dendrimers binding to gel vs. fluid bilayers? 2) How does the variation in dendrimer termination and lipid phase affect binding? The numerical results presented answer both questions via atomistic molecular dynamics simulations. Three hypotheses have been developed and tested while providing insight into the importance of dendrimer structure and lipid phase in biological functionality.

Hypothesis 1: The fluid phase lipid bilayer deforms to accommodate dendrimer-lipid interactions with more of the dendrimer and lipids in contact than the gel phase lipids.

These simulations are consistent with this hypothesis. The images for the simulations (Figs. 2 and 3), show the dendrimers penetrated into the fluid phase lipids and the lipid head groups have formed a depression accepting the dendrimer. Many of the dendrimer moieties were in close contact with the fluid phase lipid tails, which did not occur with gel phase lipids. As shown in Fig. 5.5, approximately three times as many dendrimer moieties are within 3 Å of the lipids and approximately twice as many lipid molecules are within 3 Å of the dendrimer for fluid vs. gel lipids.

Hypothesis 2: The dendrimers achieve stronger interaction energy with fluid phase lipids than gel phase lipids due to the mobility of the fluid phase lipids allowing the dendrimers' terminal groups to obtain more favorable interactions.

Although the dendrimers as a whole obtain a stronger interaction with fluid vs. gel phase lipids, it is not mediated by the terminal groups. Rather, the difference in binding is driven primarily by the inner dendrimer moieties, especially the hydrophobic parts. The net enthalpy of binding is 14% stronger for G3-NH_3^+, 27% stronger for G3-COO^-, and 87% stronger for G3-Ac for the fluid vs. gel phase lipids. However, the enthalpy of binding for terminal groups of G3-NH_3^+ and G3-COO^- are weaker on fluid vs. gel phase lipids, by 48 and 2%, respectively. The uncharged terminal groups on G3-Ac bind more strongly to fluid vs. gel phase lipids, but much less so than the entire dendrimer. This result contradicts previously held perceptions that the dendrimer binding is dominated by the dendrimer terminal groups and emphasizes the importance of the inner dendrimer structure on the fluid vs. gel phase interactions.

Hypothesis 3: The charged dendrimers (G3-NH_3^+ and G3-COO^-) bind enthalpically stronger than the uncharged dendrimer (G3-Ac) and, as such, the charged dendrimers become more morphologically changed upon binding.

The charged dendrimers bind more strongly than the uncharged dendrimer. However, contrary to this hypothesis, G3-Ac becomes significantly more deformed upon binding to the lipids than does either of the charged dendrimers. The morphological changes of binding for all three dendrimers are similar upon the gel phase lipids. Yet on the fluid phase lipids, greater deformation occurs for dendrimers that are more hydrophobic, regardless of dendrimer charge.

5.5. CONCLUSIONS

This manuscript addressed the mechanisms of dendrimer binding to lipid bilayers, specifically the role of the terminations of G3 PAMAM dendrimers and the phase of DMPC lipid bilayers. The variations in dendrimer termination demonstrate the strong effect of charged terminal groups on binding and overall dendrimer morphology. The charged terminal groups in particular release 28% less enthalpy upon interacting with fluid vs. gel phase lipids, even though over twice as many were within 3 Å of the lipids on fluid vs. gel lipids.

The inner-dendrimer hydrophobic components are most influential for enhancing binding to fluid vs. gel phase lipids. Similar to the charged terminals, over twice as many of the hydrophobic moieties were within 3 Å of the fluid vs. gel phase lipids. Contrary to the charged terminals, the hydrophobic moieties released twice as much enthalpy upon binding to fluid vs. gel lipids. All dendrimers bind more strongly to the fluid vs. gel phase

lipids, but this is most pronounced for the uncharged dendrimer (G3-Ac), with net 88% greater enthalpy release on fluid vs. gel phase lipids. It is concluded that the hydrophobic dendrimer moieties are the key to enhanced binding to fluid vs. gel phase lipids.

5.6. ACKNOWLEDGMENTS

Pascale R. Leroueil, Bradford G. Orr, Mark M. Banaszak Holl, and Ioan Andricioaei made essential contributions to this research. Fellowship support was received from the NIH Michigan Molecular Biophysics Training Program (T32 GM008270-20), the Applied Physics program, and the Graham Environmental Sustainability Institute. Computational time was provided by the Center for Advanced Computing at the University of Michigan and Lawrence Livermore National Laboratory. The authors thank Christine Orme, Timothy Sullivan, James R. Baker, Jr., Elizabeth Nett, and Jeffery Wereszczynski. This research was supported by a grant from the National Institute of Biomedical Imaging and BioEngineering (R01-EB005028) and the NSF CAREER award program (CHE-0548047).

5.7. REFERENCES

1. Sahoo, S. K.; Labhasetwar, V., Nanotech approaches to delivery and imaging drug. *Drug Discovery Today* **2003,** 8, (24), 1112-1120.
2. Yang, H.; Kao, W. Y. J., Dendrimers for pharmaceutical and biomedical applications. *Journal of Biomaterials Science-Polymer Edition* **2006,** 17, (1-2), 3-19.
3. Bosman, A. W.; Janssen, H. M.; Meijer, E. W., About dendrimers: Structure, physical properties, and applications. *Chemical Reviews* **1999,** 99, (7), 1665-1688.
4. Tang, M. X.; Redemann, C. T.; Szoka, F. C., In vitro gene delivery by degraded polyamidoamine dendrimers. *Bioconjugate Chemistry* **1996,** 7, (6), 703-714.
5. Stiriba, S. E.; Frey, H.; Haag, R., Dendritic polymers in biomedical applications: From potential to clinical use in diagnostics and therapy. *Angewandte Chemie-International Edition* **2002,** 41, (8), 1329-1334.
6. Tomalia, D. A.; Baker, H.; Dewald, J.; Hall, M.; Kallos, G.; Martin, S.; Roeck, J.; Ryder, J.; Smith, P., A New Class of Polymers - Starburst-Dendritic Macromolecules. *Polymer Journal* **1985,** 17, (1), 117-132.
7. Quintana, A.; Raczka, E.; Piehler, L.; Lee, I.; Myc, A.; Majoros, I.; Patri, A. K.; Thomas, T.; Mule, J.; Baker, J. R., Design and function of a dendrimer-based therapeutic nanodevice targeted to tumor cells through the folate receptor. *Pharmaceutical research* **2002,** 19, (9), 1310-1316.
8. Majoros, I. J.; Thomas, T. P.; Mehta, C. B.; Baker, J. R., Poly(amidoamine) dendrimer-based multifunctional engineered nanodevice for cancer therapy. *Journal of medicinal chemistry* **2005,** 48, (19), 5892-5899.
9. Patri, A. K.; Majoros, I. J.; Baker, J. R., Dendritic polymer macromolecular carriers for drug delivery. *Curr. Opin. Chem. Biol.* **2002,** 6, (4), 46-471
10. Landmark, K. J.; DiMaggio, S.; Ward, J.; Vogt, S.; Hong, S.; Kotlyar, A.; Penner-Hahn, J. E.; James R. Baker, J.; Holl, M. M. B.; Orr, B. G., Synthesis, Characterization, and In Vitro Testing of Superparamagnetic Iron Oxide Nanoparticles Targeted Using Folic Acid-Conjugated Dendrimers. *Submitted* **2007**.
11. Hubbell, J. A., Multifunctional polyplexes as locally triggerable nonviral vectors. *Gene Therapy* **2006,** 13, 1371-1372.
12. Hong, S. P.; Leroueil, P. R.; Janus, E. K.; Peters, J. L.; Kober, M. M.; Islam, M. T.; Orr, B. G.; Baker, J. R.; Holl, M. M. B., Interaction of polycationic polymers with supported lipid bilayers and cells: Nanoscale hole formation and enhanced membrane permeability. *Bioconjugate Chemistry* **2006,** 17, (3), 728-734.
13. Lai, J. C.; Yuan, C. L.; Thomas, J. L., Single-cell measurements of polyamidoamine dendrimer binding. *Annals of Biomedical Engineering* **2002,** 30, (3), 409-416.
14. Fischer, D.; Li, Y. X.; Ahlemeyer, B.; Krieglstein, J.; Kissel, T., In vitro cytotoxicity testing of polycations: influence of polymer structure on cell viability and hemolysis. *Biomaterials* **2003,** 24, (7), 1121-1131.
15. Manunta, M.; Nichols, B. J.; Tan, P. H.; Sagoo, P.; Harper, J.; George, A. J. T., Gene delivery by dendrimers operates via different pathways in different cells, but is

enhanced by the presence of caveolin. *Journal of Immunological Methods* **2006,** 314, (1-2), 134-146.
16. Manunta, M.; Tan, P. H.; Sagoo, P.; Kashefi, K.; George, A. J. T., Gene delivery by dendrimers operates via a cholesterol dependent pathway. *Nucleic Acids Research* **2004,** 32, (9), 2730-2739.
17. Kelly, C. V.; Leroueil, P. R.; Janus, E. K.; Wereszczynski , J. M.; Baker, J. R.; Orr, B. G.; Holl, M. M. B.; Andricioaei, I., Poly(amidoamine) dendrimers on lipid bilayers I: free energy and conformation of binding. *Submitted* **2008**.
18. Leroueil, P. R.; Hong, S. Y.; Mecke, A.; Baker, J. R.; Orr, B. G.; Holl, M. M. B., Nanoparticle interaction with biological membranes: Does nanotechnology present a janus face? *Accounts of Chemical Research* **2007,** 40, (5), 335-342.
19. Mecke, A.; Uppuluri, S.; Sassanella, T. M.; Lee, D. K.; Ramamoorthy, A.; Baker, J. R.; Orr, B. G.; Holl, M. M. B., Direct observation of lipid bilayer disruption by poly(amidoamine) dendrimers. *Chemistry and physics of lipids* **2004,** 132, (1), 3-14.
20. Mecke, A.; Lee, D. K.; Ramamoorthy, A.; Orr, B. G.; Holl, M. M. B., Synthetic and Natural Polycationic Polymer Nanoparticles Interact Selectively with Fluid-Phase Domains of DMPC Lipid Bilayers. *Langmuir* **2005,** 21, 8588-8590}.
21. Mecke, A.; Lee, I.; Baker, J. R.; Holl, M. M. B.; Orr, B. G., Deformability of poly(amidoamine) dendrimers. *European Physical Journal E* **2004,** 14, (1), 7-16.
22. Lee, H.; Larson, R. G., Molecular Dynamics Simulations of PAMAM Dendrimer-Induced Pore Formation in DPPC Bilayers with a Coarse-Grained Model. *J.Phys.Chem.B 2006, 110, 18204-18211* **2006,** 110, 18204-18211.
23. Mecke, A.; Majoros, I. J.; Patri, A. K.; Baker, J. R.; Holl, M. M. B.; Orr, B. G., Lipid bilayer disruption by polycationic polymers: The roles of size and chemical functional group. *Langmuir* **2005,** 21, (23), 10348-10354.
24. Hong, S. P.; Bielinska, A. U.; Mecke, A.; Keszler, B.; Beals, J. L.; Shi, X. Y.; Balogh, L.; Orr, B. G.; Baker, J. R.; Holl, M. M. B., Interaction of poly(amidoamine) dendrimers with supported lipid bilayers and cells: Hole formation and the relation to transport. *Bioconjugate chemistry* **2004,** 15, (4), 774-782.
25. Hong, S.; Leroueil, P. R.; Majoros, I. J.; Orr, B. G.; Baker, J. R.; Holl, M. M. B., The binding avidity of a nanoparticle-based multivalent targeted drug delivery platform. *Chemistry & Biology* **2007,** 14, (1), 105-113.
26. Brown, D. A.; London, E., Functions of lipid rafts in biological membranes. *Annu. Rev. Cell. Dev. Biol.* **1998,** 14, 111-136.
27. Simons, K.; Ikonen, E., Functional rafts in cell membranes *Nature* **1997,** 387, (6633), 569-572.
28. Holl, M. M. B., Cell Plasma Membranes and Phase Transitions. *In Press*.
29. Leroueil, P. R.; Berry, S. A.; Duthie, K.; Han, G.; Rotello, V. M.; McNerny, D. Q.; Baker, J. R.; Orr, B. G.; Holl, M. M. B., Wide Varieties of Cationic Nanoparticles Induce Defects in Supported Lipid Bilayers. *Nano Letters* **2008**, (ASAP).
30. Marrink, S. J.; de Vries, A. H.; Mark, A. E., Coarse grained model for semiquantitative lipid simulations. *Journal of Physical Chemistry B* **2004,** 108, (2), 750-760.
31. Brooks, B. R.; Bruccoleri, R. E.; Olafson, B. D.; States, D. J.; Swaminathan, S.; Karplus, M., Charmm - a Program for Macromolecular Energy, Minimization, and Dynamics Calculations. *Journal of Computational Chemistry* **1983,** 4, (2), 187-217.

32. MacKerell, A. D.; Bashford, D.; Bellott, M.; Dunbrack, R. L.; Evanseck, J. D.; Field, M. J.; Fischer, S.; Gao, J.; Guo, H.; Ha, S.; Joseph-McCarthy, D.; Kuchnir, L.; Kuczera, K.; Lau, F. T. K.; Mattos, C.; Michnick, S.; Ngo, T.; Nguyen, D. T.; Prodhom, B.; Reiher, W. E.; Roux, B.; Schlenkrich, M.; Smith, J. C.; Stote, R.; Straub, J.; Watanabe, M.; Wiorkiewicz-Kuczera, J.; Yin, D.; Karplus, M., All-atom empirical potential for molecular modeling and dynamics studies of proteins. *Journal of Physical Chemistry B* **1998,** 102, (18), 3586-3616.
33. Mercier, G. A., Dendrimer Builder. *http://server.ccl.net/chemistry/resources/messages/1996/05/20.009-dir/index.html* **1996**.
34. Humphrey, W.; Dalke, A.; Schulten, K., VMD: Visual molecular dynamics. *Journal of Molecular Graphics* **1996,** 14, (1), 33.
35. Lee, I.; Athey, B. D.; Wetzel, A. W.; Meixner, W.; Baker, J. R., Structural molecular dynamics studies on polyamidoamine dendrimers for a therapeutic application: Effects of pH and generation. *Macromolecules* **2002,** 35, (11), 4510-4520.
36. Paulo, P. M. R.; Lopes, J. N. C.; Costa, S. M. B., Molecular Dynamics Simulations of Charged Dendrimers: Low-to-Intermediate Half-Generation PAMAMs. *J. Phys. Chem. B* **2007,** 111, (36), 10651-10664.
37. Feig, M.; Brooks, C. L., Recent advances in the development and application of implicit solvent models in biomolecule simulations. *Current Opinion in Structural Biology* **2004,** 14, (2), 217-224.
38. Bashford, D.; Case, D. A., Generalized born models of macromolecular solvation effects. *Annual Review of Physical Chemistry* **2000,** 51, 129-152.
39. Johnson, S. J.; Bayerl, T. M.; McDermott, D. C.; Adam, G. W.; Rennie, A. R.; Thomas, R. K.; Sackmann, E., Structure of an Adsorbed Dimyristoylphosphatidylcholine Bilayer Measured with Specular Reflection of Neutrons. *Biophysical journal* **1991,** 59, (2), 289-294.
40. Kucerka, N.; Liu, Y. F.; Chu, N. J.; Petrache, H. I.; Tristram-Nagle, S. T.; Nagle, J. F., Structure of fully hydrated fluid phase DMPC and DLPC lipid bilayers using X-ray scattering from oriented multilamellar arrays and from unilamellar vesicles. *Biophysical journal* **2005,** 88, (4), 2626-2637.
41. Hunenberger, P. H.; McCammon, J. A., Effect of artificial periodicity in simulations of biomolecules under Ewald boundary conditions: a continuum electrostatics study. *Biophysical Chemistry* **1999,** 78, (1-2), 69-88.
42. Castro-Roman, F.; Benz, R. W.; White, S. H.; Tobias, D. J., Investigation of finite system size effects in molecular dynamics simulations of lipid bilayers. *Journal of Physical Chemistry B* **2006,** 110, (47), 24157-24164.
43. Rudnick, J.; Gaspari, G., The asphericity of random walks. *Journal of Physics A: Math. Gen.* **1986,** 19, L191-L193.
44. Ginzburg, V. V.; Balijepalli, S., Modeling the Thermodynamics of the Interaction of Nanoparticles with Cell Membranes. *Nano Lett.* **2007**.

CHAPTER 6

CONCLUSIONS AND OUTLOOK

This dissertation analyzed the effects of two types of nanoscale perturbations on the plasma membrane. One of the primary functions of the plasma membrane is to protect the cell from damage upon exposure to a variety of stressors, such as exposure to synthetic nanoparticles or fluctuations in temperature and pressure. The membrane response to intense pressure and temperature fluctuations is the subject of Chapter 2. The membrane response to exposure of nanoparticles is the subject of Chapters 3, 4 and 5. While this research contributes significant new understandings to the field, it has also proposed further questions concerning the functioning of the plasma membrane.

The interaction of pulsed lasers and living cells is of significant interest in both basic science and medical application. Via multiphoton processes, light was absorbed within nanoscale volumes and induced local evaporation of the cytosol. We have examined the micron-scale membrane response of the cell to severe irradiation through fluorescent microscopy. The blebbing process is a fascinating balance of osmotic forces, biochemical processes, and surface tension.

Further research in this field will explain nanoscale biological response to irradiation. To examine small length scales of biological response, another method of examining the cell is necessary. For example, ultra-high resolution microscopy has the

potential to examine nanoscale fluorochrome distributions in biological systems. Microscopy systems such as photo-activated localization microscopy (PALM) and stochastic optical reconstruction microscopy (STORM) have been used to localize molecules to 20 nm resolution and provide structural descriptions of biological systems well beyond that previously done optically. Utilization of these techniques to examining the cellular response to irradiation could answer: Is it possible to create a single nanoscale plasma membrane defect by irradiation? If so, does the cell repair the hole? How quickly and with what biochemical processes?

The interaction of synthetic polymers and the plasma membrane is important for both the development of medical nanodevices as well as avoiding environmental side effects from commercial applications. Chapter 3 experimentally examines the stoichiometry of interaction, as observable with the enthalpy change upon mixing dendrimers and phospholipids, and theoretically examines the atomistic details of interaction. Experimentally, it has been shown that nanoparticles of sufficient size and electrostatic charge are wrapped by a phospholipid bilayer, likely leading to membrane disruption and pore formation. In Chapters 4 and 5, the energetics of dendrimer-lipid interaction, in terms of the total free energy as well as the enthalpic components from particular atomic moieties, were calculated through molecular dynamics simulations. It was identified that although the electrostatic interaction between the charged terminal groups of the dendrimers and charged moieties of the zwitterionic phospholipids were identified as highly influential, the majority of the difference between dendrimers of varying termini and lipids of varying phase was the interaction between hydrophobic dendrimer moieties and hydrophobic lipid moieties.

These hydrophobic interactions are one of the key components of the system that should be explored in future studies. In fact, simulations are currently being performed to explore the effects of increasing amounts of hydrophobic moieties on the surface of PAMAM dendrimers. These simulations examine the key features identified in Chapters 4 and 5 as influential components to the interaction. These simulations incorporate third-generation PAMAM dendrimers with combinations of terminal groups composed of primary amines, methyl groups, ethyl groups, butyl groups, and carboxyl groups.

Further, these newest simulations improve upon the solvent model by explicitly including the water molecules, rather than with an implicit model as used in Chapters 4 and 5. The work to date utilizes a 4r dielectric function to account for the solvent screening between electrostatically charged atoms within the simulation. Although this model has been shown to work well in select circumstances, the fact that entropic contributions from the solvent are not incorporated into the observed free energy changes is the greatest approximation in these previous results. The current simulations incorporate explicit solvent, are a large improvement to the accuracy of the model, and should be very useful in determining the robustness of the previous conclusions.

Greater understandings of the dendrimer-membrane interactions could come from greater computational abilities or novel experimental approaches. Experimental techniques such as NMR and fluorescence resonance energy transfer could determine which atomic moieties were in close proximity between the dendrimer and the phospholipids.

In conclusion, this dissertation includes a variety of experimental and theoretical techniques to understand the plasma membrane upon nanoscale perturbations. Continued

examination of the biological response to pulsed laser light and synthetic polymers holds great promise for the development of novel technologies, medical treatments, and reduced side effects of commercial nanoparticles.

APPENDIX

This appendix includes a representative scripts used for the all-atom molecular dynamics simulations, as described in Chapters 4 and 5. The creation of the potential of mean force within Chapter 4 included running simulations of each dendrimer type at various windows along the interaction coordinate. Following is the script used to perform the simulation of G3-NH_3^+ above a DMPC bilayer with the umbrella sampling offset at 35 Å.

```
* Simulation of amine above DMPC, rc = 35Å
*

set zcur 35                 ! This should never have a ".0"
set term ami                ! ace, ami, or car
set numsteps 250000         ! one step equals 2 fs with shake
set iternum 0               ! if check load cor file and load res file with change in iternum
set esu sim

faster on

set sfiles /g/g15/kelly54/support_files

calc zprev = @zcur + 0.5
calc zprevten = @zprev * 10
calc zcurten = @zcur * 10

calc iterprev =  @iternum - 1
set loadcorfile @term_tdmpc_sim_@zprevten_0.cor
set loadresfile @term_tdmpc_sim_@zprevten_0.res

! --- topology and parameter files ---
open unit 1 card read name @sfiles/top_all27_lipid_@term.rtf
read RTF card unit 1
open unit 1 card read name @sfiles/pamam_@term.rtf
read RTF card unit 1 append
open unit 1 card read name @sfiles/lipid_dendrimer_@term.prm
read PARA card unit 1
close unit 1
```

```
bomb -1
!read psf and coordinates
open unit 20 card read name @sfiles/@term_tdmpc.psf
read psf card unit 20

open unit 20 read form name @loadcorfile
read coor card unit 20
close unit 20
bomb 0

define dendrimer sele resname AMT .or. resname CORE end
define lipids sele resname DMPC end
define pretails sele type -
  C2*  .or. type C3*  .or. type H*T  .or. type H*S  .or. type -
  H*R  .or. type H*X  .or. type H*Y  .or. type H*Z  .or. type -
  O3*  .or. type O2*  end
define tails sele pretails .and. lipids end
define heads sele lipids .and. .not. tails end

! --- Put a potential barrier around the system to keep the
!dendrimer centered over the lipid disk
MMFP
GEO cylinder sawood P1 0.05 P2 3.0 -
   xref 0.0 yref 0.0 zref 0.0 xdir 0.0 ydir 0.0 -
   zdir 1.0 force 200.0 droff 2 select RCM dendrimer end
END

! --- Assorted variables to set reaction coordinate
set ld 38
set hd 62
set deld 0.5
set k 5
set rcorval 60
let rcorval = 1 * @zcur
rxncor: define e3 point mass sele dendrimer end
rxncor: define p1 point sele bynum 2381 end
rxncor: define p2 point sele bynum 14376 end
rxncor: define p3 point sele bynum 11186 end
rxncor: define xyplane plane thro p1 thro p2 thro p3
rxncor: define rcor distance xyplane e3
rxncor: set rcor
rxncor: trace rcor unit 21
open unit 21 write form name  @term_tdmpc_@esu_@zcurten_@iternum.tr
rxncor: umbrella form 1 kumb @k del0 @rcorval
rxncor: stat lowdelta @ld hidelta @hd deldel @deld start 0

! --- confirm locations
coor stat sele dendrimer end
coor stat sele lipids end
coor stat sele bynum 2381 end
coor stat sele bynum 14376 end
coor stat sele bynum 11186 end


! --- Specifications for NONBond interactions
```

```
NBONDS CUTNb 13.0 CTONnb 8.0 CTOFnb 12.0 -
   SWITCH VSWItch RDIElectric EPSilon 4.0

! --- Load restart file
open unit 11 read form name @loadresfile

! --- open restart and dcd files
OPEN UNIT 12 WRITe FORMatted –
                  NAME @term_tdmpc_@esu_@zcurten_@iternum.res
OPEN UNIT 14 WRITe UNFORMatted –
                  NAME @term_tdmpc_@esu_@zcurten_@iternum.dcd

SCALAR FBETA SET 50 sele all end

! --- Fix lipid tails for gel phase simulations
shake bonh
cons fix sele tails .or. prop z .lt. 0 .or. segid L188 end

DYNA LEAP LANGEVIN reSTRT NSTEP @numsteps TIMESTEP 0.002 -
   IPRFRQ 1000 IHTFRQ 0 IEQFRQ 0 NTRFRQ 0 -
   IUNREA 11 IUNWRI 12 IUNCRD 14 IUNVEL -1 KUNIT 70 -
   NPRINT 1000 NSAVC 1000 NSAVV 0 IHBFRQ 0 INBFRQ 10 -
   ILBFRQ 1000 RBUFFER 0.0 TBATH 300.0 -
   FIRSTT 300.0 FINALT 300.0  -
   IASORS 0 IASVEL 1 ISCVEL 0 ICHECW 0 TWINDH 0.0 TWINDL 0.0 -
   ISEED 413851


! --- Unfix lipid for saving
cons fix sele none end

open write unit 1 card name @term_tdmpc_@esu_@zcurten_@iternum.cor
write coor card unit 1
* Simulation Result
*

STOP
```